Thesis Report

Design of A Thermal Protection System for a Mars Entry Vehicle with Ceramic Matrix Composites

Danny Tjokrosetio

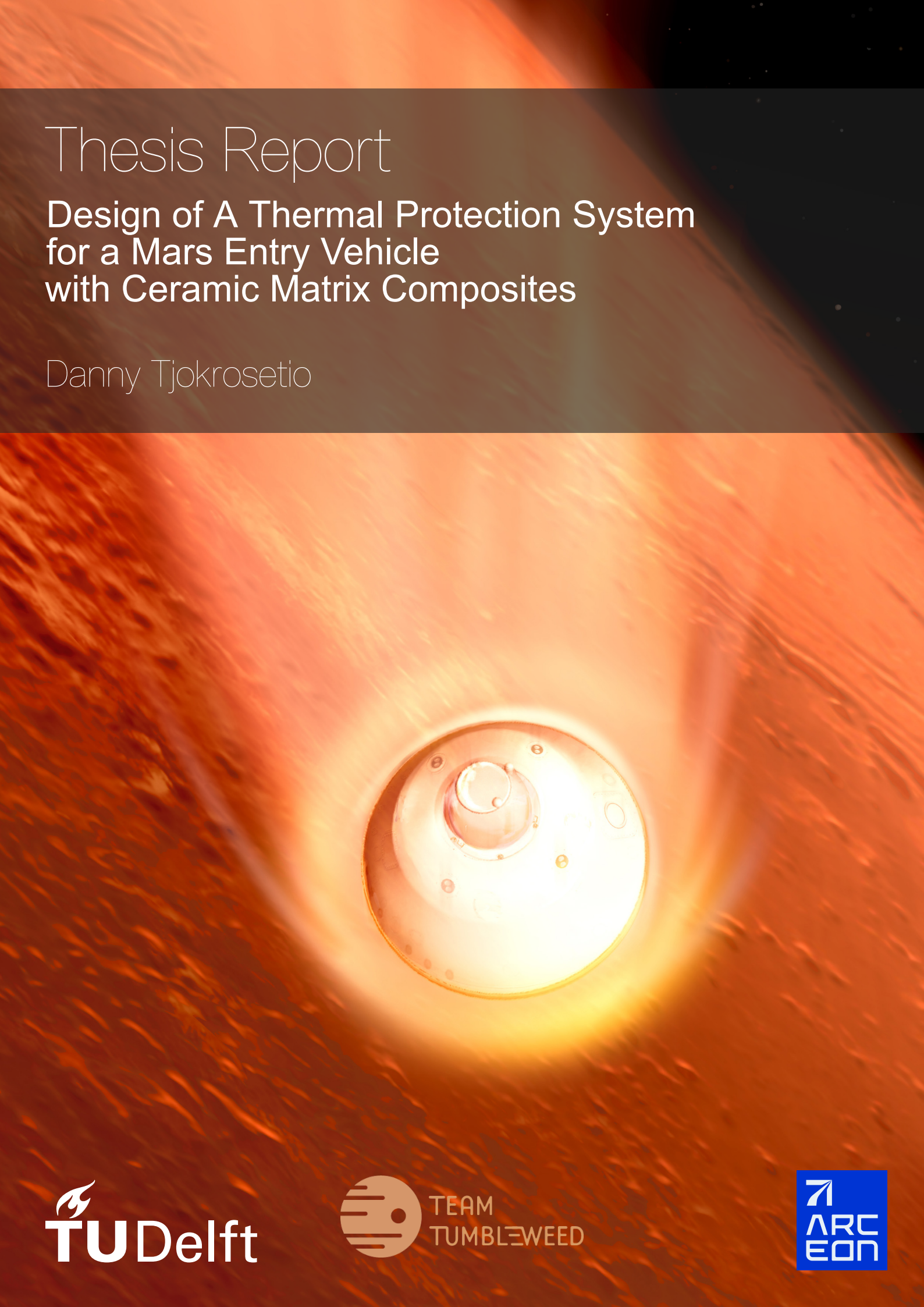

TU Delft

TEAM TUMBLEWEED

ARC EON

Thesis Report

Design of A Thermal Protection System for a Mars Entry Vehicle with Ceramic Matrix Composites

by

Danny Tjokrosetio

A thesis submitted to obtain the degree of
Master of Science in Aerospace Engineering
at the Delft University of Technology

Student number:	4832310	
Supervisors:	I. U. Balbin,	Aerospace Structures & Materials
	Y. J. van Haaren,	External, Arceon B.V.
Graduation committee:	Dr. S. J. Garcia,	Novel Aerospace Materials
	Dr. ir. E. Mooij,	Astrodynamics & Space Missions

Cover: Artist's rendering of the Mars 2020 aeroshell entering the Martian atmosphere. Courtesy of NASA.

TU Delft

TEAM TUMBLEWEED

ARC EON

Preface

"There is no greater flex than seeing your name dropped in a Master's thesis preface."

- G.G.

The completion of this thesis marks a turning point in my life. A turning point, mathematically speaking, can mean either a local maximum or minimum. While writing this thesis may not be my highest point at this phase of the continuous function we call life, the years on which I have worked on it have led to it and were nothing but transformative. While I have decided to take on multiple (life-changing) tangents that have delayed the completion of this project, I met a number of people who became pivotal to my story arc. I would like to take this page and the next to thank those I consider highly influential, and the real homies who have stuck with me, over the past 6 years; thank you for showing up to the function.

First of all, my deepest gratitude goes to my academic supervisor Ines Uriol Balbin. You truly watched me grow from a confused post-Bachelor's student to a still-confused Delft graduate and emerging space leader. I could not ask for a more supportive supervisor through your encouragement in my highs and lows, never-ending facepalms, mastery of impossible deadlines, and ability to work through my whirlwinds of chaos. I would also like to thank the team at Arceon. As this thesis is vastly different from my original assignment and saw further topical iterations, Rahul Shirke and Rahul Sharma have been incredibly patient and accommodating in the process to identify and incorporate my technical passions. Yestin, we started out as equals and shared the same desk in 2022 - you leveled up and stepped in as my company supervisor; I am grateful for your constant eagerness to answer my questions on the materials side even at the dead of night and your bouts of motivation to help me power through.

Team Tumbleweed was not only a side quest that turned into a main quest through their incorporation into this thesis, but is also a family to me. They go beyond pushing the boundaries of Mars exploration; I cherish the little things like pulling long hours with Austin, Misha, Julian, and Lucas at the office while impulsively verbalizing meme references, running James over with a remote-controlled Mars rover, dogsitting with One, and being the head chef during ramen night at the Tumbleweed household.

My life at Delft has never been boring thanks to my countless number of friends, such as Joshika, Evelien, Davide, and Oscar, my first friends here with whom I struggled through pages of integrals at late hours over burgers and fries. Siya, Momo, Aïcha, and Robbin, thanks for always being there to share literal tea with me. Thank you, Rui, for the laughs, and Kim for putting up with our mayhem and mischief. Eden, I cherish our culinary adventures together. Jerry, thank you for being my brother away from home, and for not only sharing whatever number of brain cells we have, but also a heart.

My friends who are cheering me on from around the world - Marta, Bryan, Bram, Eleonore, Susie, Mari-Liis, and Whitney, thank you for being among the closest in my space family. Andrea, for our night-long phone calls which are like free therapy to me.

Sasha, Clement, Umer, and Jazzy, we've assembled a crew that stood the test of time, from Enschede to Delft or Eindhoven. Goda and Jose, my first true friends, words cannot express how grateful I am for our bond that surpasses all understanding. Alesia, Delft has only made us closer as we slay by day and mentally spar by night. Nina, we grew apart yet stayed close, and you never fail to inspire me every time we catch up. Thank you all for being the family I choose since the early Twente days.

Back home, I would like to thank my life and career mentor Ann Cammaro of Antarexxa Space Global, who continuously shapes me to become a global space pioneer from an underrepresented nation.

Last but not least, to my family for their unwavering support in my lifelong stellar ambitions - none of this would be possible without the encouragement from my parents, siblings, and grandparents.

One last shoutout to whoever installed the free coffee machine on the 13th floor.

Danny Tjokrosetio
Delft, The Netherlands

Abstract

The growing advancement of the space sector has raised further ambitions in solar system exploration while widening access to planetary missions. With Mars being a longstanding destination of scientific interest, a growing demand for surface missions to the planet will be seen. The Martian atmosphere, however, is a challenging environment for entry, descent, and landing (EDL). An entering spacecraft must reduce its incoming hypersonic velocity to acceptable levels for impact or descent by using the atmosphere for deceleration. Due to the low density of the Martian atmosphere, deceleration levels are significantly low compared to Earth entry environments. This atmospheric constraint places limitations on payload size.

To enable a wide range of Mars missions, the challenge of EDL must be addressed through different vehicle architectures. This requires lightweight approaches in entry vehicle design beyond the current state-of-the-art, including protection from atmospheric heating. Heat shields constructed from materials capable of carrying demanding mechanical loads in harsh thermal environments are a promising solution for Mars entry vehicles. This is because the need for a separate load-bearing carrier structure can be reduced, thus providing a relatively lightweight and low-volume aeroshell. Traditional ceramic matrix composites (CMC), including C/C and C/SiC, have attracted international interest for Mars entry applications. Novel ultra-high temperature ceramic matrix composites (UHTCMCs) emerge as good candidates for thermal protection systems (TPS) and hot structures exposed to extreme thermomechanical environments. Their capabilities extend beyond the operational temperature limits of traditional ceramic matrix composites.

The work presented explores the use of (UHT)CMCs in the design of a sphere-cone heat shield for the reference case of a low-mass Mars mission delivering a wind-driven spherical rover to the surface. Through a high-level trade-off, different solutions such as hot structure aeroshells and decelerators, CMC shingles and shells over insulated structures, and a CMC-protected ablator were compared. The hot structure concept was selected for further analysis due to its mission suitability and potential for minimal weight.

Using the Mars Climate Database version 6.1 and a simplified ballistic entry trajectory model, the thermomechanical loads were obtained. The model was verified using data obtained from heritage Mars entry missions. The given loads were used as inputs for thermal and structural numerical simulations using the FEA package Ansys Workbench. The simulations were used to design the heat shield by sizing the TPS layers and assessing thermomechanical stress responses.

Finally, a comparison was made between a baseline CMC and a UHTCMC as the hot structure material. It was found that the baseline CMC saves mass compared to the UHTCMC while allowing a larger stress-based margin of safety. A comparison of heat shields with different size configurations was also made; within a limit of vehicle mass, base diameter, and nose radius, a heat shield with larger vertex angles results in higher mass reduction and thermostructural performance. This work aims to provide a first step towards the exploration of novel structures for Mars entry, enabling a range of robotic and human missions to the red planet.

Contents

List of Figures

List of Tables

Nomenclature

Abbreviations

Abbreviation	Definition
1D	One-Dimensional
2D	Two-Dimensional
3D	Three-Dimensional
ACC	Advanced Carbon/Carbon
ADEPT	Adaptive Deployable Entry and Placement Technology
ARD	Atmospheric Re-Entry Demonstrator
C^3HARME	Next Generation Ceramic Composites For Combustion Harsh Environments And Space
CAD	Computer-Aided Design
C/C	Carbon/Carbon
C/C-SiC	Carbon/Carbon-Silicon Carbide
C/SiC	Carbon/Silicon Carbide
CFRP	Carbon Fiber-Reinforced Polymer
CMC	Ceramic Matrix Composite
CNR-ISTEC	Institute of Science and Technology for Ceramics of the Italian National Research Council
CR	Consistency Ratio
CTE	Coefficient of Thermal Expansion
CVI	Chemical Vapor Infiltration
DLR	German Aerospace Center (Deutsches Zentrum für Luft- und Raumfahrt)
ECSS	European Cooperation for Space Standardization
EDL	Entry, Descent, and Landing
EDV	Entry and Descent Vehicle
ESA	European Space Agency
FEA	Finite Element Analysis
FE	Finite Element
FOLDHOST	Foldable Hot Structure
HIAD	Hypersonic Inflatable Aerodynamic Decelerator
HYDRA	Hybrid Ablative Development For Re-Entry In Planetary Atmospheric Thermal Protection
IML	Inner Mold Line
IXV	Intermediate eXperimental Vehicle
ISRO	Indian Space Research Organization
LSI	Liquid Silicon Infiltration
MCD	Mars Climate Database
MDM	Mars Demonstrator Mission

Abbreviation	Definition
MER	Mars Exploration Rover
MHSHS	Multifunctional Hot Structure Heat Shield
MIRKA	Micro Re-Entry Capsule
MMOD	Micrometeoroids and Orbital Debris
MoS	Margin of Safety
MSL	Mars Science Laboratory
NALT	Non-Ablative Lightweight Thermal Protection System
NASA	National Aeronautics and Space Administration
OML	Outer Mold Line
PICA	Phenolic-Impregnated Carbon Ablator
PIP	Precursor Infiltration and Pyrolysis
RLV	Reusable Launch Vehicle
RCC	Reinforced Carbon/Carbon
SiC	Silicon Carbide
SF	Safety Factor
SPA	Surface-Protected Ablator
TCAT	Thermal Calculation Analysis Tool
TPS	Thermal Protection System
TRL	Technology Readiness Level
TTW	Team Tumbleweed
UHTC	Ultra-High Temperature Ceramic
UHTCMC	Ultra-High Temperature Ceramic Matrix Composite
UTM	Ultimate Tumbleweed Mission

Symbols

Symbol	Definition	Unit
C_D	Drag Coefficient	[-]
Cp	Specific Heat Capacity	[J/kg·K]
E	Young's Modulus	[GPa]
g	Gravitational acceleration	[m/s^2]
h	Vehicle Altitude	[km]
k	Thermal Conductivity	[W/m·K]
m	Vehicle mass	[kg]
P_{crit}	Critical buckling load	[Pa]
q	Heat Flux	[W/cm^2]
R_b	Base Radius	[m]
R_n	Nose Radius	[m]
R_s	Shoulder Radius	[m]
S	Vehicle reference surface area	[m^2]
SF	Safety Factor	-
T_∞	Ambient Temperature	[K]
T_{int}	Internal Temperature	[K]
T_w	Surface/wall Temperature	[K]

Symbol	Definition	Unit
T_{i1}	Interface temperature between skin and insulation	[K]
T_{i2}	Interface temperature between insulation	[K]
T_b	Inner Mold Line/backface Temperature	[K]
V	Velocity	[km/s]
V_c	Circular Velocity	[km/s]
α	Coefficient of Thermal Expansion	[10^{-6}/K]
β	Ballistic Coefficient	[kg/m^2]
ϵ	Emissivity	[-]
γ	Flight Path Angle	[°]
μ	Poisson's ratio	[-]
ρ	Density	[kg/m^3]
$\sigma_{allowable}$	Material allowable stress	[MPa]
$\sigma_{applied}$	Stress due to applied loads	MPa
$\sigma_{thermal}$	Thermal stress	MPa
θ_c	Vehicle half-cone vertex angle	[°]

Constants

Constant	Definition	Value and Unit
g_0	Standard gravitational acceleration of Mars	3.72076 m/s^2
R_m	Equatorial Radius of Mars	3389.5 km
ρ_0	Sea-level atmospheric density of Mars	0.01712 kg/m^3
σ	Stefan-Boltzmann Constant	5.67$\times 10^{-8}$ W/m^2·K^4

1

Introduction

The exploration of our solar system has unlocked a vast array of data and research opportunities previously deemed inaccessible to the scientific community. Recent decades have witnessed a surge in planetary missions, due in part to increasing efforts in international collaboration and the democratization of the space industry. Mars, in particular, is a target of interest due to its proximity and similarities to Earth, and the desire for setting a multiplanetary presence for the human species. Its thin atmosphere, however, poses a challenging environment for delivering payloads to the surface. On one hand, its density enables entry heating, requiring the use of a thermal protection system (TPS). On the other hand, it is too thin to decelerate an entering spacecraft completely. The Martian atmosphere is therefore a major cost driver and a limiting constraint to the size of missions. Advancements beyond current entry, descent, and landing (EDL) systems are critical to enabling a broad range of mission sizes and architectures. Various Mars EDL systems have been explored, such as inflatable and mechanically deployable decelerators and mid-lift-to-drag (L/D) aeroshells [1]. Notable examples of such systems include the Hypersonic Inflatable Aerodynamic Decelerator (HIAD) [2] and the Adaptive Deployable Entry and Placement Technology (ADEPT) [3].

The utilization of structural materials with superior thermomechanical properties such as ceramic matrix composites (CMC) is necessary to enable lightweight entry vehicle design, as well as the realization of a variety of EDL architectures. Such materials are the key to multifunctional entry systems, integrating thermal protection with structural functionality. In addition to being primary materials for heat shields and decelerator panels, they can be used for secondary hot structure components of larger EDL systems. These components may include the nose caps of inflatable decelerators [4] and structural struts of deployable rigid decelerators [5]. For this reason, CMCs can offer mass and volume-saving solutions, potentially increasing mission payload sizes. This family of materials possesses a space heritage, particularly with an interest for use in reusable launch vehicles. This includes carbon-carbon (C/C) as used on the hottest parts of the space shuttle [6], and C/SiC, used on the nose and body flaps of the IXV [7]. An emerging class of materials called Ultra-High Temperature Ceramic Composites (UHTCMC) is being developed to expand this group, with extreme aerospace environments as a primary focus of application [8].

The intrinsic properties of CMCs prompted an interest in their investigation for Mars entry applications, beginning with Europe, where these materials have the highest technological maturity [9]. A C/SiC hot structure heat shield with decelerator was studied for the proposed MarsNet mission to land a trio of measurement stations on the Martian surface [10]. Advanced Carbon/-

Carbon (ACC) heat shields were later studied at Lockheed and NASA for use within various planetary atmospheres [11][12]. In addition, the SpaceX Starship, designed to ultimately become a reusable Mars transport vehicle, currently uses TUFROC thermal protection tiles [13]. These tiles contain an outer layer of C/C composite.

The use of CMCs in the Mars entry environment must be successfully demonstrated to pave the way for use as primary or secondary components on larger EDL and aerobraking missions to the red planet. A small and affordable low-mass mission offers a potential opportunity to prove their operation in the actual environment and provide a benchmark for future designs. For this thesis project, a CMC-based heat shield will be designed for the dedicated entry capsule of the Tumbleweed Mars Demonstrator Mission (MDM), a lightweight mission to test a wind-driven rover prototype on the Martian surface [14]. Team Tumbleweed and the MDM are explained further in section 1.1. This project was conducted with the consultancy of Arceon, a startup company focusing on the development of CMCs for extreme environments. The company specializes in the production of carbon-reinforced carbon-silicon carbide composites (C/C-SiC) using the liquid silicon infiltration (LSI) route. The work performed will contribute to their knowledge of space vehicle design processes using CMCs, as atmospheric entry and hypersonics are applications of interest to the company.

1.1. Reference Mission: The Tumbleweed MDM

Team Tumbleweed (TTW) is a research organization with the goal of widening access to Mars exploration through the development of cost-effective and lightweight spherical rovers. Harnessing the Martian winds, a swarm of 90 rovers measuring five meters in diameter will traverse the Martian globe in the *Ultimate Tumbleweed Mission* (UTM) [15], slated to take place in 2034. This distributed network of highly mobile rovers allows for the collection of surface data across a wide coverage of the Martian globe that has never been spanned by past and present surface missions. Each rover, illustrated in figure 1.1, consists of an outer structure comprising a series of arcs and a stabilized inner structure to support the scientific instruments, housed in payload modules called pods. Six sails mounted on the structure generate the propulsive force from the wind. The rovers will feature a foldable design to be stacked in the EDV.

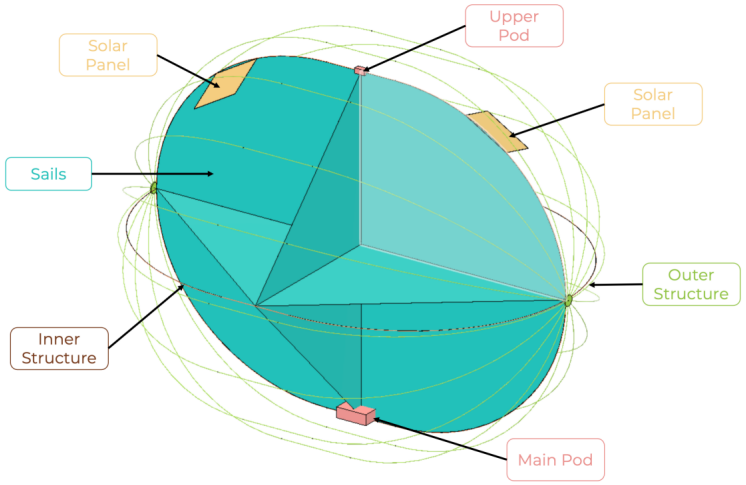

Figure 1.1: Schematic of a Tumbleweed Rover.

The UTM mission concept architecture, including the EDL sequence, is illustrated in figure 1.2. Following launch (1), and cruise stage transfer to Mars (2), the EDV will separate from

the cruise stage and begin atmospheric entry (3). At an altitude of 10 kilometers above the surface, the EDV will be jettisoned, deploying the rovers mid-air (4). The rovers are unfolded as shown in (5), making use of their aerodynamic sails for descent (6) to impact the Martian surface at a velocity of 15 km/s (7). Once on the surface, each rover spreads out across the surface through its 90-sol mobile operations phase (8), whereby it gathers measurements as it rolls along. Following this phase, the rovers then arrive at their terminal stationary phase, gathering local measurements at their respective locations (9) until their end-of-life (10).

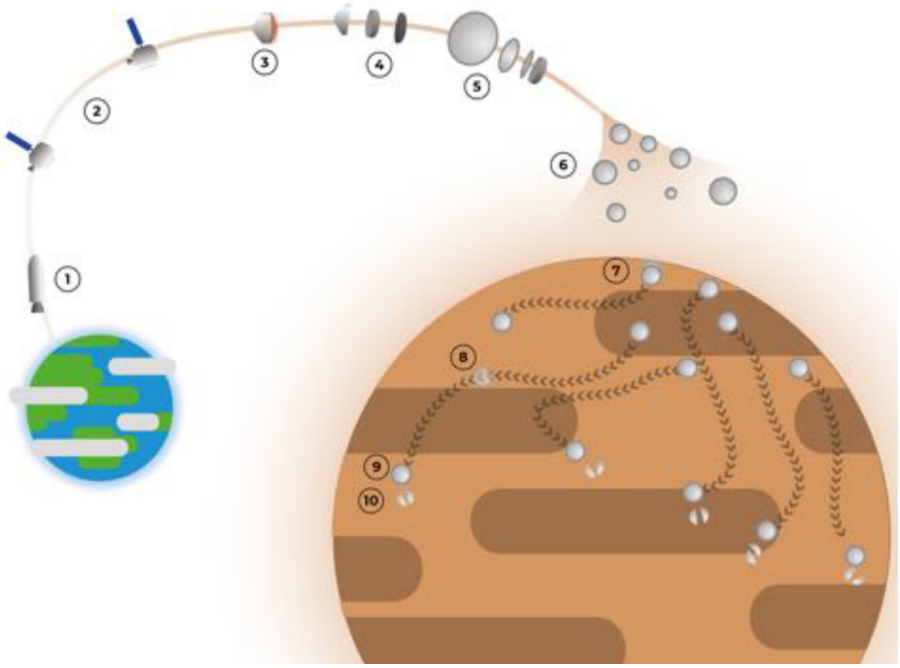

Figure 1.2: Mission concept architecture of the UTM. [15]

Due to the challenges of such a novel mission concept, Team Tumbleweed plans to conduct a representative preceding mission in 2030 to test a single prototype rover in the Martian environment to demonstrate its feasibility and operations. This mission is currently dubbed the *Mars Demonstrator Mission* (MDM) [14]. The rover measures 3.8 m in diameter when unfolded and will weigh no more than 8 kg. As this is a light payload, the MDM is proposed to fly on a rideshare mission to Mars. The phases that follow will be identical to the UTM. A small dedicated EDV, depicted in figure 1.3 will house the folded rover throughout entry. A traditional aeroshell capsule, it consists of a backshell and a heat shield (or forebody/front shield) that adopts the heritage geometry of a conical structure enclosed by a spherical cap. Its vertex angle was initially defined by Tumbleweed to 70° degrees, consistent with most Mars EDV aeroshells. Its base diameter was initially set to 0.6 m. No further details on the EDV's subsystems, including structure, TPS, and materials were specified, giving room for the opportunity to design a novel heat shield.

The MDM's EDL sequence is illustrated in figure 1.4. After detaching from the parent transfer vehicle, the EDV begins entry at an altitude h of 125 km with a flight path angle γ of $-11.916°$ [14]. Its entry velocity is 7.25 km/s. These entry parameters are initial trajectory baseline values derived by Team Tumbleweed without considering the effects of the rideshare mission due to a myriad of unknown factors. These values, however, will be kept throughout the work carried out to obtain the entry loads in chapter 4.

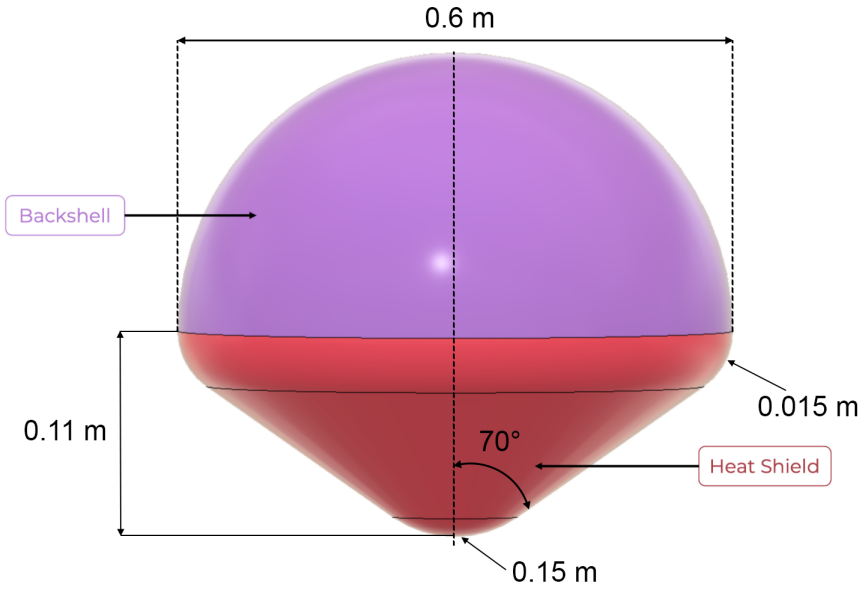

Figure 1.3: Early illustration of the MDM EDV aeroshell with original heat shield dimensions.

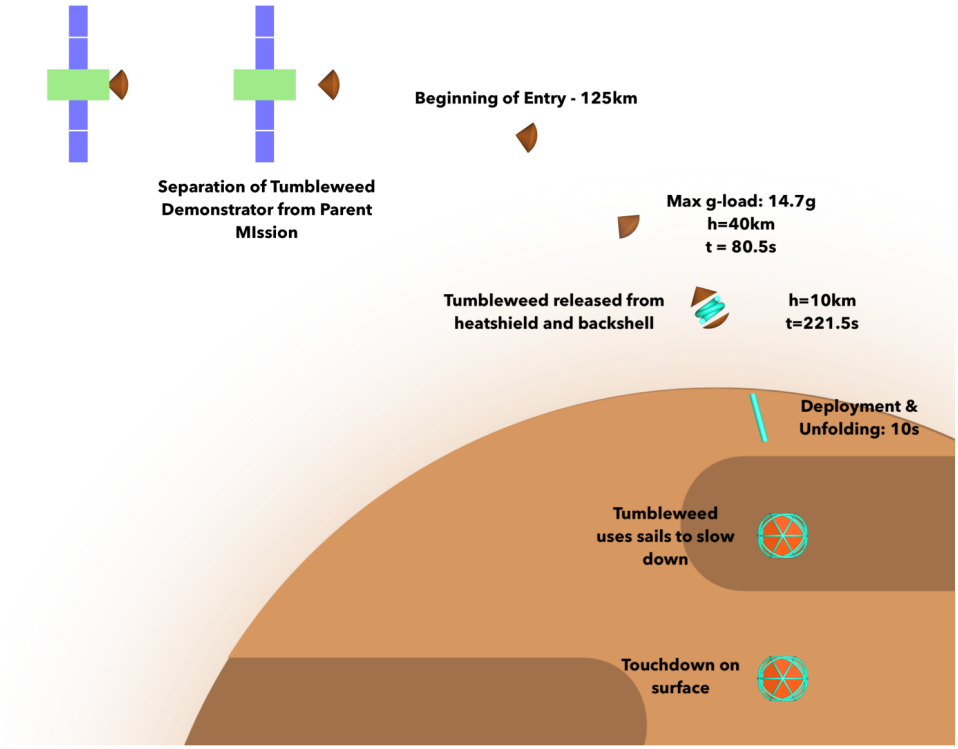

Figure 1.4: EDL sequence of the MDM [14].

1.2. Research Objectives and Methodology

As the aim of this thesis is to design a CMC heat shield for Team Tumbleweed's Mars Demonstrator Mission, the main research question can be defined:
How can a lightweight heat shield combining high thermal and mechanical performance be designed for a small Mars entry capsule using ceramic matrix composites?

This research question can be further broken down into a set of subquestions as stated below:

- *What CMC TPS design concept is suitable for a low-mass Mars mission?*
- *How do changes in vehicle dimensional parameters affect the design of the heat shield?*
- *How does a traditional CMC and a UHTCMC compare with respect to the thermostructural performance of the heat shield while satisfying mass requirements?*

To answer these questions, a list of tasks was identified:

1. **Trade-off and selection of CMC TPS concepts.** Different CMC TPS concepts identified from literature are proposed. A high-level trade-off considering mission suitability, weight, and potential performance will compare the concepts, leading to their elimination or selection. The final selection will be investigated for further analysis.

2. **Define the entry load environment.** Beginning with given vehicle and entry parameters, a trajectory simulation is to be set up on MATLAB to obtain the vehicle's thermostructural load profile throughout the duration of entry and descent. This step is vital in obtaining the input data needed to design and optimize the heat shield for the vehicle and its mission. Comparisons of the heating and load profiles between vehicles with differing heat shield parameters such as semi-vertex angle, diameter, and total mass will be made. A heat shield configuration with modified parameters will be selected for further analysis, and compared with the initially-defined heat shield.

3. **Identify the system design requirements.** Requirements drive system design. Goals for optimization and sizing are set based on limits placed by requirements.

4. **Model and size the TPS using finite element analysis tools.** Thermal and structural models will be set up on the Finite Element Analysis (FEA) software package Ansys Workbench. The thermal model will be used to size the TPS layers to keep temperatures within operational limits under a specified mass constraint. The structural model will combine thermally and mechanically induced stresses to ensure that the CMC heat shield does not fail under expected critical flight loads.

5. **Compare designs using a standard CMC and a UHTCMC material.** The sizing and analysis process will be performed for a TPS using a baseline CMC material and a novel UHTCMC material. The UHTCMC material data entered into the simulations is based on current consistent values reported in literature. The efficiency and suitability of a TPS using traditional and novel CMC skin materials for the particular mission will be compared.

6. **Compare the sized heat shields for two aeroshells.** The TPS for both outer skin materials will be sized for both heat shields with initial and modified parameters identified in task 2. The results for the sized TPS with both skin materials will be compared among the two aeroshells.

1.3. Thesis Outline

This section describes the outline of the thesis report based on the list of tasks. The goals of this work were outlined here in chapter 1, as well as an overview of the reference mission used throughout this work. Chapter 2 summarizes necessary background topics, namely state-of-the-art TPS for Mars entry, an overview of CMCs and their properties for TPS, heritage TPS using CMCs, and studied concepts for Mars missions. Based on this review, several concepts for the heat shield architecture are proposed in chapter 3, which details on the concept selection process. The reference loads obtained from the mission's entry trajectory is discussed in Chapter 4. Following the definition of entry loads, chapter 5 lists the heat shield design requirements based on mission needs and the loads obtained. Important considerations made early in the design process are also given. These considerations include the theory and assumptions made for the thermal and structural analyses, as well as material properties and temperature limits. Chapter 6 discusses the setup and verification of the numerical thermal and structural models, including element type, boundary conditions, and mesh convergence. Sizing of the heat shield and the following thermal and structural analyses are reported in chapter 7. A comparison between the sized TPS for heat shields with different structural materials and dimensions is also made. Finally, conclusions extracted from the work performed and recommendations for future work are summarized in chapter 8.

The flowchart in figure 1.5 illustrates the workflow of tasks and their corresponding chapters.

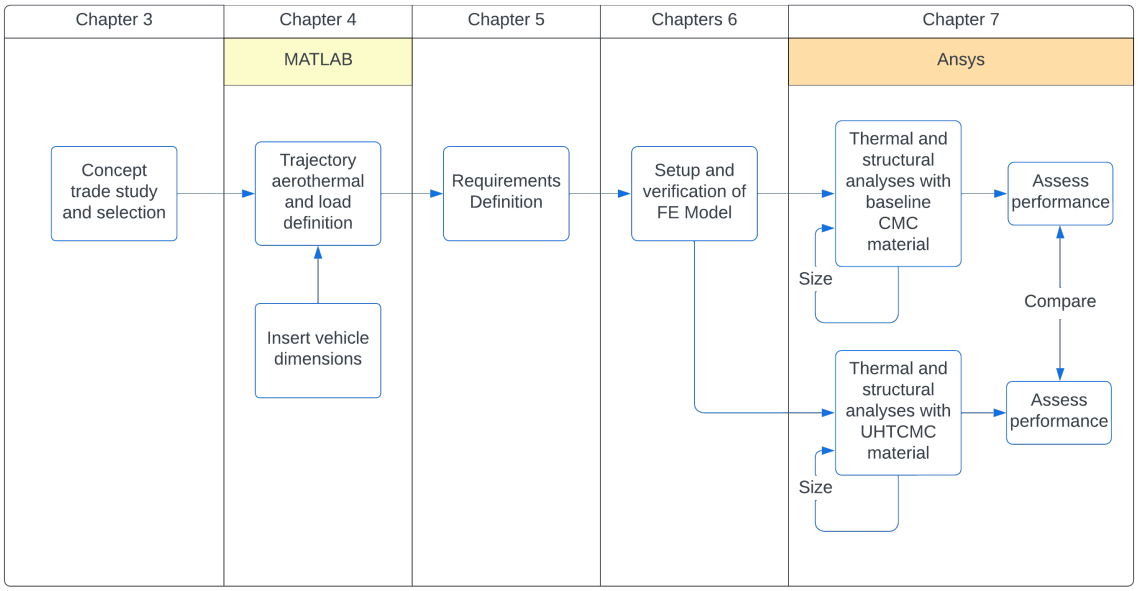

Figure 1.5: Workflow of tasks for the design of a lightweight mission-specific CMC heat shield with integrated thermomechanical functions.

2

Research Background

This chapter aims to familiarize the reader with the necessary topics explored throughout this report, namely on Mars entry and thermal protection systems. First, the general conditions of Martian atmospheric entry and a survey of Mars entry missions are presented in section 2.1. Next, the state-of-the-art of Mars entry TPS through current ablative methods is discussed section 2.2. This is followed by an introduction to CMC materials and their relevant properties for TPS applications in section 2.3. Sections 2.4, 2.5, and 2.6 explain hot structures, passive insulative TPS methods, and hybrid TPS respectively through heritage designs incorporating CMCs and CMC-based designs investigated for Mars missions.

2.1. Mars Entry Environment

The entry environment experienced by a space vehicle highly depends on the body on which it is descending, as well as flight and vehicle factors. These include the planet's shape, atmospheric density and composition, gravitational field, and consequently, vehicle trajectory. The atmosphere provides braking to decelerate the descending spacecraft; its kinetic energy is converted to frictional heat [16]. A thermal protection system (TPS) is therefore required. The heating encountered at the stagnation point of a space vehicle comes from the convection and radiation; radiative heating is traditionally neglected for Mars entry analysis [16].

The Martian atmosphere is mostly of carbon dioxide, and its density is 1% of Earth's atmosphere. The aerodynamic drag experienced by vehicles in a Mars entry environment is much smaller than for Earth. Therefore, it is difficult to use the thin Martian atmosphere for deceleration. Suspended Martian dust in the atmosphere may also impact the heat shield at high velocities [17]; this is dependent on entry time and location, and dust storm presence.
Table 2.1 shows relevant entry data collected from past Mars missions. The values reported consist of entry parameters, vehicle properties, and peak thermal and mechanical loads. This overview provides a benchmark for comparison. All data was taken from NASA's latest Planetary Mission Entry Vehicles Quick Reference Guide [18] unless stated otherwise.

Since the first Mars entry mission, a spherically-blunted cone with a half-angle of 70° has been adopted as the standard geometry for Mars aeroshell forebodies. The current state-of-the-art of Mars entry TPS use sacrificial materials, or ablators, to provide semi-active methods of thermal protection. This is discussed in the following section.

Vehicle	Entry Altitude [km]	Entry Velocity [km/s]	Entry Angle [°]	Vehicle Diameter [m]	Vertex Angle [°]	Ballistic Coefficient [kg/m^2]	Peak Heating [W/cm^2]	Peak Deceleration [G]
Vikings	240.99 and 242.80	4.42 and 4.48	-17.76	3.54	70	60.41 and 61.44	24 [19]	6.86 and 7.20
Pathfinder	130.86	7.48	-14.06	2.65	70	61.50	115 [19]	16.00
Deep Space 2	128.00	6.90	-13.25	0.35	45	36.20	194.00	12.40
MER	126.80	5.39	-10.74	2.65	70	88.96	54.00 [19]	4.78
Phoenix	125.00	5.90 [19]	-13.00 [20]	2.65 [19]	70	65.00 [21]	56 [19]	8.50 [20]
MSL	125.00	5.80	-16	4.50	70	146.00	226.00 [22]	9.70
InSight [23]	125.00	5.54	-12.57	2.65	70	69.00 [21]	45.60 (predicted)	8.13
Beagle 2	120.00	5.40	-15.80	0.92	60	69.90	72.11	-
ExoMars EDM (Schiaparelli)	122.50	5.93	-12.43	2.40	70	74.20	50.00 to 70.00	-
Mars 2020	128.20	5.33	-16.18	4.50	70	143.20	79.00 [24]	10.73
Tianwen-1	125.00	4.70 [25]	-11.53 [25]	3.40 [26]	70	-	-	-

Table 2.1: A table comparing the entry parameters of Mars entry vehicles. Deep Space 2 and the ExoMars EDM were lost. Beagle 2 landed successfully but failed to operate on the surface [18].

2.2. Ablative TPS

Ablators are for single-use systems where large heat fluxes and short entry times are expected [9]. In addition to poor thermal conductivity, their excellent thermal performance can be owed to multiple reactive mechanisms. An ablator absorbs incoming heat to decompose; a protective barrier of gases forms. These gases consist of pyrolysis gases that remove heat from the ablator to its surroundings, which further reduce the convective heat flux by reacting with the boundary layer. In addition, the gaseous products blow the incoming heat away as they flow. These mechanisms are illustrated in figure 2.1. Ablative materials are typically polymer-based [27].

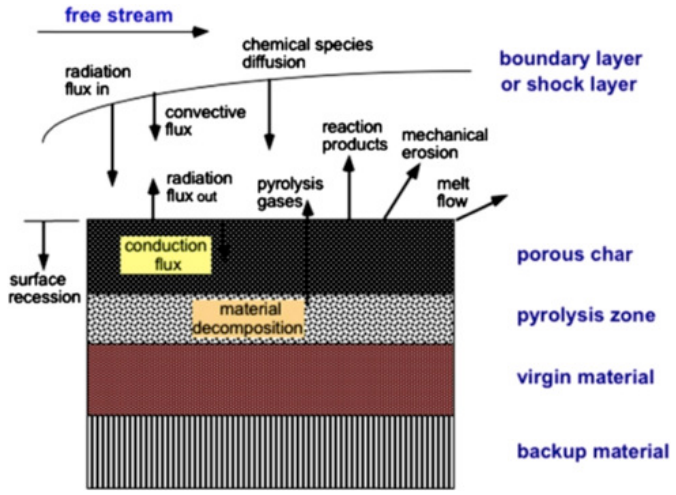

Figure 2.1: Schematic diagram of an ablative thermal protection system with ablation mechanisms.[28].

2.2.1. Ablative TPS Heritage for Mars Missions

SLA-561V Heat Shield

Super Lightweight Ablator-561V (SLA-561V) is a Lockheed Martin-developed ablator. It is composed of phenolic honeycomb cells which are filled with an elastomeric silicone-based composition, which includes cork, glass fibers, and phenolic microballoons [22]. SLA-561V was selected and used as the TPS material to manufacture a single-piece heat shield for all US Mars landing missions before the Mars Science Laboratory (MSL) [29].

As entry vehicles increase in size, the application of SLA-561V consequently increases in difficulty, as clearly demonstrated during the heat shield development process of the Mars Science Laboratory. The SLA-561V TPS is only appropriate for entry vehicles that encounter laminar flow conditions at their stagnation point during peak heating [30]. MSL, being larger than all its predecessors, encountered a turbulent environment. Under the MSL flight envelope, including combined shear, SLA-561V showed behavioral anomalies in ablation that were not well-understood, and even displayed devastating results. This forced the switch to an alternative ablator [31] [22].

Tiled PICA

Phenolic-Impregnated Carbon Ablator (PICA) is made of a carbon foam-like substrate called FiberForm infused with a phenolic resin. Due to its heritage on the highly-demanding Stardust mission, PICA was ultimately selected as the MSL TPS material, and consequently, for the identical Mars 2020 heat shield [33]. The development of the MSL TPS outlined the challenges

Figure 2.2: Construction of the monolithic SLA-561V heat shield for the Mars InSight lander [32].

of adapting ablators towards specific missions [22].

Due to PICA manufacturing size constraints and the MSL entry vehicle's diameter, a monolithic heat shield cannot be constructed. PICA was applied in tiles, requiring fillers between tile gaps. The tiles were directly bonded to the aeroshell substructure. The final design resulted in 113 PICA tiles with 27 unique geometries.

Ablators such as PICA, however, have a low strain-to-failure rate, making them brittle and prone to defects. This affects ablator tile thickness, size, and application method [34]. The poor properties of ablators also prompt the use of a thick substructure to avoid load transfer to the ablator [12].

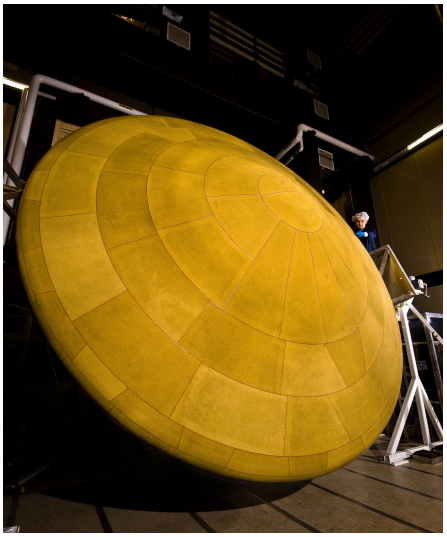

Figure 2.3: The tiled-PICA heat shield for the Mars Science Laboratory [35].

While ablators display strong heritage for Mars entry, they present themselves with numerous design challenges, which notably increase with vehicle size. Alternative thermal protection methods and materials have been investigated to overcome these limitations.

2.3. CMC Materials for Thermal Protection Systems

TPS design beyond ablative and flexible methods call for the use of lightweight materials with high-temperature structural capabilities, especially in critical areas with peak thermal stresses. On rigid systems where volume and mass are concerned, thin-walled primary structures resistant to high temperatures are imperative. Given the current availability of materials, the CMC material family is the key to unlocking such thermal structures for planetary entry. This is due to their ability to retain, and even improve, their mechanical properties at high operating temperatures without significant distortion, while being lighter than high-temperature metals [36].

2.3.1. Properties of CMCs

As composites, CMCs consist of a reinforcement phase and a ceramic matrix phase. The ceramic matrix phase raises the operational temperatures and oxidation and thermal shock resistance beyond other composite families such as polymer and metal matrix composites. The reinforcement phase improves the mechanical properties of ceramics by enhancing strength and fracture toughness.

Carbon and silicon carbide (SiC) fibers are most commonly used for reinforcement in high-temperature appplications [37]. Despite the superior oxidation resistance of SiC fibers, carbon fibers are typically used for TPS due to higher specific strengths at elevated temperatures, in addition to lower material costs [9] [38]. Available fiber architectures are short fibers, 1D reinforcements, 2D fabrics, and 3D braids; short fibers typically give higher composite densities, while continuous fibers correspond to higher specific strengths and lower densities [37]. For TPS applications, 2D fabrics in a quasi-isotropic layup are typically used to reduce deflections due to high thermal gradients [39] [40].

Clear distinctions are made for CMCs based on their matrix materials; oxide CMCs typically use alumina matrices, while non-oxide CMC matrices traditionally contain carbon and/or SiC. Non-oxide CMCs exhibit superior retained mechanical properties at higher temperatures compared to oxide CMCs [41]. However, carbon-based CMCs suffer from poor oxidation resistance; C/C composites, which were first developed in the 1950s, cannot be used in oxidizing atmospheres above 450°C unless oxidation-resistant coatings are applied.

To further increase the operational temperature and lifetime of C/C, silicon carbide matrices were first introduced in the 1970s [37]. Carbon-reinforced silicon carbide CMCs comprise C/SiC and C/C-SiC. In C/SiC composites, carbon fibers are embedded in a completely SiC-filled matrix; processing typically begins with a porous C/C preform, and the carbon matrix is completely replaced by SiC using gaseous reactants or molten silicon, depending on the manufacturing route. C/C-SiC consists of a carbon and SiC-containing matrix; the C/C preforms are tailored to ensure the presence of carbon in the final matrix composition for better mechanical properties. These SiC-containing CMCs, however, are still limited by the active oxidation temperature of SiC, and may require an additional protective coating.

In this work, C/C-SiC will be used as a baseline CMC given Arceon's affinity for the material. Due to its availability of data, the properties of the DLR standard material C/C-SiC XB, where XB stands for "experimental basic", will be used in particular. In addition to serving as a heritage material in spacecraft design representative of Arceon's products, C/C-SiC XB has been extensively studied and characterized with experimental data for over two decades and considered a standard baseline [42] [39]. This allows for using a homogenized material model for thermal and structural analysis simulations later in this work. The properties of C/C-SiC XB

have been used in multiple CMC TPS design projects; these projects include the nose of the EXPERT entry vehicle [43], the SHEFEX-II TPS [44], and the Stratofly TPS [45].

2.3.2. C/C-SiC XB

C/C-SiC XB uses 2D-woven fabrics in a 0°/90° orientation made of polyacrylonitrile (PAN) carbon fibers. The liquid silicon infiltration (LSI) manufacturing process is used; it begins with the production of a carbon fiber-reinforced plastic (CFRP) preform. The fabrics are stacked and infiltrated with a phenolic resin. After pyrolysis in an inert environment above 900°C, the CFRP turns into a highly porous C/C preform. Finally, the preform is infiltrated with molten silicon in a vacuum above 1420°C, which reacts with the carbon fibers to form SiC. A weak fiber-matrix bond is needed to obtain high mechanical properties; therefore, the PAN fibers may be coated to ensure no direct contact between the fibers and the highly reactive silicon. The LSI method allows near-net shaping and the production of thin-walled, large, and complex geometries, allowing quicker and cost-effective production compared to other manufacturing methods. With LSI, wall thicknesses between 1 to 70 mm have been manufactured [46].

2.3.3. UHTCMCs

In recent years, ultra-high temperature ceramic composites (UHTCMCs) have been developed to overcome the oxidation and service temperature limitations of traditional CMCs through the addition of a UHTC to the matrix [47]. UHTCs, which include carbides and borides of zirconium and hafnium, possess an extraordinary range of operating temperatures. These materials can reach temperatures above 2273 K with minimal or no oxidation and erosion [48].

The C^3HARME project (Next Generation Ceramic Composites For Combustion Harsh Environments And Space) [8] funded by the European Union has provided a significant contribution to the available research on UHTCMCs. The project focuses on, but is not limited to, application to TPS and rocket nozzles. A consortium of 12 European institutions participates in C^3HARME to develop UHTCMCs through different manufacturing methods. To the author's knowledge, researchers at the Institute of Science and Technology for Ceramics of the Italian National Research Council (CNR-ISTEC) in Faenza, Italy, have produced UHTCMC samples with the most consistent range of values published [49].

CNR-ISTEC's particular material of focus is C/C-ZrB_2SiC, manufactured with Spark Plasma Sintering (SPS). First, wet ball-milling is used to create a ZrB_2 and SiC powder mixture, which is dried using a rotary evaporator. A slurry is made using polyacrylate resin, which is then used to infiltrate a stack of unidirectional carbon fabrics in a 0°/90° orientation. The preform is sintered in an SPS furnace to produce the resulting UHTCMC. Complex axisymmetric shapes for rocket nozzles have been produced using this method; however, post-machining was required as only thick manufacts can be produced by SPS. The current diameter of manufacts is also limited to 400 mm. While the heat shield diameter in this work is larger than this value, the use of UHTCMCs as a skin material is merely an investigation of its effects on the TPS design. The size constraint is also expected to grow throughout the decade as demands for such materials may increase. As of the time of writing, the composites have a TRL of 5 for TPS applications.

The interest toward a ZrB_2 UHTC phase is due to its balance between density, high-temperature behavior, and cost [50]. A small addition of SiC to the matrix phase enhances oxidation protection. Based on the results collected throughout ISTEC's division within the project, a baseline composition consisting of 10%-volume SiC and a fiber volume fraction between 40 to 50% is typically employed [51] [52]. Short, and 2D and unidirectional continuous fiber architectures

have been investigated. The CNR-ISTEC C/C-ZrB_2-SiC material with short fibers and a 2D 0°/90° fiber arrangement have undergone multiple thermal and mechanical tests in representative highly demanding re-entry environments. The recorded mechanical and thermophysical properties at room and elevated temperatures of these composites are consistent across multiple papers published by the institution [49] [53] [54].

2.3.4. Applications of CMCs toward TPS types

The properties of CMCs for TPS design are mainly regarded with spaceplane-type reusable launch vehicles (RLVs), which currently use passive TPS methods. This is not only due to their attractive thermostructural properties, but also their low ablation rates under RLV entry conditions, promising continuous-use applications. TPS with CMCs as primary materials, however, have also been applied for ballistic single-use missions through passive and hybrid methods combining ablative materials and CMCs. The following sections will provide an overview of CMC-based architectures for each TPS type through heritage missions, as well as proposals for Mars missions wherever necessary. Passive TPS types comprise hot structures and insulated structures, which will be further elaborated in sections 2.4 and 2.5 respectively. Hybrid TPS heritage will be explained in section 2.6.

2.4. CMC Hot Structures

A TPS consisting of a primary load-carrying structure directly exposed to entry heating is called a hot structure. A hot structure is characterized by high surface emissivity [27]; a sizable portion of the incoming heat is rejected via radiation. This enables exposure to higher heat fluxes for longer periods. A hot structure schematic in figure 2.4. As hot structures must maintain structural integrity while enduring aerodynamic heating, the use of a high-temperature structural material is required. Within the current availability of materials, CMCs are primarily considered for this application. Examples of hot structures are the reinforced carbon-carbon (RCC) leading edges of the Space Shuttle, and the C/SiC control surfaces of the IXV spaceplane. If protecting internal components, lightweight insulation is typically used below the hot structure to delay the further conduction of heat.

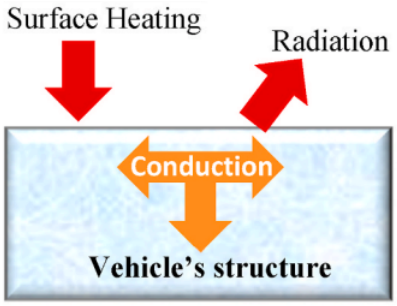

Figure 2.4: Schematic of a hot structure [27].

2.4.1. CMC Hot Structure Heritage

The development of CMC TPS was born out of interest in RLV and spaceplane applications. C/C, which was used as hot structure components for the nose and leading edges of the Space Shuttle, had military beginnings in the United States [55]. Meanwhile, carbon-reinforced CMCs with SiC-containing matrices saw primary development in Europe [9].

The first instance of TPS design with C/SiC was for hot structure components on the Soviet space shuttle Buran. Its nose cap and leading edges were made of a specially-developed

C/SiC material called *Gravimol*, manufactured with the LSI process [56] [57]. A viscous anti-oxidative molybdenum silicate coating was applied manually with a brush. The coated Gravimol C/SiC material was flight-proven when the orbiter successfully flew one autonomous mission in 1988. The opportunity to investigate its reusability, however, dissolved along with the Buran program and the Soviet Union. Figure 2.5 shows a rendering of Buran, highlighting its C/SiC hot structure components.

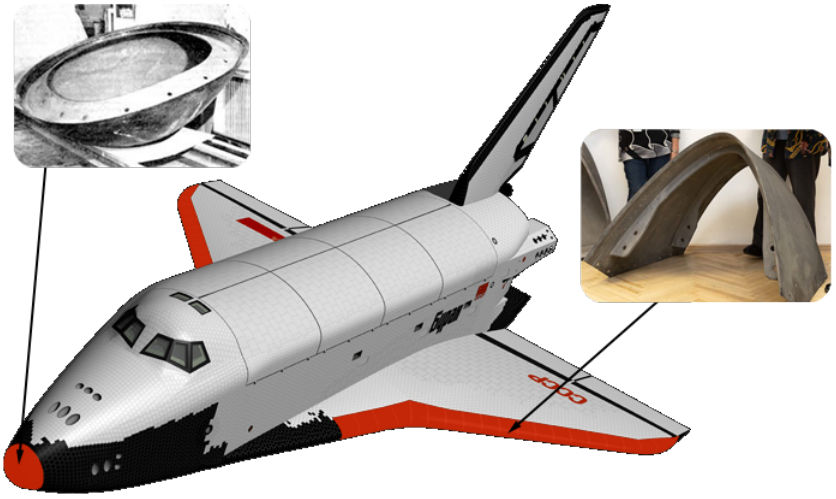

Figure 2.5: C/SiC nose cap and leading edges (highlighted in red) of the Soviet Buran space shuttle [57] [58].

C/SiC was heavily used in the TPS design of the canceled European space shuttle Hermes [59]. These parts include its leading edges, wingbox, and a hot skin antenna. Coated C/C and C/SiC were both considered for use as the nose cap material. The knowledge gained from Hermes paved the way for the integration of CMC TPS components in further spaceplane projects in Europe.

2.4.2. CMC Hot Structures for Mars Entry

Beginning in Europe, CMC hot structures have been considered for Mars missions as early as 1992 [60]. The European Cooperation for Space Standardization (ECSS) considers CMCs suitable for Mars entry, with the added benefit of low pollutive gas production as opposed to ablators [39]. This allows more direct measurements of Mars entry plasma flows. In addition, CMCs offer erosion resistance due to regolith impact, as well micrometeoroids and orbital debris (MMOD) in the space environment.

MarsNet Aeroshell

Dassault Aviation incorporated C/SiC into the forebody design of the MarsNet entry vehicle. The aeroshell, shown in figure 2.6, was to land a network of surface penetrators following an unguided ballistic entry. Its 2-meter forebody consists of a spherical front shield measuring 1.25 m in diameter and an aft conical decelerator with a 60° half angle.

In the first phase of the project, the front shield and decelerators form a monolithic heat shield. After comparisons with a traditional ablative system, a hot structure concept was selected, showing a mass reduction of 10 kg [60]. It consisted of a C/SiC shell with internal Kaowool (alumina-silica) insulation under the front shield. For a maximum stagnation heat flux of 55 W/cm^2, the sized heat shield had a C/SiC skin of 1.8 mm and an insulation thickness of 37

mm. The maximum surface temperature was approximately 1300°C. A more complex semi-integrated ablative front shield and C/SiC decelerator was later explored, with pressure tests revealing leakage issues in the interface between the two components [10].

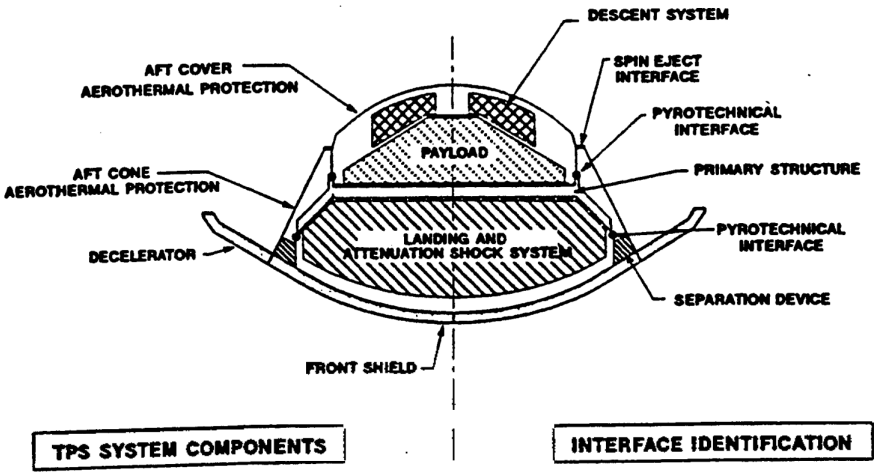

Figure 2.6: MarsNet aeroshell configuration [60].

FOLDHOST Decelerator

In the early 2000s, the European Space Agency (ESA) identified the need for larger heat shields to land human Mars mission architectures. In response, Trabandt et al [61] [62] proposed a foldable hot structure (FOLDHOST) decelerator comprising CMCs. The concept, illustrated in figure 2.7, consists of a central heat shield, a cold structure covered in ablator or CMC tiles, and 20 C/SiC panels with a wall thickness of 2.4 mm making up the foldable decelerator. A trade-off analysis showed that there were mass savings compared to an ablative decelerator. Despite suggestions for further investigation, the project was not continued.

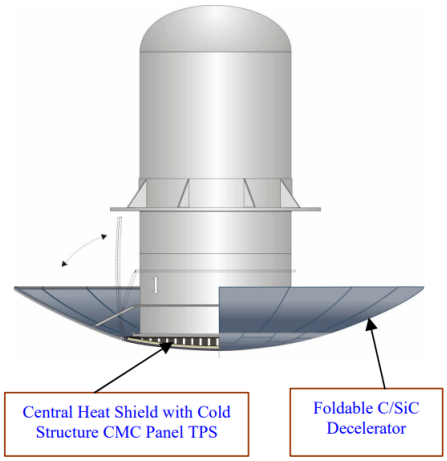

Figure 2.7: Foldable hot structure concept [61].

American Developments in Monolithic Hot Structure Aeroshells

To investigate mass-saving solutions for planetary exploration vehicles, the United States sought the use of their matured C/C composites to design a single-piece heat shield. In the

last half of the 2000s, Munk et al [11] at Lockheed designed and constructed a 2-meter 70° sphere cone heat shield using advanced carbon-carbon (ACC). An integrated stiffener system consisting of one ring frame and six radial stringers was co-cured onto its skin. This breadboard aeroshell is shown in figure 2.8.

Figure 2.8: Internal view of Lockheed's carbon/carbon hot structure heat shield, displaying its integrated stiffeners [11].

The heat shield was designed for use in Venus, Earth, Mars, and Titan conditions, with mass reductions between 15 to 30% compared to traditional ablative systems [63]. The prototype was tested under Titan aerobraking conditions, bringing it to a TRL of at least 5. Its thermal design consisted of a thin external oxidation-resistant coating and internal fibrous carbon insulation to keep the inner mold line (IML) at optimal temperatures. Its total areal density measured 23.7 kg/m^2. Thermal tests showed that the hot structure heat shield was able to withstand a maximum heat flux of 300 W/cm^2, and up to 700 W/cm^2 if a substructure is added.

Walker et al [64] [12] at NASA's Langley Research Center continued the development and scale-up of ACC aeroshells via the Multifunctional Hot Structure Heat Shield (MHSHS) project, also called the HoSt (Hot Structure) aeroshell. Applications specific to future Mars entry missions were studied to enable precision landings by weight savings. A lightweight and flexible blanket consisting of fibrous insulation developed at the Ames Research Center was used underneath the ACC shell. A schematic of the MHSHS concept is illustrated in figure 2.9.

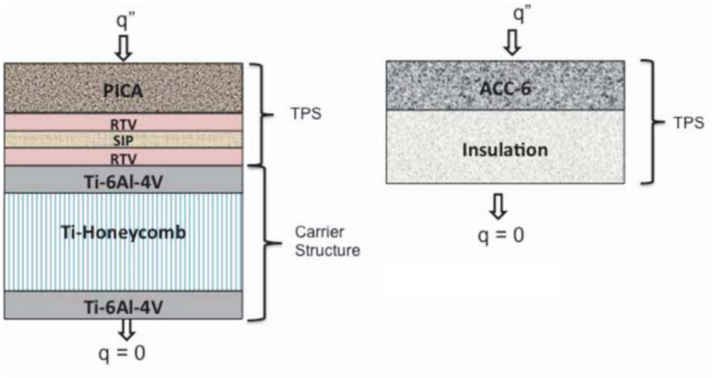

Figure 2.9: Through-the-thickness schematic of an ablative TPS with substructure (left) and the HoSt hot structure aeroshell (right)[64].

A structural and thermal sizing analysis using the HoSt concept was done for an MSL-sized heat shield. Three trajectory cases with maximum heat fluxes of 100, 150, and 200 W/cm^2 were analyzed. For all three cases, HoSt shows a volumetric efficiency of 200% compared to an ablative system. For the 150 W/cm^2 case and a stress safety factor of 1.5 applied, a 29% reduction in areal density is obtained compared to an ablative system.

2.5. CMC Insulative TPS

A passive insulative TPS concept consists of a primary structure, or cold structure, protected by an additional low-ablative external layer that insulates the incoming heat while re-radiating most of it back to space, as illustrated in figure 2.10. It is typically used in a moderate heat flux environment where shorter heat exposure periods are required, such as RLVs and space-planes [9]. The most well-known example of an insulated structure is the Space Shuttle, protected by external insulating blankets and tiles [27].

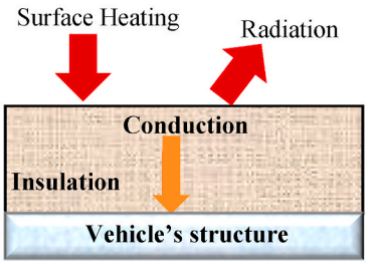

Figure 2.10: Schematic of an insulated structure [27].

The external layer over the primary structure can serve the thermal insulation function only (and mechanical loads to a small extent), such as the Space Shuttle's tiles and blankets. It can also be a multilayered system consisting of an external structural skin to assist the substructure with additional load-bearing functions, thereby reducing the necessary thickness of the substructure. Lightweight insulation between the external and internal structure blocks the incoming heat. As with the hot structure TPS, CMCs are often employed for the external skin.

2.5.1. CMC Insulative TPS Heritage

From Hermes to Space Rider: The C/SiC Shingle

C/SiC components were designed not only for hot structure components of the Hermes shuttle, but also constitute a large portion of its TPS through aerodynamic surface tiles, or shingles, to insulate the airframe. This shingle architecture fixes the C/SiC shingles onto the substructure using a standoff attachment system. The standoff system accommodates the CMC's thermal expansion while transferring loads between the shingles and the cold structure. The shingle architecture used today was improved by Pichon et al for the Pre-X project [65], illustrated in figure 2.11a.

Pre-X evolved into the Intermediate Experimental Vehicle (IXV), shown in figure 2.11b. The IXV TPS consisted of 30 C/SiC shingles with integrated woven stiffeners, comprising the windward side of the vehicle [7]. The nose cap was a monolithic C/SiC piece. The nose cap was attached to the structure the same way as the shingles, with integrally manufactured stiffeners fastened to standoffs. Following a successful suborbital mission in 2015, the IXV's shingle TPS will be implemented on the Space Rider program, currently slated for a 2025 maiden launch [66]. The shingle architecture was also employed on SHEFEX-II, where surface temperatures above 2600 K during its flight were estimated [44].

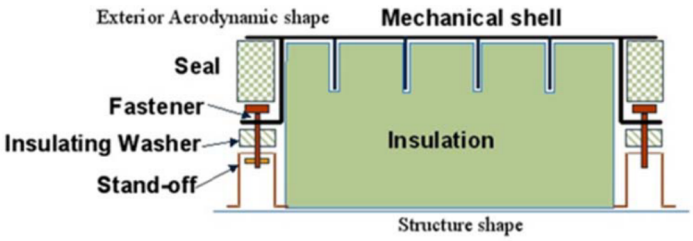

(a) The Pre-X C/SiC shingle architecture [65].

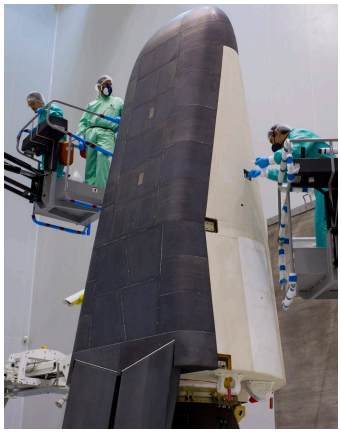

(b) Technicians prepare the IXV for launch. The black components are the C/SiC shingles [67].

Figure 2.11: The C/SiC Shingle TPS for European spaceplanes.

C/C-SiC Nose Caps

LSI-manufactured monolithic C/C-SiC structures were first developed by DLR for the nose cap of the X-38 vehicle [68]. The nose, measuring 740 mm in diameter, was an answer to the demand for a structure with a surface temperature capability up to 2023 K. This was beyond the capability of Space Shuttle nose caps up to 1773 K. The nose was joined to the spaceplane's cold structure using a lever attachment system to support radial thermal expansion. The larger nose cap of the EXPERT vehicle had 16 hat-shaped C/C-SiC components joined in-situ on the edge of the nose, with a metallic leaf spring fastened on top and joined to the cold structure. The flexibility of the leaf spring accommodates radial thermal expansion. The EXPERT nose with installed leaf springs is shown in a test setup in figure 2.12. A thin SiC coating of not more than 120 μm was applied for oxidation protection [69].

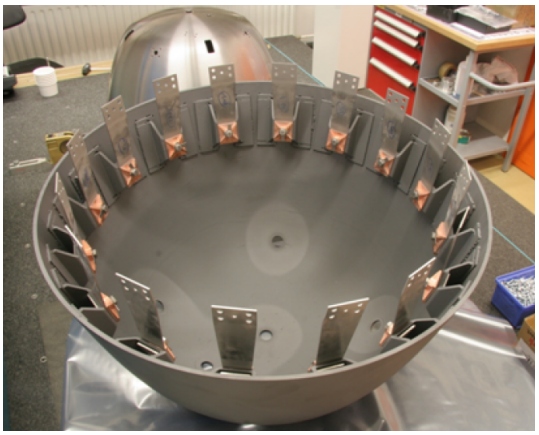

Figure 2.12: EXPERT nose cap with leaf springs [70].

Genesis Sample Return Capsule Heat Shield

NASA's Genesis mission debuted a flown insulated capsule forebody structure with a CMC skin in 2004. As it was a solar wind sample return mission, a substructure is necessary to absorb impact loads. Excluding the graphite-epoxy composite substructure, the TPS measured 60 mm thick: a 38 mm-thick C/C skin backed by a 22 mm-thick carbon foam-like FiberForm insulation [18][71]. With a base diameter measuring 1.5 m and a sphere-cone geometry with

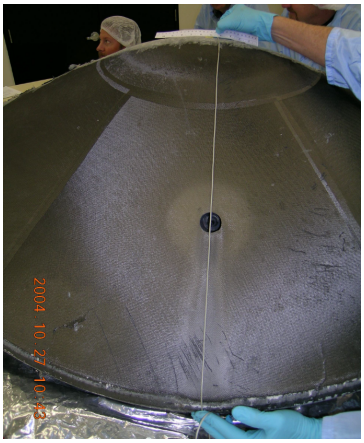

(a) The Genesis C/C forebody recovered from the wreckage.

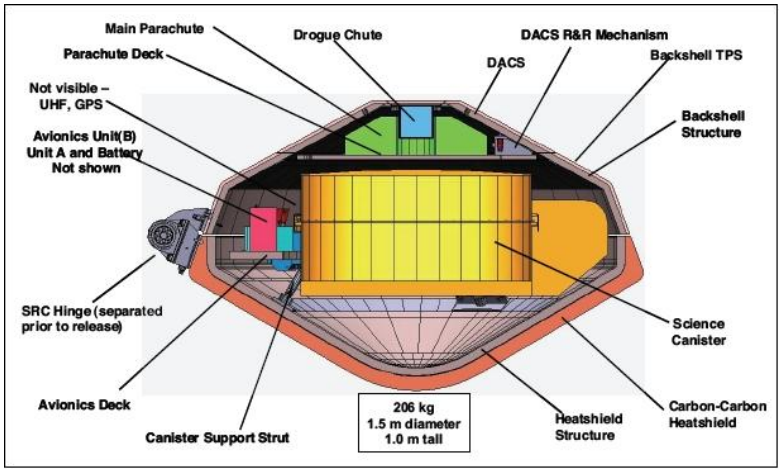

(b) Cross section of the Genesis sample return capsule.

Figure 2.13: The Genesis entry vehicle and its CMC forebody heat shield.

a 59.18° half angle, the heat shield successfully protected the spacecraft from a maximum stagnation heat flux of approximately 700 W/cm^2. The spacecraft, however, crashed as its parachute failed to deploy due to a faulty deceleration sensor. Fortunately, the payload survived and was successfully retrieved. The recovered heat shield and a cross section of the Genesis capsule are shown in figures 2.13a and 2.13b respectively.

2.5.2. Insulative CMC TPS for Mars Entry

Suzuki et al [72] developed the Non-Ablative Lightweight TPS (NALT) for the heat shield of the Mars Aeroflyby Sample Collection mission. Similar to the Genesis heat shield, it consists of a monolithic SiC-coated C/C shell, carbon foam insulation, and a CFRP-aluminum sandwich substructure. The insulation, however, uses a novel jigsaw-like assembly. It is bonded to the shell with a high-temperature graphite adhesive, and with epoxy to the substructure. A schematic of the concept is shown in figure 2.14. A 0.6 m-base diameter sphere-cone breadboard model was manufactured for vibration, shock, and infrared lamp and arc-jet heating tests. The tests brought NALT to a TRL of 4, and it was concluded that the concept is potentially feasible for the mission.

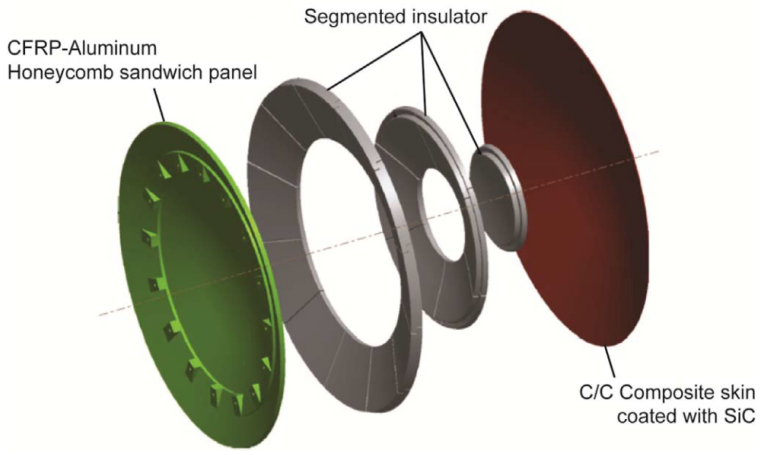

Figure 2.14: Schematic of the NALT heat shield [72].

2.6. Hybrid CMC TPS

2.6.1. SPA: The Surface-Protected Ablator

A small C/SiC experiment on ESA's Atmospheric Re-entry Demonstrator (ARD) was the first application of a CMC to an entry capsule [36]. However, the German Micro Re-Entry Capsule (MIRKA) was the first to fully use a CMC-based TPS, using a hybrid design called the Surface-Protected Ablator (SPA) [73]. A thin external C/SiC shell was adhesively bonded over a 30 mm-ablative layer, which was bonded onto a 1 mm-thick carbon fiber composite substructure. Manufactured by DASA-Dornier through the polymer-infiltration and pyrolysis (PIP) method, the C/SiC skin was designed to protect the ablator from erosion, particle abrasion, and intense heat fluxes and aerodynamic pressure [39]. The C/SiC skin had a primary thickness of 1.3 mm, but gradually increased up to 3.5 mm at the stagnation point. Flown in 1997, SPA successfully protected the 1-meter diameter spherical capsule without any sign of damage or debonding. A schematic of the SPA design is illustrated in figure 2.15a, and the MIRKA capsule with the installed SPA is shown in figure 2.15b.

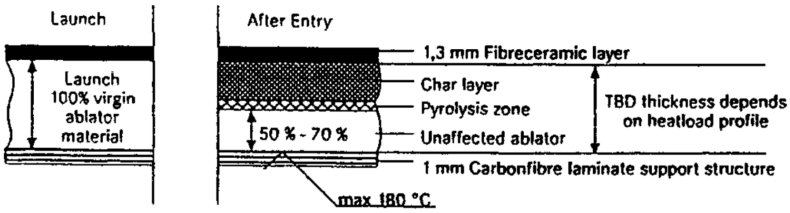

(a) Schematic of the Surface-Protected Ablator [73].

(b) The MIRKA capsule [74].

Figure 2.15: The SPA TPS of the MIRKA capsule.

3

Concept Generation

This chapter covers the selection of the most feasible heat shield architecture concept per the mission. Five concepts are proposed. The weakest concept is first eliminated in 3.2.1. Following a strength and weaknesses analysis of the remaining concepts in 3.2.2, two options were chosen for a further trade study in 3.2.3 to select the final design concept. From this chapter on, the terms ”TPS” and ”heat shield” will be used interchangeably, and refers to the entire forebody of the aeroshell.

3.1. Design Options

The first step in the concept generation and selection process is to assess the possible design candidates based on the literature study in chapter 2. Three primary categories based on TPS classifications are identified, which are broken down into a set of design candidates with their respective examples shown in chapter 2.

- Hot structure: the CMC skin is a primary load-bearing structure and is directly exposed to entry heating.
  - Monolithic Forebody (Phase A MarsNet Heat Shield, Lockheed/NASA HoSt)
  - Deployable Decelerator (FOLDHOST)
- Insulated structure: the CMC skin reduces the loads on the primary structure with thermal insulation sandwiched between them. Cores or standoff attachment systems between the skin and substructure act as interfaces for load transfer. In the case of a monolithic shell over an insulated structure, adhesive bonding may be used in lieu of mechanical attachments.
  - Monolithic (Genesis Heat Shield)
  - Shingle (IXV Windward TPS)
- Hybrid Ablative
  - Surface-Protected Ablator (MIRKA TPS)

For clarity, a design options tree illustrating the concept families is shown in figure 3.1.

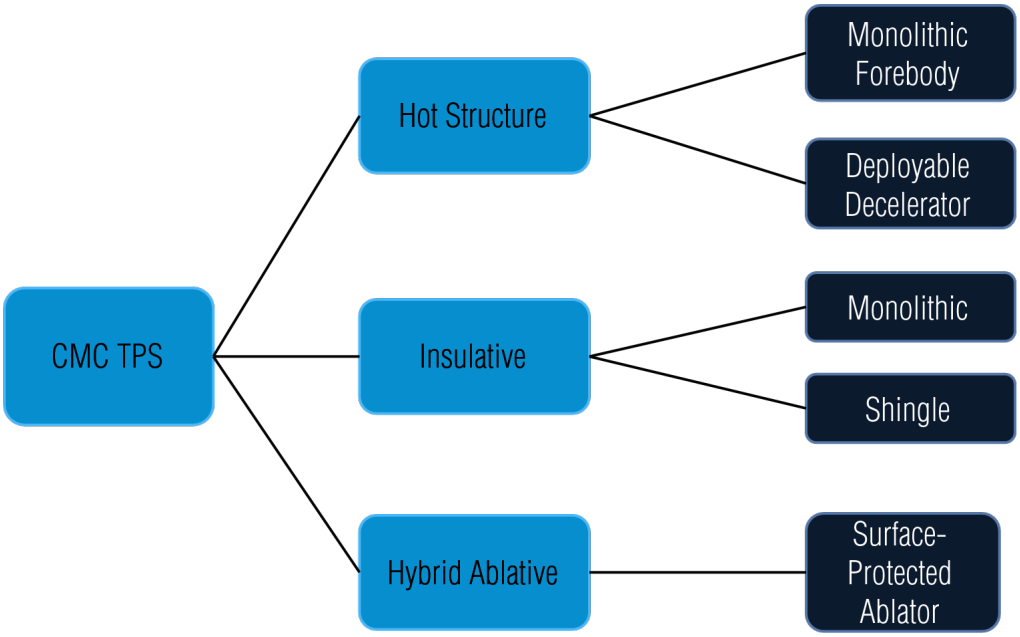

Figure 3.1: Design options tree

3.2. Concept Selection

3.2.1. Elimination of clear losing concepts

The deployable decelerator concept can be immediately eliminated as it violates the vehicle's overall configuration: a classic aeroshell capsule. In addition, its mechanisms and number of subcomponents add to the complexity and weight of the system. In the context of MDM, the performance of the Tumbleweed rover's sails throughout atmospheric descent is critical to measure. To properly record and assess this data, it is desired for the rover to not receive assist in deceleration from additional braking devices such as a decelerator. Assessing the rover's survivability and robustness in a more severe descent environment ensures the Tumbleweed's versatility within a variety of missions.

3.2.2. Analysis of Strengths and Weaknesses

Following the elimination of unfeasible concepts, four concepts still remain. A comparison of these concepts with respect to their strengths and weaknesses will allow the simple elimination of two concepts. The remaining two concepts will enter a further trade study. This analysis is presented in table 3.1.

Concept	Strengths	Weaknesses
Monolithic Hot Structure	No substructure required - saves mass and volume.	• No flight heritage (TRL 5 [11])
Monolithic Shell over Insulated Structure	• Has flight heritage for entry capsules from Genesis [18] • Adhesives may be used in lieu of mechanical fasteners to save mass.	• Additional mass from substructure
Shingle Architecture	• Has flight heritage - flown as IXV's windward TPS and the primary TPS of SHEFEX II. • Tiles present less manufacturing limitations compared to larger monolithic shells.	• Mismatch of thermal expansion between shell, attachment assembly, and substructure due to dissimilar materials. • Gap fillers/seals required to fill discontinuities between tiles • Added complexity and mass due to the attachment assemblies required for all tiles • Added thermal conductivity from the attachment system to the substructure
Surface-Protected Ablator	• Has flight heritage - flown on MIRKA [74] • High interest for planetary probes and capsules • Excellent thermal performance from ablator	• Added challenges, time, cost from ablator manufacturing and bonding • Additional mass from substructure

Table 3.1: Concept comparison table.

From table 3.1, the shingle concept can be discarded as the number of weaknesses significantly outweighs the number of strengths. Its use would result in a high number of unnecessary risks for the scale and nature of the mission. Due to the subcomponents required, namely the individual CMC tiles, the attachment system, and the substructure, an analysis of the entire system would be complex and time-consuming to analyze. A coupled thermomechanical analysis and sizing have to be performed not only for the holistic system but also at a component level to ensure that the system does not fail. The requirement of a standoff attachment system to the substructure, especially for the shingle system, where every tile requires secure attachment, also makes the shingle concept mass inefficient. The complexities of analysis, additional stresses due to material mismatch, and the added mass involved adds to its unsuitability for a small planetary entry mission. In addition, the standoff-based solutions are primarily used for the design and development of vehicles with a high degree of reusability [75], which is not required for the mission.

The insulated concept with a monolithic shell, as demonstrated on the Genesis capsule and the NALT project, does not require standoffs or mechanical attachments. This would reduce complexities, mass, and thermal mismatch issues, making it a superior solution to the shingle concept. The presence of a substructure, however, can significantly add mass despite additional assistance in load-bearing capabilities. As the Lockheed study showed [11], a monolithic hot structure heat shield with similar materials to the Genesis heat shield can withstand

demanding thermal and mechanical loads without a substructure. The monolithic insulative concept is therefore rejected in favor of the monolithic hot structure. The SPA, where an ablator replaces the insulation on the monolithic insulative concept, was also selected for the final tradeoff due to the promising thermal performance of the ablator.

3.2.3. Trade-off Analysis

The two remaining concepts are now traded off. As detailed thermal analyses, especially with ablation processes, are too intensive at this high-level stage, the comparison of concepts is based on literature and intuition. The criteria for selection are specified below, along with the rationale for the choice and ranking of concepts for each criterion, depicted in the graphical trade-off table 3.2.

- **Thermal performance:** Materials are a limiting factor to the performance of a TPS over a range of temperatures. The maximum service temperature, as well as the behavior of a TPS material at expected operating temperatures, are quick ways for initial qualitative judgment of TPS thermal performance.

  In the monolithic hot structure aeroshell, the CMC skin is directly exposed to the entry flow. CMCs are limited to a certain range of temperatures depending on the time exposed to peak temperatures beyond that of the material's working temperature. This temperature limitation can be raised through the application of coatings or the use of a UHTCMC. However, the MDM EDV is an expendable-use ballistic entry capsule; the allowable temperature can be raised beyond standard limits as entry and peak heating times are short and reusability is not a concern. In this case, the potential thermal performance of this concept can be considered sufficient.

  The SPA's external ablator, however, offers excellent thermal performance, which potentially allows a thinner CMC layer for mass reduction. The formation of pyrolysis gases during operation also lowers the incoming heat towards the vehicle. Finally, the MIRKA mission successfully proved the viability of the SPA concept, particularly for short entry trajectories with demanding heat loads. For these reasons, the SPA concept is considered to possess superior thermal performance compared to the monolithic hot structure.

- **Mass performance:** Weight is a crucial factor especially for small vehicles. In the comparison of TPS, areal density is typically used not only as a measure of weight, but as a measure of performance. When comparing multiple TPS concepts subject to identical conditions, the one requiring lower areal density shows superior thermal performance and efficiency.

  Considering the potential thermal performance of the SPA, the thickness of the CMC skin may be reduced as a result of the ablator. While it conserves mass, the reduced skin thickness might not guarantee the same mechanical performance as the skin of the monolilthic aeroshell. In addition, if both concepts employing the same CMC thickness are compared, the SPA is likely to show a higher areal density; ablators are denser than most lightweight fibrous insulation materials to be used on the monolithic hot structure [76] [39]. Finally, the SPA requires a substructure underneath the ablator, whereas the monolithic hot structure reduces this need. Therefore, the monolithic hot structure weighs less than the SPA.

- **Manufacturing Considerations:** Due to the simplicity and size of the vehicle, the manufacturing and integration process must not be excessively complex and time-consuming, which will affect design and production costs.

  In the case of C/(C-)SiC materials, Liquid Silicon Infiltration (LSI) is appropriate for manufacturing the heat shield's CMC skin, a closed axisymmetric shell. The manufacturing of the nose cap for the X-38 [77] and EXPERT [43] at DLR brought maturity and heritage to this method. Manufacturing the SPA heat shield, however, poses additional challenges as well as higher manufacturing times and cost due to the production and bonding of the ablative layer.

- **Implications for Future Mars Missions:** The Tumbleweed MDM is an opportunity to study and test systems within the Martian environment in a lightweight mission. It is therefore recommended that the TPS applied to the MDM EDV is not only suitable for the specific mission but applicable to a wider range of EDL systems considered for future missions.

  In both concepts, the external CMC skin will provide valuable data on its behavior and performance in the Mars entry environment. For a small mission like MDM, the SPA is highly suitable. However, scalability is an issue. It is not appropriate for large missions due to the limitations of ablator manufacturing [78] and the simultaneous attachment of the ablator to the substructure and the CMC to the ablator [76]. As entry progresses and the ablator recedes, the interface between the CMC skin and the ablator can be lost; this risk increases with vehicle size.

  While the SPA is restricted to small capsules and short entry times, the monolithic hot structure heat shield also applies to a broader range of vehicles and missions [79]. In addition to capsules as large as 10 m in diameter, this concept can be combined with other TPS methods in large vehicles. This includes the nose section for HIAD to expand its heat flux operability range, as well mid lift-to-drag vehicles with lifting body configurations, facing entry durations as long as 8 minutes [80]. Given its versatility and range of applicability, the hot structure aeroshell would provide a more valuable return of data compared to the SPA.

The cell colors in table 3.2 indicate the rating of a concept for each criterion. The colors are coded as follows: green (excellent), blue (good), yellow (correctable deficiencies). It is clear from the table that the monolithic hot structure concept is a favored solution concerning the MDM, keeping future missions in mind. It is therefore chosen for further design and analyses in the following chapters.

Concept	Thermal Performance	Mass Performance	Manufacturing Considerations	Implications for Future Mars Missions
Monolithic Hot Structure Forebody				
Surface-Protected Ablator				

Table 3.2: Graphical tradeoff of the final 2 TPS concepts.

4

Reference Load Definition

The design of a TPS cannot begin without knowing the design environment. The aerothermodynamic and mechanical environment from a given entry trajectory must be characterized to know the heating and structural loads on an entry vehicle, which are critical to appropriately design and size the TPS. A simple 2D trajectory model for the MDM entry vehicle was set up on MATLAB to obtain the thermomechanical loads; this chapter briefly explains the theory implemented in the model, the results of thermal and mechanical loads obtained, and the validation of the model. This begins with an explanation of the atmospheric data used for the Mars entry model in section 4.1. Section 4.2 explains the entry trajectory of the EDV. Next, the deceleration loads to characterize the EDV's structural environment are discussed in section 4.3. This is followed by the aerothermodynamic models considered and their selection for the MDM in section 4.4. Finally, the effect of vehicle parameters on thermostructural loads is discussed in section 4.5.

4.1. Atmospheric Data

Planetary entry is dependent on the planet's atmospheric properties, such as its composition, gravitational acceleration, pressure, and temperature over different altitudes. A reliable Martian atmospheric model must be used as a reference for this project. The Mars Climate Database [81] was therefore used as it is an extensive atmospheric model validated using data from orbiters and surface missions, such as the Mars Reconnaissance Orbiter and Mars 2020. The current version 6.1 was released in October 2022.

As the exact MDM entry date is unknown, the input Earth date is January 1, 2030, at 12:00:00 UTC. The temperature, pressure, and atmospheric density used in the model were extracted by averaging these properties over a latitude and longitude of -180° to $+180^\circ$ and -90° to $+90^\circ$ respectively. This way, a global average of the outputs is obtained without constraining the data to a particular location. The averaged atmospheric pressure and temperature over altitude are plotted in figure 4.1.

4.2. Entry Trajectory

For the MDM trajectory simulation, the following assumptions were made for simplicity:

- The analysis is constrained to planar motion (two-dimensional)
- Entry is fully ballistic (no lift and zero angle-of-attack)
- The drag coefficient is constant throughout the flight

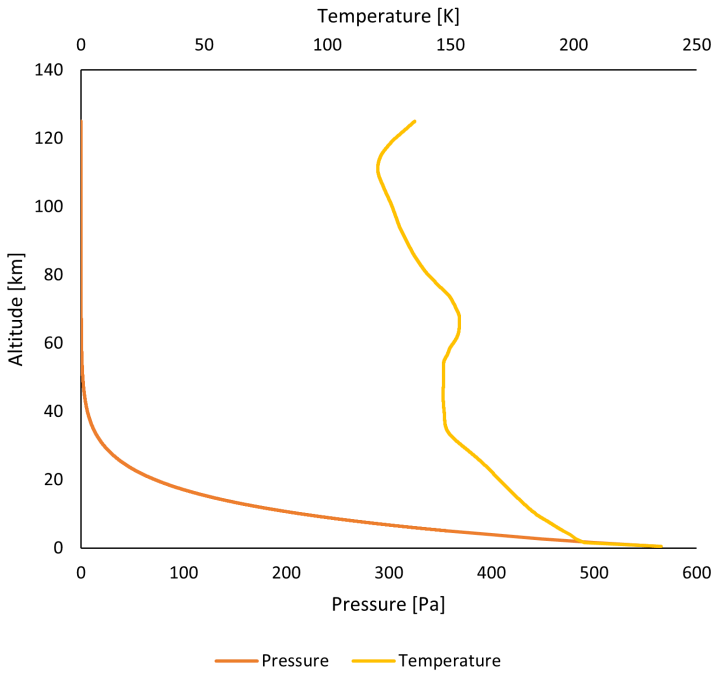

Figure 4.1: Mean global pressure and temperature as a function of altitude using MCD v6.1.

- Only the stagnation point is considered - it is assumed that the heat flux and pressure loads are constant throughout the length of the vehicle.
- The planetary body is perfectly spherical and non-rotating.

The MDM initial entry conditions mentioned in section 1.1 are repeated here in table 4.1 for convenience.

Entry Velocity (km/s)	Entry Angle (°)	Entry Altitude (km)
7.246	-11.916	125

Table 4.1: Entry conditions for the Tumbleweed MDM.

The gravitational acceleration at any point along the flight is given by equation 4.1:

$$g = g_0 \frac{R_m^2}{(R_m + h)^2} \tag{4.1}$$

g_0 is the standard gravitational acceleration of Mars (3.72076 m/s^2), R_m is the equatorial radius of Mars and h is the EDV's altitude.

Adopting the reference frame in figure 4.2, Newton's second law is applied, resulting in the equations of motion given in equation 4.2 and 4.3.

$$m\frac{dV}{dt} = -D - mg\sin\gamma \tag{4.2}$$

$$m\frac{d\gamma}{dt} = L - mg\cos\gamma(1 - \frac{V^2}{V_c^2}) \tag{4.3}$$

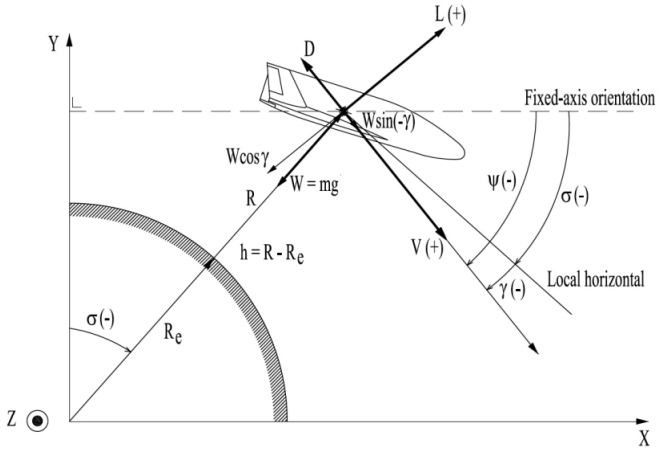

Figure 4.2: Reference frame from [82] adopted for the trajectory model. R_e is replaced by R_m in this work.

The flight path angle γ orients the velocity vector V with respect to the local horizontal frame. V_c is the vehicle's circular velocity at the entry interface altitude, given by $\sqrt{g(h+R_m)}$. The kinematic equation is described by the vertical component of velocity in equation 4.4.

$$\frac{dR_m}{dt} = \frac{dh}{dt} = V \sin\gamma \tag{4.4}$$

Equations 4.2, 4.3, and 4.4 are integrated numerically using the Runge-Kutta method on MATLAB.

4.3. Deceleration

The EDV's deceleration profile characterizes its structural loads. To proceed, the ballistic parameter β is now introduced:

$$\beta = \frac{m}{C_D S} \tag{4.5}$$

S is the reference surface area of the vehicle. The Newtonian approach can be used to calculate a simplified drag coefficient C_D for the EDV's geometry, approximating it as a cone [83]. This allows for a simple expression for C_D as a function of the conical vertex angle θ_c:

$$C_D = \frac{1}{2}\cos^2\theta_c(1-\sin^4\theta_c) + 2\sin^2\theta_c(1-\frac{1}{2}\cos^4\theta_c) \tag{4.6}$$

A drag coefficient of 1.77 for $\theta_c = 70°$ is obtained.

The ballistic coefficient β is a crucial parameter in dictating the aerodynamics and entry environment of a vehicle. It is a measure of a vehicle's ability to maintain its velocity in the presence of an atmosphere. It is desired to attain lower ballistic coefficients for Mars EDL to achieve lower levels of heating, and maximum deceleration at higher altitudes. Equation 4.7 is obtained by substituting β into equation 4.2 and expanding the drag term.

$$\frac{dV}{dt} = \frac{-\rho V^2}{2}\frac{1}{\beta} - g\sin\gamma \tag{4.7}$$

The deceleration profiles against altitude of previous Mars entry missions are plotted in the figure 4.3a for comparison with historical data. The data from table 2.1 was used as input for

Vehicle	Entry Velocity [km/s]	Entry Angle [°]	Peak Deceleration [G]	Actual Peak Deceleration [G]	Error [%]	Peak Deceleration Altitude [km]
MDM, 70°	7.25	-11.92	12.01	-	-	36.18
MDM, 45°	7.25	-11.92	11.89	-	-	35.63
Pathfinder	7.48	-14.06	17.89	16.00	11.86	28.39
Deep Space 2	6.90	-13.25	14.92	12.40	20.28	32.90
MER	5.39	-10.74	6.18	4.78	29.39	28.63

Table 4.2: Comparison of maximum deceleration obtained from the flight model and actual data.

these missions. The deceleration profiles for two MDM EDVs are plotted in figure 4.3b. The 45° vehicle refers to EDV 2 with a ballistic coefficient of 38.6 kg/m^2 in table 4.8. The same 2030 atmospheric model was used for all missions; using the Pathfinder case, it was found that inserting the corresponding averaged atmospheric conditions at its time of entry gives no difference in results.

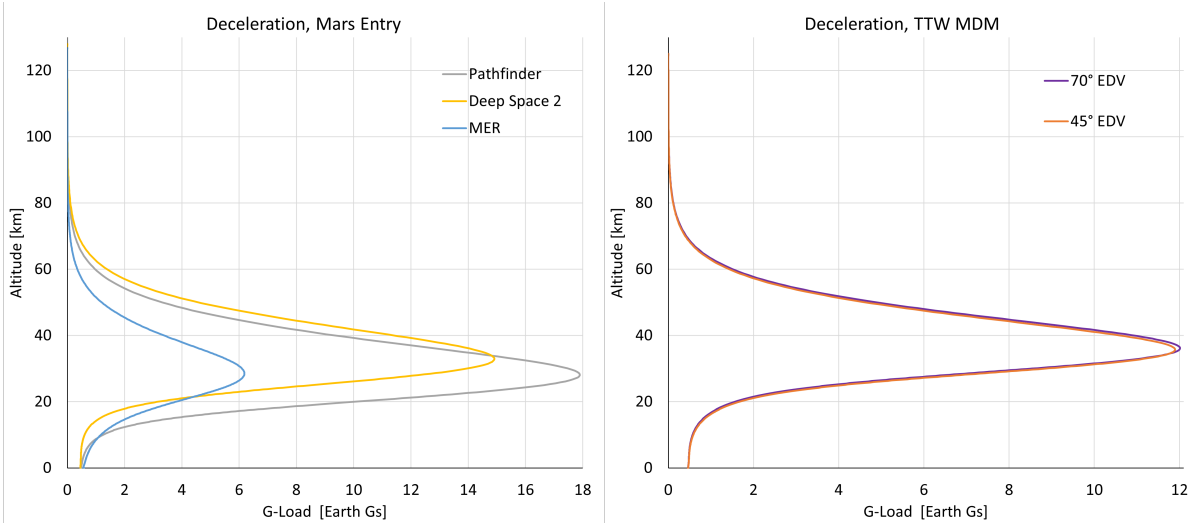

(a) Altitude-Deceleration plots for three historical Mars missions.

(b) Altitude-Deceleration plots for the MDM with the initial 70° aeroshell and the selected 45° aeroshell.

Figure 4.3: Altitude-Deceleration plots of Mars missions given by the trajectory model.

To assess the accuracy of the model, the maximum deceleration obtained is compared with recorded flight data in table 4.2. The model overestimates the deceleration compared to actual flight data, up to an error of approximately 30% for MER. This difference may be due to the assumption of a constant drag coefficient as well as transverse forces that are not considered in planar motion. In reality, the drag coefficient changes throughout the trajectory, especially between different flow regimes. As the deceleration loads from the model are all conservative in comparison to the actual deceleration, they are appropriate to use for mechanical design loads.

4.4. Aerodynamic Heating

The entry conditions of a vehicle and its ballistic coefficient strongly dictate the levels of aerodynamic heating experienced. The aerothermodynamic analysis in this work takes the convective heating at the stagnation point, where the most severe heat fluxes occur. The location

of the stagnation point may vary according to the vehicle's angle of attack and flow properties; as the angle of attack is zero, the stagnation point is assumed to be located only at the tip of the EDV's nose. For further simplicity, radiative heating from the gas layer is neglected in this work. This is a valid assumption that is typically used in assessing Mars entry for current vehicle sizes, especially if they are not large [84]. Pathfinder, due to its relatively high entry velocity, experienced radiative heating between 5 to 10 W/cm^2, which is still small in comparison to convective heating. In addition, a TPS wall with low surface catalycity will show lower rates of radiative heating. However, a combination of large entry masses and a high entry velocity in future missions will cause radiative heating to play significant effects.

Multiple solutions exist to calculate the convective heating rate at the stagnation point of a blunt-nosed vehicle; the Chapman and Sutton-Graves relations will be discussed and compared in this section to select the appropriate heat fluxes for design. These models in particular were considered as they are quick approximations with sufficient detail for stagnation point heating in conceptual studies [85].

Chapman Model

The Chapman model [86] in equation 4.8 relates the stagnation point heating to the vehicle's nose radius R_n, entry conditions, and atmospheric composition.

$$q_c = c_1 R_n^{-n} (\frac{\rho}{\rho_0})^{(1-n)} (\frac{V}{V_c})^m \tag{4.8}$$

The constants c_1, n, and m are dependent on planetary atmospheric composition and flow conditions. The flow is assumed to be laminar. Taking the values from literature [87], m and n are 3.04 and 0.5 respectively, and a c_1 value of 932194 kg$^{0.5}$m$^{2.03}$s$^{2.04}$ is used. The sea-level density ρ_0 of Mars is taken as 0.01712 kg/m^3. The Chapman heat flux is calculated using the trajectory model and plotted for past Mars entry missions in figure 4.4.

The results of the maximum convective heat flux calculated using the Chapman equation of the vehicles plotted in figure 4.4 are shown and compared with their actual values in table 4.3.

Vehicle	Entry Velocity [km/s]	Nose Radius [m]	Peak Chapman Heating [W/cm^2]	Actual Peak Heating [W/cm^2]	Error [%]
Pathfinder	7.48	0.66	95.62	100.69	-5.04
Deep Space 2	6.90	0.09	156.79	194.00	-19.18
MER	5.39	0.66	35.41	37.72	-6.13

Table 4.3: Comparison of Chapman and actual peak heating for historical Mars missions.

The Chapman values according to the trajectory model are relatively accurate, with underpredictions of less than 10%, except for Deep Space 2, with an error of approximately 19%.

Sutton-Graves Model

The Sutton-Graves model [88] in equation 4.9 neglects the hot-wall correction term employed by Chapman and instead assumes a fully-catalytic cold-wall. This gives a conservative estimate of the stagnation point heating. Like the Chapman model, it is also adaptable to various planetary atmospheres. The constant c_1 for the Martian atmosphere is taken as 1.83×10^{-4}

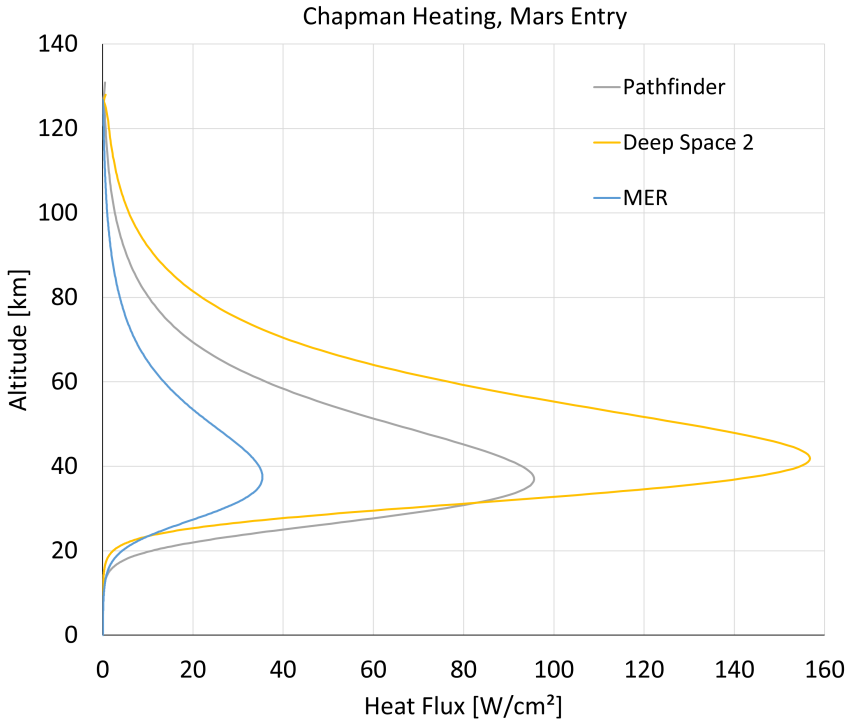

Figure 4.4: Altitude-Heat flux plots of three historical Mars entry missions using the Chapman relation

from literature [89]. The Sutton-Graves heat flux is calculated using the trajectory model and plotted for past Mars entry missions in figure 4.5.

$$q_c = c_1 R_n^{-n} \rho^{(1-n)} V_\infty^m \tag{4.9}$$

The peak heating according to the Sutton-Graves model for each vehicle plotted in figure 4.5 is given in table 4.4 and compared with the actual value.

Vehicle	Entry Velocity [km/s]	Nose Radius [m]	Peak Sutton-Graves Heating [W/cm^2]	Actual Peak Heating [W/cm^2]	Error [%]
Pathfinder	7.48	0.66	161.59	100.69	60.48
Deep Space 2	6.90	0.09	264.64	194.00	36.41
MER	5.39	0.66	59.73	37.72	58.36

Table 4.4: Comparison of Sutton-Graves and actual peak heating for historical Mars missions.

As expected, the Sutton-Graves heat flux is highly conservative, with overestimations of approximately 60% for Pathfinder and MER. A comparison between Sutton-Graves and Chapman heating predictions and the stagnation point for the MDM EDVs is shown in figure 4.6 and table 4.5. It can be seen that the Sutton-Graves heating envelope is significantly higher than the Chapman heating envelope, with peak values differing by 84 and 75 W/cm^2 for the 70° and 45° configuration respectively.

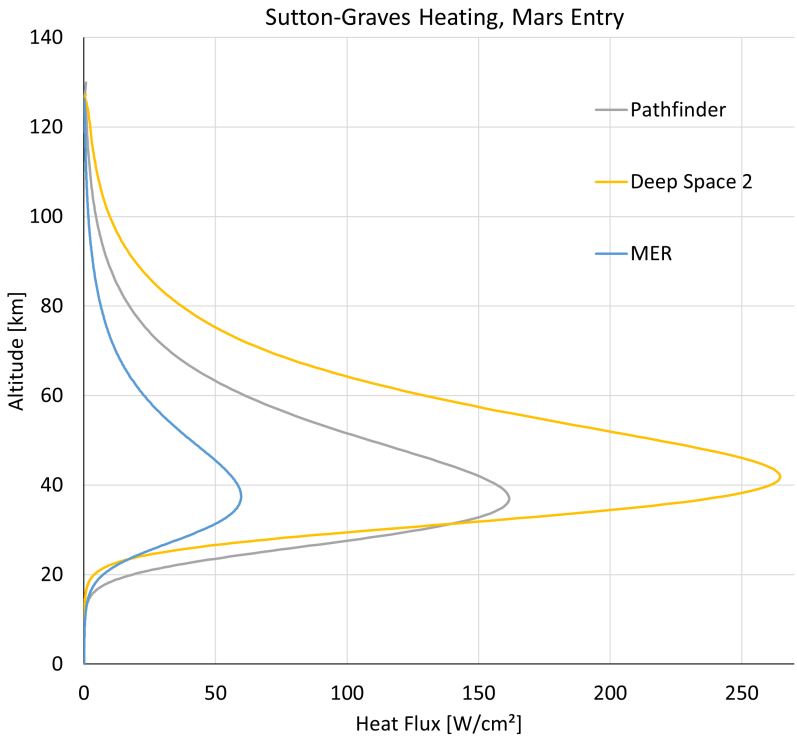

Figure 4.5: Altitude-Heat flux plots of three historical Mars missions using the Sutton-Graves relation.

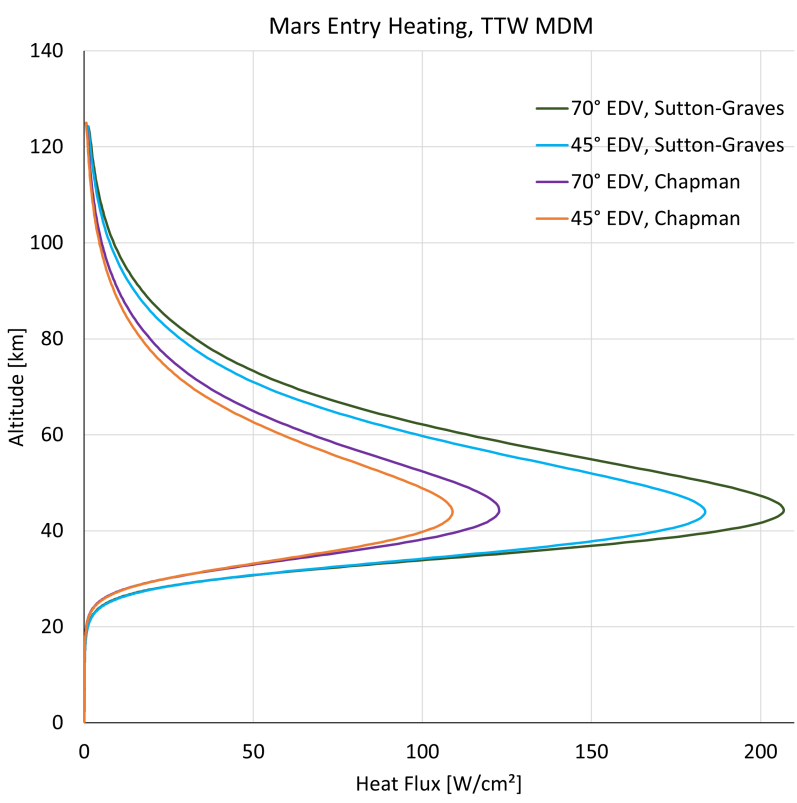

Figure 4.6: Comparison of Altitude-Heat flux plots of the MDM EDVs using the Sutton-Graves and Chapman relations.

Vehicle	Entry Velocity [km/s]	Nose Radius [m]	Peak Chapman Heating [W/cm^2]	Peak Sutton-Graves Heating [W/cm^2]
MDM, 70°	7.25	0.15	122.71	206.86
MDM, 45°	7.25	0.20	108.93	183.62

Table 4.5: Comparison of Sutton-Graves and actual peak heating for historical Mars missions.

Despite slightly underpredicted values, the Chapman model provides a more accurate and representative value of stagnation heat flux compared to the Sutton-Graves model. Therefore, the Chapman model is selected for the heat flux history used in the proceeding sections.

4.5. Effect of EDV Parameters on Thermostructural Loads

As of the latest TTW update at the time of writing, better aerodynamic stability throughout entry is desired. To increase mass efficiency, a heat shield vertex angle of 45° was recently proposed to passively orient the EDV. As propulsive and active control devices are eliminated, more mass can be allocated to the payload and other EDV subsystems, including aeroshell mass. This method is commonly adopted for small entry vehicles such as Deep Space 2 [90]. This change in vertex angle, however, results in a lower drag coefficient, which in turn affects the vehicle's ballistic coefficient. The entry environment encountered by the vehicle can be profoundly affected. A sensitivity analysis, therefore, is conducted in this section to find a combination of relevant design parameters that satisfies requirements and minimizes thermostructural loads. These main parameters are driven by the ballistic coefficient, namely entry mass, vertex angle (drag coefficient), and vehicle base diameter. The nose radius also strongly dictates the incoming heat fluxes but is constrained to scale up with base diameter using the relations in appendix A. Adjusting the base diameter will therefore also adjust the vehicle's nose radius. The selected combination of parameters will be used for further TPS design and comparison in chapter 7. The current ballistic coefficient value is 36.4 kg/m^2, similar to that of Deep Space 2 [91].

First, the vehicle's drag coefficient, through the vertex angle via equation 4.6, will be changed. The mass and base diameters of the EDV will be kept constant.

Entry mass [kg]	Diameter [m]	Vertex Angle [°]	C_D	Ballistic Coefficient [kg/m^2]	Peak deceleration [G]	Peak Deceleration Altitude [km]	Peak heating [W/cm^2]	Peak Heating Altitude [km]
18.18	0.60	45	1.03	62.35	10.91	32.46	153.83	40.43
18.18	0.60	60	1.52	42.43	11.70	35.02	130.88	43.25
18.18	0.60	70	1.77	36.40	12.01	36.18	122.71	44.35

Table 4.6: Effect of vertex angle on thermostructural loads.

From table 4.6, it can be observed that a small change in drag coefficient greatly affects the ballistic coefficient. Reducing the vertex angle from 70° to 45° can result in an increase in maximum heat flux by approximately 33 W/cm^2. The altitudes of maximum heat flux and maximum deceleration both decrease by approximately 4 km, while the peak deceleration reduces by approximately 1 G. Therefore, a constraint must be placed on the ballistic coefficient, a constraint; a maximum of 40 kg/m^2 is set.

Next, the drag coefficients and base diameters of the EDV will be kept constant as per the values in table 4.2; the total EDV mass will be changed. The current EDV mass is 18.18 kg. A constraint is placed such that the total mass shall not exceed 20 kg.

Entry mass [kg]	Diameter [m]	Vertex Angle [°]	C_D	Ballistic Coefficient [kg/m^2]	Peak deceleration [G]	Peak Deceleration Altitude [km]	Peak heating [W/cm^2]	Peak Heating Altitude [km]
16.00	0.60	70	1.77	32.04	12.27	37.09	116.17	45.12
18.18	0.60	70	1.77	36.40	12.01	36.18	122.71	44.35
20.00	0.60	70	1.77	40.04	11.82	35.56	127.74	43.62

Table 4.7: Effect of vehicle mass on thermostructural loads.

From table 4.7, it can be observed that an increase in mass by approximately 2 kg leads to an increase in convective heat flux; its corresponding altitude shows a small decrease of approximately 0.7 km. The peak deceleration altitude shows a decrease of 0.9 km between 16 and 18.18 kg, while the difference is smaller between 18.18 and 20 kg at 0.6 km. The peak deceleration, however, shows no significant decrease between 16 and 20 kg. The heat flux is the most affected by a change in entry mass. Increasing the vehicle's base diameter, and consequently, nose radius, can compensate for the increase in heat flux.

Finally, a combination of mass and appropriate diameters for a 45° vertex angle ($C_D = 1.03$) is investigated. Two aeroshells with a 45° vertex angle are compared. EDV 1 will keep the same mass as the original EDV; its diameter is adjusted such that its ballistic coefficient is also kept the same. EDV 2 has a different ballistic coefficient. Its entry mass is increased to the 20 kg limit and its diameter is sized up to 0.8 m. A computer-aided design (CAD) model of the three heat shields is shown in figure 4.7. Details of calculating the dimensions, including the surface area of the heat shield, are given in appendix A adopting the relations used by Prabhu et al [92].

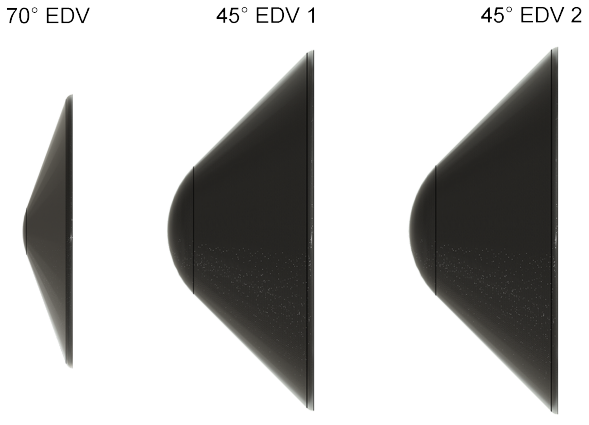

Figure 4.7: CAD models of 3 different heat shield configurations to scale.

Despite different dimensions, retaining the same ballistic coefficient keeps the peak deceleration and the altitudes of peak deceleration and heating the same. The maximum heat fluxes

of the 45° EDVs, however, are lower than that of the 70° EDV, whereas it is much larger for the 45° vehicle in table 4.6. This is a result of the increased nose radius, which is inversely proportional to the heat fluxes as shown in equation 4.8. As the difference in nose and base radii between the two 45° heat shields are small, their heating profiles are very similar in figure 4.9a. Past the peak heating phase, all three vehicles appear to follow nearly identical profiles.

For the increase in mass between the 45° EDVs, the peak deceleration remains similar as demonstrated in table 4.7. The altitude-heat flux and altitude-deceleration curves for the three vehicles are plotted in figures 4.9a and 4.9b respectively. The deceleration plots, however, are identical for the 70° EDV and the 45° EDV with the same ballistic coefficient. For this reason, the deceleration plot for the 70° EDV is not visible, and the plot 45° EDV 1 is layered over it. The plot for the vehicle with the higher ballistic coefficient also follows a very similar profile, with the peak deceleration having a small difference from the rest at a small difference in altitude.

Vehicle	Diameter [m]	Nose radius [m]	Entry Mass [kg]	Ballistic Coefficient [kg/m^2]	Peak Deceleration [G]	Peak Deceleration Altitude [km]	Peak heating [W/cm^2]	Peak Heating Altitude [km]
70° EDV	0.600	0.150	18.181	36.402	12.015	36.175	122.714	44.349
45° EDV 1	0.785	0.196	18.181	36.402	12.015	36.175	107.267	44.349
45° EDV 2	0.800	0.200	20.000	38.583	11.895	35.630	108.928	43.973

Table 4.8: EDV parameter combinations and maximum thermostructural loads.

As the maximum loads and their corresponding altitudes for both 45° EDVs are similar, EDV 2 is selected for the final 45° EDV configuration. This is because the larger diameter allows more payload space, and the 20-kg mass allows a larger TPS areal density limit. Figure 4.8 shows the newly selected dimensions of the heat shield on the aeroshell illustration.

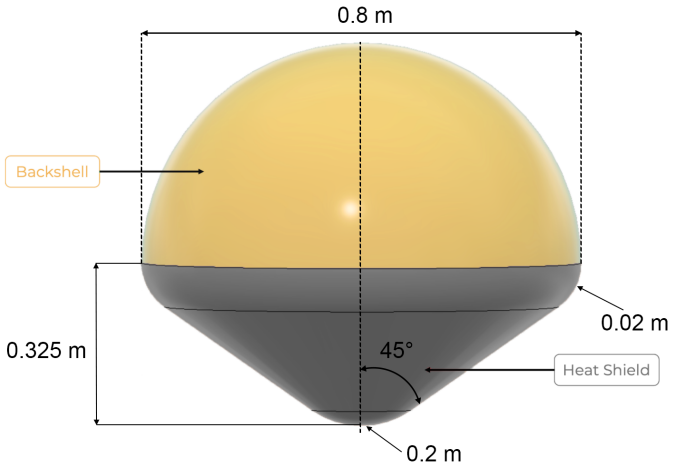

Figure 4.8: MDM EDV aeroshell with modified heat shield dimensions.

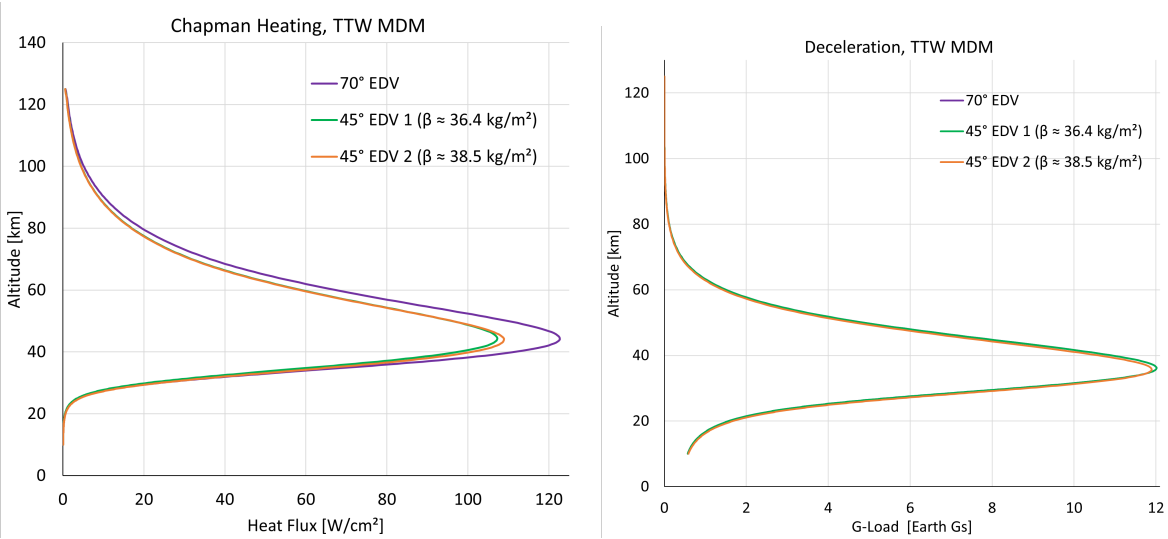

(a) Altitude-Heat flux plots of three MDM EDVs.

(b) Altitude-Deceleration plots of three MDM EDVs.

Figure 4.9: Thermostructural profiles of three MDM EDVs.

5

Requirements and Considerations

With the design concept and load environment defined, preliminary considerations can be made for the design of the heat shield. This begins with a mass budget estimation for the entry and descent vehicle to derive the required heat shield mass in section 5.1. This is followed by a derivation of requirements in section 5.2. A brief description and schematic of the selected design concept from chapter 3 is presented in section 5.3. The design considerations that follow will be used to set up the finite element (FE) model in chapter 6. Section 5.4 presents the heat transfer mechanisms, as well as corresponding assumptions, to be incorporated into the thermal model. The most critical (thermo)mechanical load cases and failure modes to consider are discussed in section 5.5. Finally, section 5.7 details the consideration concerning materials.

5.1. EDV Mass Budget Estimation

Besides the MDM EDV's vehicle configuration and heat shield geometry, no physical details about the EDV were previously defined or analyzed by Team Tumbleweed. A mass budget estimation for the EDV was therefore performed in this work to obtain the mass of the heat shield.

Based on historical data from American planetary entry missions, a linear relationship has been developed by NASA to estimate an entry vehicle's TPS mass fraction as a function of total integrated heat load [93]. However, this relationship only applies to purely ablative systems and considers only the thermal function of the TPS without including the heat shield's structural mass. In addition, small entry missions such as the Tumbleweed MDM may not require as many subsystems and components as conventional EDVs. No parachutes, active control, or propulsion systems will be included on the MDM, for example. Therefore, even if an ablative system is used, using this historical relationship would provide excessively conservative mass constraints. In this thesis, a TPS with an external structural skin is explored, therefore the heat shield's mass budget concerns both structural and thermal aspects.

To estimate the mass of the TPS, the mass of the aeroshell must be determined. The MarsDrop capsule, which weighs less than 4 kg and measures 0.3 m in diameter, was developed by Staehle et al [94] and was successfully demonstrated in an Earth drop test. Unlike the Deep Space 2 capsule, it consisted of a separable aeroshell, which is also the case for MDM. Therefore, the mass allocations excluding payload and the aeroshell structure are based on MarsDrop. The mass breakdown for a total MDM EDV mass of 20 kg is given below, and summarized in table 5.1:

- **Payload:** The payload comprises the Tumbleweed rover, which has a known mass of 8 kg [14].

- **Non-structural mass:** This comprises components and subsystems within the EDV.
  - **Mechanisms.** This includes the mechanisms to separate the heat shield and backshell. The MDM EDV, due to its larger size than MarsDrop, may require more components to separate the aeroshell. A conservative mass of 500 g compared to 256 g on MarsDrop is therefore assumed.
  - **Power.** Taking a mass of 360 g from the MarsDrop electric power subsystem excluding solar panels, 400 g is estimated for the MDM EDV. This includes lithium-ion batteries and a battery board, which were also used to power Deep Space 2 [91].
  - **Attitude Determination and Navigation.** The MDM EDV will have no control systems for entry and descent and will rely on its aerodynamics for stability and orientation. However, it would be useful to collect EDV performance and trajectory data. For this subsystem, an internal measurement unit is to be installed, consisting of a descent camera, gyroscopes, and accelerometers. This constituted 90 g of mass on MarsDrop; 100 g is estimated for MDM.
  - **Avionics.** MarsDrop used a lightweight flight computer and data storage system measuring 10 g. Its telecommunications system consists of an ultra-high frequency radio and antenna measuring approximately 60 g. For avionics and telecommunications, a total of 100 g for the MDM EDV is estimated.
  - **Internal Heating.** Heaters will be installed in the EDV to keep the payload at optimal temperatures during the cruise to Mars. The internal heating subsystem on MarsDrop weighs 160 g; 200 g is estimated for MDM.
  - **EDV instrumentation.** To assess the performance of the EDV and the heat shield, a lightweight, miniature suite of entry, descent, and landing instrumentation is necessary. It would record atmospheric, aero(thermo)dynamic, and flight data. This suite would include multiple thermocouples and pressure sensors and different points of the EDV. A mass of 200 g is estimated.

  In total, a mass of 1.5 kg is estimated for non-structural components. To place a margin, an upper limit of 2 kg is taken.

- **Aeroshell:** Subtracting the payload and upper limit non-structural mass from the total entry mass, 2 kg is obtained. Subtracting this value and the rover from the total EDV mass, a structural mass of 10 kg for the aeroshell remains. It is assumed that the heat shield takes 80% of this mass. This assumption was estimated from literature; the heat shield mass ratios for the aeroshell structure, including TPS, are 0.77 and 0.82 for ExoMars and Mars 2020 respectively [18]. Therefore, the aeroshell structural mass of a 20 kg EDV consists of an 8 kg heat shield and a 2 kg backshell. If the calculations are applied to the initial 18.2 kg EDV, a heat shield mass of 6.5 kg is obtained.

Subsystem	Mass [kg]
Payload Mass: 8 kg	
Mechanisms	0.5
Electrical Power Systems	0.4
Attitude Determination and Navigation	0.1
Telecommunications, Command, and Data Handling	0.1
Internal Heating	0.2
EDV Instruments	0.2
EDV Non-Structural Mass/Upper limit: 1.5/2 kg	
Backshell Structure and TPS	2
Heat Shield Structure and TPS	8
Total Aeroshell Mass : 10 kg	
TOTAL EDV MASS : 20 kg	

Table 5.1: Estimated mass breakdown of EDV subsystems.

5.2. Requirements Analysis

Requirements will now be generated for the design of the heat shield; relevant constraints from the overall vehicle will also be mentioned. Codes are designated to each requirement and constraint such as TPS-TH-# or EDV-CO-#. The requirement identifier abbreviations are elaborated on in table 5.2.

Requirement Identifier Abbreviation	Designation
TPS	Thermal Protection System
TH	Thermal Performance
ME	Mechanical Performance
EDV	Entry and Descent Vehicle
CO	Constraints

Table 5.2: Definition of requirement identifier abbreviations.

The requirements are generated for performance with respect to both functions, attributes, and constraints. Table 5.3 shows the requirements of the system and their rationale.

ID	Requirement	Rationale
TPS-TH-1	The system shall protect the spacecraft during its operational phase at entry and descent for one flight.	The EDV is expendable and will be discarded after use.
TPS-TH-2	The system shall keep the average inner mold line temperature below 450 K.	The inner mold line temperature, or backface temperature, depends on the primary structural material of the rover. While this remains an open decision, recent private communication with a member of TTW's structures team revealed that Kevlar is a leading candidate. This consideration was made due to its resistance to corrosion and abrasion at a range of temperatures appropriate for the Martian surface environment. Kevlar has a maximum service temperature of 450 K [95].
TPS-TH-3	The system shall be able to withstand entry heat fluxes of up to 109 W/cm^2 for a heat shield with a half-cone vertex angle of 45°.	This value was based on the aerothermal analysis in chapter 4.
TPS-ME-1	The system shall be able to withstand maximum pressure loads corresponding to 12 Gs throughout its operation.	Deceleration due to aerodynamic pressure is the main source of mechanical loads imposed on the vehicle. No damage must be caused by combined atmospheric and aerodynamic pressure at the point of maximum deceleration. The deceleration load obtained from the trajectory model in chapter 4 is 12 G.
TPS-ME-2	The combined stresses imposed by heating and mechanical loads during flight shall not exceed the limit stresses of the heat shield's skin material.	CMC materials, demonstrating orthotropic or quasi-isotropic properties, are characterized by multiple stress limits for tension, compression, and bending. Stress responses to entry loads exceeding any of their respective values will lead to catastrophic failure.
TPS-ME-3	The mass of the heat shield shall not exceed 80% of the EDV's structural mass. The maximum heat shield mass for the 45° aeroshell is 8 kg.	These values were based on the mass budget estimation performed in section 5.1.
EDV-CO-1	The total entry mass shall not exceed 20 kg.	The entry mass of the previously analyzed EDV was 18.2 kg. 20 kg is the upper margin.
EDV-CO-2	The heat shield shall not change the configuration of the entire spacecraft.	The EDV's configuration is set as a typical Mars entry capsule.

Table 5.3: Heat Shield System requirements

5.3. Design Description

The selected hot structure aeroshell concept consists of two primary functional layers, illustrated in figure 5.1:

- **CMC Structural skin:** This thin-walled structure is the primary component of the hot structure TPS. It carries mechanical loads while enduring the incoming heat flux. Displaying a high surface emissivity, it also serves to re-radiate a portion of the incoming heat back to the external environment.
- **Thermal insulation:** Lightweight with poor conduction, this layer serves to delay the heat flux conducted to the IML throughout the entire duration of entry and descent until heat shield jettison. This layer is not expected to carry any mechanical loads. Fibrous insulation is typically used. Depending on the temperatures encountered, one or more materials may be used throughout the thickness profile to minimize mass. This means that a denser high-temperature insulation material will be used under the CMC skin, and a medium-to-low-temperature insulation material will be used below it.

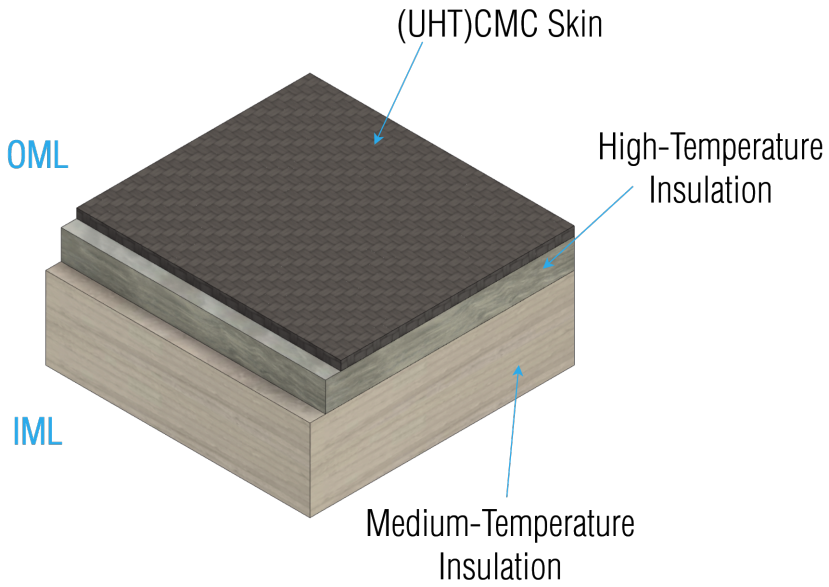

Figure 5.1: Through-thickness schematic of the hot structure aeroshell design concept.

5.4. Heat Transfer Modes

As covered in chapter 4, the heat transfer from the external environment to the surface of the TPS considered in this work is only convection. Within the TPS, radiation and conduction are the modes of heat transfer.

Heat is transferred from the top surface of the TPS to the external environment, and from the TPS backface to inside the EDV via radiation. The transmitting surface loses heat to an absorbing medium or body, which heats up. The reradiated heat depends on the emissivity of the surface; this is described in equation 5.1 per unit area.

$$q_{rad} = \epsilon\sigma(T_w^4 - T_\infty^4) \tag{5.1}$$

ϵ is the emissivity of the transmitting surface, T_w is the wall or surface temperature, T_∞ is the freestream or environmental temperature, and σ is the Stefan-Boltzmann constant, which is

equal to 5.67$\times 10^{-8}$W/m^2·K^4. The same equation can also be used to calculate the maximum equilibrium wall temperature. This temperature gives the highest temperature achievable by a TPS surface as it is based on the assumption that all the heat is radiated back to the ambient environment. The equilibrium wall temperature is sometimes used as a first estimate of the maximum flight temperature encountered by a TPS [96]. This value is conservative but also can be used to check the thermal model to ensure that the highest temperature at the wall does not cross the radiative equilibrium temperature. This temperature can also be used for material selection of the structural skin.

Fourier's law in equation 5.2 describes the conductive heat transfer per unit area through the thickness or length of a body. k is the thermal conductivity of the material, L is the thickness of the body, and T_1 and T_2 are the temperatures at two points of interest within the body.

$$q_{cond} = \frac{k}{L}(T_1 - T_2) \tag{5.2}$$

For a steady-state thermal analysis, the heat balance can be described in equation 5.3 using the law of conservation:

$$q_{in} = q_{cond} + q_{rad} \tag{5.3}$$

A steady-state thermal analysis, however, is not appropriate for TPS design and analysis as it assumes that the incoming heat does not change with respect to time, leading to highly conservative estimates of temperatures. In the case of planetary entry, a transient thermal analysis must be used as the heat fluxes vary rapidly throughout the entry duration. A comparison between the use of a steady-state and transient thermal model for a rough and initial estimate of temperatures in early design phases will also be briefly discussed in chapter 6.

A transient thermal analysis introduces an additional time-dependent term in the description of heat balance; heat is stored within a body over time in addition to being transferred away. This storage of heat per unit area is described in equation 5.4, where Cp is the specific heat capacity of the material, ρ its density, and the differential term is the rate of change in temperature.

$$q_{stored} = \rho L C p \frac{dT}{dt} \tag{5.4}$$

With the thermal storage term introduced, the transient thermal balance of the TPS per unit area can then be stated in equation 5.5:

$$q_{in} = q_{cond} + q_{rad} + q_{stored} \tag{5.5}$$

To simplify the thermal analysis throughout this work, the following assumptions were used:

- Radiation only takes place at the top surface and back surfaces of the entire TPS. No radiative processes take place within the system.
- Surface emissivities are constant.
- There is no conduction due to gas in the fibrous insulation layer.
- There is no contact conductance between layers of different materials. This assumption gives a more conductive estimate of temperatures.

- Convective heat flux and freestream temperature are the only external factors within the heat transfer analysis. Other factors such as aerodynamic and atmospheric pressure have no influence.
- The ambient temperature inside the EDV is constant.
- The incoming heat flux, taken from the trajectory model in the previous chapter, is not affected by the temperatures at or outgoing heat from the TPS surface.
- Oxidation and ablation processes are not included in the thermal model.

5.5. Structural Loads and Failure Modes

Aerodynamic pressure is the primary contributor to the vehicle's structural loads, as shown in equation 4.7. The aerodynamic pressure alone is often taken as the input for the mechanical load environment in TPS or entry vehicle design [97] [98]. The sum of the aerodynamic and atmospheric pressures, however, provides a more conservative estimate [99]. Throughout this work, the EDV is assumed to have no internal pressure, providing a further conservative mechanical environment. As per the zero angle of attack and uniform load distribution assumptions in section 4.2, an axisymmetric pressure distribution is obtained. This assumption is typically used for structural analyses in the preliminary design of an axisymmetric heat shield [97] [100].

In the design of hot structures, it is important to note that mechanical loads alone do not provide a complete picture of structural analysis. The structure also responds to a change in temperature, such as a rise in temperature or the presence of temperature gradients within the structure. Stresses are produced as a result of thermal expansion. The thermal stress response exhibited by a structure is dependent on its material's coefficient of thermal expansion (CTE) α, as shown in equation 5.6. As E is the material's modulus of elasticity, the product of α and temperature change ΔT is therefore equal to the thermal strain.

$$\sigma_{thermal} = E\alpha\Delta T \tag{5.6}$$

Static (thermo)structural analyses will be performed; only the outer skin will be investigated and the insulation layer will be neglected. This practice is done in literature for thermomechanical TPS analysis as fibrous insulation materials are soft and have no load-carrying abilities [101]. The structural failure modes considered are:

- Buckling, where a structure loses its stability under compressive loads. Due to the compressive action of aerodynamic pressure, buckling is commonly considered as a critical failure mode in entry vehicle and TPS structural design [99] [100]. The heat shield substructure of the Viking entry capsule was primarily designed against buckling due to external pressure [97]. A structure exhibits sudden deformation at its critical buckling load. As a heat shield is a single point of failure component, it is therefore desired that the buckling load is sufficiently beyond the maximum flight loads.

- Failure by yielding or exceeding the maximum allowable stress. A structure becomes permanently damaged once the stress response to an applied load exceeds its material's yield or maximum strength. In the case of CMCs, the maximum allowable stresses are characterized by tension, compression, and flexural strength [37]. As maximum allowable stress is a material property and is more easily predicted than buckling, it is desired that the loads corresponding to maximum stress are lower within the design envelope than structural buckling loads. The combined action of thermal and mechanical

stresses due to expected design loads must not amount to any of the strength limits of the material.

The failure criterion used in this work will be based on maximum stresses. The stress results in principal directions will be compared to the maximum tensile and compressive strengths of the skin material, and the bending stresses to the maximum flexural strength. The maximum stress criterion is a practice recommended by the ECSS standards for structural materials [39] when evaluating CMC hot structures, with the DLR standard material in mind.

5.6. Safety Design Philosophy

In the design of spacecraft structures, it is important to design for the worst-case scenario. This is typically done by applying a safety factor either to the applied loads and/or to FEA stress results to analyze the system's margin of safety. For the design of the FOLDHOST CMC nose for an Earth entry payload retrieval system, Knoche et al applied a load safety factor of 1.1 to the input heat flux [102]. Fatemi used a stress-based margin of safety (MoS) approach for the design of EXPERT's metallic TPS [103]. An ultimate stress safety factor of 1.25 and a yield stress safety factor of 1.1 were applied. These are typical values used in structural design for uncrewed European spacecraft [104].

For this work, the MoS approach will be adopted. For a stress-based MoS analysis, equation 5.7 is applied using safety factor SF:

$$MoS = \frac{\sigma_{allowable}}{\sigma_{applied} \cdot SF} - 1 \tag{5.7}$$

A positive MoS above 0 shows an appropriate design. Due to the behavior of CMC materials, the maximum allowable stresses are taken as ultimate stresses. Therefore, the MoS stress safety factor used in this work is 1.25.

5.7. Material Considerations

5.7.1. Structural Skin

As per the purpose of this thesis project, the structural skin is to be made of a CMC material. Using equation 5.1 to calculate the maximum equilibrium wall temperature, a value of 2413 and 2486 K was found by the trajectory model for the 45° and 70° aeroshells respectively. This temperature is beyond the standard operational temperature of traditional CMCs. However, these temperatures are within the range of UHTCMCs that are being developed.

CMC Skin Temperature Limits

As mentioned in section 2.3, the properties of the DLR material C/C-SiC XB will be adopted in this work. Based on the experimental results on the material published in literature and employing a micromechanical approach for structural properties, Messe [105] generated a homogenized dataset and polynomial curves for the temperature-varying properties of C/C-SiC XB. The C/C-SiC XB thermal and mechanical properties used in this project are adopted from his work. These properties are shown in table B.1.

Oxidation poses a limitation on the maximum operating temperature of C/C-SiC [106]. The oxidation process begins at 723 K, whereby the carbon fibers begin to oxidize. Between 1573 and 1923 K, passive oxidation occurs, whereby a protective layer of silica (SiO_2) forms:

$$SiC(s) + \frac{3}{2}O_2(g) \longrightarrow SiO_2(l) + CO(g) \tag{5.8}$$

$$SiC(s) + 2\,O_2(g) \longrightarrow SiO_2(l) + CO_2(g) \tag{5.9}$$

Above 1923 K, active oxidation begins, stripping the protective silica layer away. The material recedes as the remaining SiC forms monoxide gases.

$$SiC(s) + O_2(g) \longrightarrow SiO(g) + CO(g) \tag{5.10}$$

For this reason, the maximum operating temperature of C/C-SiC is often placed up to 2073 K [107]. However, one should bear in mind that this is the maximum continuous operating temperature, as the interest for C/C-SiC TPS is typically within the realm of RLVs. Reusability is not the only criterion for this application, but also the duration of high-temperature exposure; RLVs undergo long entry trajectories, with typical durations between 15 to 20 minutes. Exceeding the 2073 K mark can therefore lead to devastating events for RLV missions. Wang et al [108] determined a maximum operational temperature of 1923 K for continuous use, 2273 to 2473 K for expendable use lasting tens of minutes to hours, and 3073 to 3273 K for applications up to minutes. The radiative equilibrium wall temperature values given at the beginning of this section are between 2400 and 2500 K. As the heat shield's operational duration is less than 4 minutes, C/C-SiC can be selected.

Due to the short duration of ballistic entry and the single-use application of the TPS as stated in requirement TPS-TH-1 in table 5.3, the operational temperature limit can be raised for this project. The thermomechanical analysis of the EXPERT nose performed by Reimer [109] showed maximum temperatures of approximately 2500 K; the duration of exposure above the continuous use temperature was over 40 seconds. The use of C/C-SiC above the continuous use temperature was justified through the rationale of a single-use mission. The ablation range for the analysis was assumed to be the same as that observed on the EXPRESS mission, where the CMC tile of the CETEX experiment showed a total ablation recession of 0.9 mm. In the EXPERT TPS thermomechanical analysis performed by Fatemi et al [99], a maximum temperature of 2328 K and 2136 K were accepted for the CMC flaps and nose respectively.

Despite the effects of atmospheric gas chemistry on CMC oxidation and surface catalycity being beyond the scope of this work, some thought was given to the effect of the Martian atmosphere on service temperature. To the author's knowledge, research on the oxidation of CMCs in the Martian entry environment is scarcely studied, but tests performed for the MarsNet heat shield are the most representative.

The test campaign included plasma tests on C/SiC in a 97% CO_2 environment. Due to the low surface catalycity rate provided by an appropriate coating, the achieved heating rates were at least half the expected heating rates [110]. This resulted in a high CO_2 dissociation rate, which decreased the maximum heat flux from 40 W/cm^2 to 15 W/cm^2 [39].

For a better understanding of the behavior and limits of SiC-based TPS materials in the Martian atmosphere, Balat and Berjoan [111] compared the passive-to-active transition temperature for SiC oxidation in air and carbon dioxide plasma conditions. It was discovered that the transition temperature only differed by 20 K. The morphology present during passive oxidation, however, was different; oxidation in air showed a consistent silica layer, while phases of SiC and even solid carbon were also present in the CO_2 environment. In the Mars environment, SiC also

reacts with carbon dioxide to form carbon monoxide - but as oxygen is more scarce compared to an Earth environment, the carbon monoxide reduces the SiC to leave pure carbon behind. For these reasons, it is assumed that the maximum continuous and intermittent temperatures are similar to those for Earth entry. Based on the maximum temperature results on the CMC components from the analyses performed by Fatemi and Walpot [99], the limit temperature of the C/C-SiC skin is set to 2350 K. Although not modeled in this work, it is assumed that a coating is applied on the C/C-SiC surface to keep its standard emissivity value constant across encountered temperatures.

To size the CMC skin, a range of thicknesses is to be set. Observing the range of thicknesses for CMC hot structures, a range between 2 and 6 mm is chosen for investigation throughout this project. The wall thickness of the IXV nose cap ranged between 1.5 to 6 mm [112], the EXPERT nose cap had a thickness of 6 mm [43], and the SHEFEX-II tiles measured 3 mm in thickness [113].

UHTCMC properties
The properties based on CNR-ISTEC's C/C-ZrB_2-SiC composite with the 2D continuous fiber architecture have been selected for use throughout this work, which are listed in table B.4. The composite's values for the specific heat capacity, however, are not reported. As this property is essential for the transient thermal analysis, the rule of mixtures in equation 5.11 was employed to give a reasonable estimation of values across a range of temperatures. This technique is used in literature for obtaining approximations of unknown properties in composites [49].

$$Cp_{tot} = Cp_m V_m + Cp_f V_f \tag{5.11}$$

Cp_m and Cp_f are the specific heat capacities of the matrix and fiber respectively, and V_m and V_f are their respective volume fractions. The specific heat capacity of the fiber was obtained from the data for graphite reported by Sheindlin et al [114], and the specific heat capacities of ZrB_2 and SiC were obtained from the data published by Tandon et al [115]. The calculated values of specific heat are reported in table B.5.

5.7.2. Thermal Insulation
Multiple options for insulation types can be used in the insulating layer, such as foams, fibrous felts and blankets, and aerogels. The choice of materials, however, is limited to fibrous materials as they are lighter than aerogels. The insulation materials are based on the availability of characterized thermal properties, as well as a compromise between their density, thermal performance, and operating temperatures. While it is important to keep areal densities low, the insulation cannot be too lightweight as its thermal performance depends on its density. Typical lightweight insulation materials are made of glass or ceramic fibers such as zirconia, alumina, and silica.

It is typical for flexible fibrous insulations to consist of multiple materials and stacks of felts or blankets sewn together as a quilt and enclosed in fabric. A schematic illustrating this concept is shown in figure 5.2. To keep the analysis simpler, no more than two insulation materials will be used for the entire thermal insulation. Therefore, one should be chosen for the high-temperature region, and one for middle-to-low-temperature regions through the thickness. As demonstrated by the Genesis capsule and the NALT project, carbon foam insulation is a common choice if highly demanding heat fluxes or temperatures are expected. However, the zirconia felt insulation RS-ZFELT by Zircar Ceramics [116] was selected instead as it is lighter than carbon foam and has a maximum operational temperature of 2473 K. This limit makes

it a suitable choice considering the vehicle's equilibrium wall temperatures. The temperature-dependent thermal properties of RS-ZFELT are shown in table B.3.

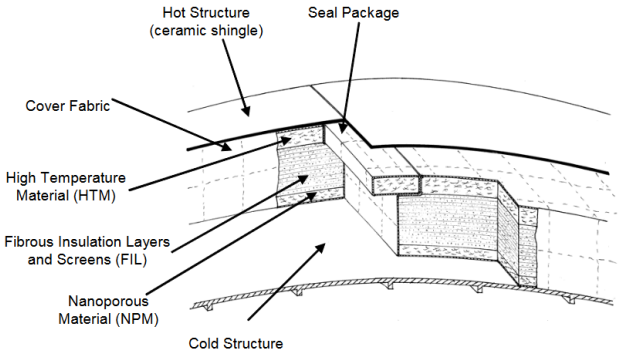

Figure 5.2: Schematic of an internal flexible insulation package developed by MT Aerospace [117].

Q-Fiber silica insulation was selected for medium to low temperatures through the thickness due to its compromise between mass and thermal performance. In addition, Kumar and Mahulikar [118] developed a polynomial curve for its thermal conductivity across a range of temperatures based on available data. Its thermal properties are included in table B.4.

Consideration of the attachment interface between the insulation and skin layers will be given here. Mechanical joints are heavy and will thus not be used. The insulation, as aforementioned, is assumed to be a quilted assembly. The same RS-ZFELT insulation used for the high temperature area can be used as the enclosing fabric. The insulation assembly can be bonded to the backface of the skin using a high-temperature adhesive; a graphite adhesive was employed for the NALT project [72]. In this case, a zirconia-based adhesive such as the Resbond® 904 [119] can be used. Its maximum service temperature is the same as the zirconia insulation, approximately 2473 K. Not only does the adhesive have the same superior operating temperature, but given that it is made of the same constituent material as the high-temperature insulation, it can be assumed that it is a part of the insulation in the thermal model.

6

Modeling

This chapter details the thermal and structural modeling of the heat shield on the finite element software package Ansys Workbench. This begins with the setup and verification of the thermal model in section 6.1, followed by the structural model in section 6.2. These sections explain the modeling practices that were performed, such as the selection of an appropriate element type and boundary conditions. Verification methods include the reproduction of a sample case from literature and comparison with closed-form solutions. Sensitivity analyses and convergence studies were performed to ensure the adequacy of crucial inputs to the models.

6.1. Thermal Model Setup

This section begins with the selection of the element type for the thermal model, followed by its inputs, boundary conditions, settings, and outputs. This is followed by the verification of the thermal model beginning with running a sample case from literature and comparing the results obtained. The section ends with a series of sensitivity analyses to test the effects of various relevant aspects such as element size, temperature dependence, and time steps.

6.1.1. Selection of Element Type

The heat shield is an axisymmetric structure. Its thickness is small compared to its radial and axial dimensions. This simplifies the choice between a solid or shell element; as it is a thin shell of revolution, a shell element is appropriate. As meshing is performed only in two dimensions, the analysis becomes much more efficient as computational time is significantly reduced.

In Ansys, there exists a thermal shell element called SHELL131 [120]. It allows for the definition of multiple layers, making it a highly suitable and convenient choice for TPS analysis. Layers of different thicknesses and materials can be defined within one element. In addition to computational efficiency, a thermal shell element provides the ease of layer thickness adjustment, in contrast to a solid element, which requires re-modeling of geometries for every iteration. SHELL131 is a four-node element that allows a selection between linear or quadratic integration order in the thickness direction. Quadratic order elements are recommended for transient analyses, especially with highly temperature-dependent materials [120]. However, if the temperature gradient is large through the thickness, as is the case for TPS, quadratic elements can yield inaccurate results, unless the thickness is partitioned through layers. For layered sections with this element type, a user-defined result can be requested on Ansys Workbench to obtain temperatures at the top, middle, and bottom of each layer. A diagram of SHELL131 is given in figure 6.1.

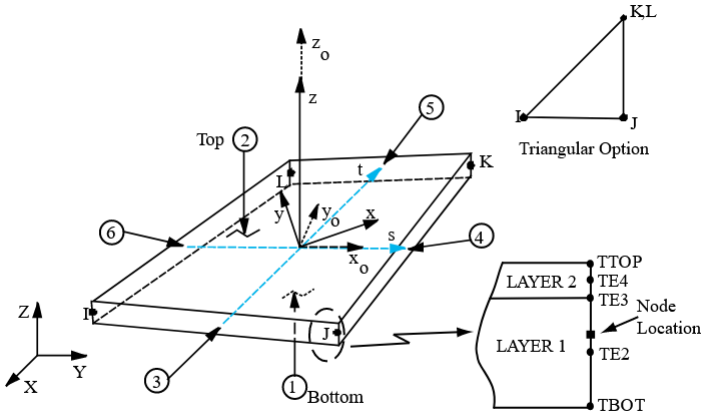

Figure 6.1: SHELL131 Geometry [120]

6.1.2. Inputs, Boundary Conditions, and Settings

A sufficiently accurate finite element model requires not only the identification of appropriate elements, but also boundary conditions, meshing and node count, load definition, and incrementation size in the case of time-dependent simulations. The transient thermal model inputs are listed in table 6.1.

Property	Value/Description
Inital Temperature	295.15 K
Analysis Time	219 s (45° aeroshell), 221 s (70° aeroshell)
Time step	1 s
Element Type	4-node quadratic order shell
Element Size	25 mm
Number of insulation thickness elements	10
Loads	Trajectory heat flux
Surface Emissivity (CMC)	0.85
Surface Emissivity (UHTCMC)	0.80
Fibrous Insulation Emissivity	0.80
Spacecraft Internal Sink Temperature	295.15 K
Ambient (space) Temperature	Trajectory Freestream Temperature

Table 6.1: Inputs, boundary conditions, and analysis settings for the transient thermal model.

The surface element size throughout the thermal analysis is 25 mm for a square panel measuring 50 mm on each side. The rationale for this choice is elaborated and verified in section 6.1.4. The surface emissivity 0.85 of the CMC layer is a typical value of C/C-SiC XB [113] [121]. This emissivity value can be relatively consistent for CMCs at different temperatures [122]. Continous-fiber UHTCMCs show more inconsistent behavior when tested by Mungiguerra et al [122], with a maximum of 0.8 before showing unsteady behavior above 2200 K. For simplicity, the value of 0.8 is maintained in this simulation.

Finally, the bottom surface emissivity of the insulation layer is assumed 0.8. Buursink [123] measured the emissivity of the alumina-based fibrous insulation Zircar ZAL-15. The emissivity of dry ZAL-15 is 0.81 at room temperature. While the silica-based Q-Fiber will be used for the medium-to-low-temperature insulation zone, it is assumed that the measured ZAL-15

emissivity is representative of most ceramic fibrous insulations. A backface emissivity value of 0.8 was also used for the Kaowool® insulation in the design of the MarsNet hot structure heat shield [60]. Therefore, the bottom face emissivity of the insulation layer is taken as 0.8.

6.1.3. Outputs

The goal for the thermal design is to ensure that the inner mold line temperature is below the required limit. It also must be ensured that none of the materials used exceed their maximum service temperature during operation. The maximum temperature of a TPS material takes place at the top surface of its respective layer. On Ansys, a user-specified result can be defined to request the temperature history at thickness nodes of interest. The output results for the thermal model are temperature history outputs. The points of interest are:

- **TPS Outer Mold Line temperature (T_w).** This is the top surface of the CMC skin exposed to the flow. Ansys defines this result as "TTOP", but it shall henceforth be called T_w in this work.
- **Interface temperature between skin and high-temperature insulation (T_{i1}).** This is the temperature at the bottom of the CMC skin and the top of the high-temperature insulation, which must not exceed the limit temperature of the high-temperature insulation. For a total insulation layer divided into 10 thickness segments, with each insulation material consisting of 5 segments, Ansys recognizes this output as "TE21". This corresponds to the 21st node from the bottom of the element.
- **Interface temperature between high- and medium-temperature insulation (T_{i2}).** This is the temperature at the bottom of the CMC skin and the top of the high-temperature insulation. For the aforementioned thickness division, Ansys recognizes this output as "TE11".
- **TPS inner mold line temperature (T_b).** This is the temperature at the backface of the TPS, recognized by Ansys as "TBOT".

6.1.4. Transient Thermal Model Verification

As stated in section 6.1.1, a quadratic order for SHELL131 can cause inaccurate and unstable results if not partitioned properly in the thickness direction. To ensure correct practices in using a quadratic element order and the application of appropriate boundary conditions for transient analysis, a test case from literature is replicated. Following this, sensitivity analyses are performed on meshing, thickness layer partitioning, and time steps to observe their effect on results.

Verification with Sample Case: RLV TPS

Cowart and Olds [124] performed a series of test cases on a reinforced carbon-carbon (RCC) TPS to develop a sizing software for RLV TPS design. The software, called TCAT (Thermal Calculation Analysis Tool), employs the implicit Newton-Raphson method. Two test cases from their work are reproduced in Ansys, which employs the implicit backward Euler integration scheme by default for transient thermal analyses [120].

In the first test case, an RCC tile is exposed to a constant heat flux of 20 W/cm^2 for 2000 seconds. Re-radiation is present at the top and bottom surface of the tile. Its initial temperature is 300 K. The RCC material properties and simulation settings are given in table 6.2.

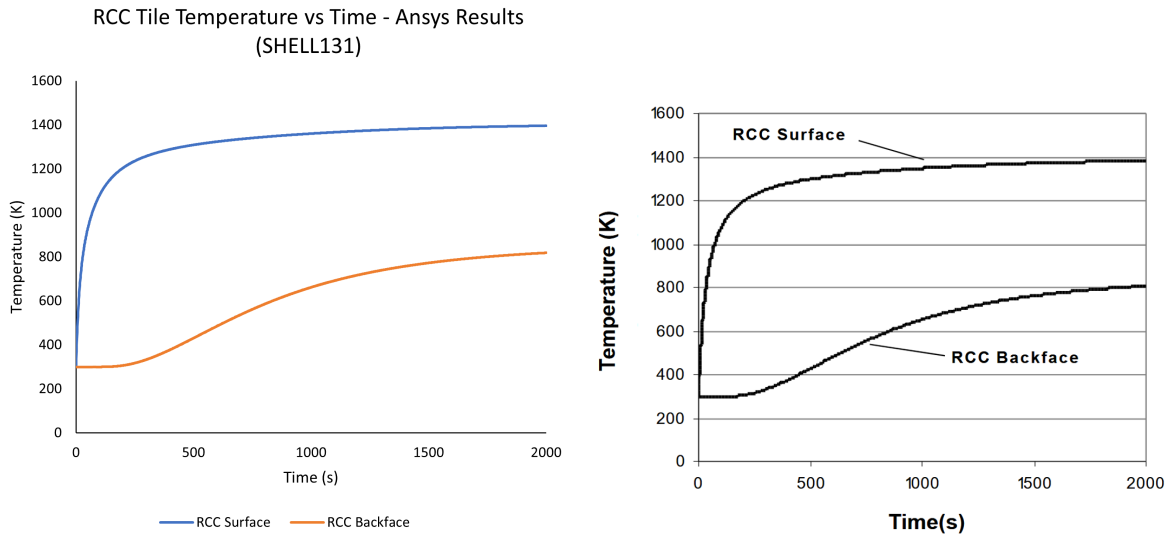

(a) RCC tile temperature history from Ansys model.

(b) RCC tile temperature history from [124].

Figure 6.2: Comparison of RCC tile temperature histories.

Density	1580 kg/m^3
Specific Heat	0.77 kJ/kgK
Thermal Conductivity	4.30 W/mK
RCC thickness	0.10 m
Time step	1 s
Number of Thickness Nodes	10

Table 6.2: RCC tile case properties [124]

The analysis was done on a 50 mm$\times$ 50 mm square tile. The quadratic SHELL131 element, as shown in figure 6.1, has 3 nodes per layer: the top, middle, and bottom nodes. Therefore, the thickness of the RCC tile was split into 4 layers, i.e. 9 thickness nodes were used instead of 10. Due to an equal heat flux on the surface of the panel, the element size across the panel face was not deemed critical and was given a size of 20 mm. An assumed radiative emissivity of 0.8 to a sink temperature of 300 K was given on the top and bottom surfaces as these values were not given. The temperature histories of the top and back faces of the tile given by the Ansys model are plotted in figure 6.2a, and the original in figure 6.2b.

The replicated temperature history plot of the RCC tile appears to be identical to the original plot. Giving a final temperature of 1397 K and 819 K for the top and back surfaces respectively, the results are confirmed in the paper, which stated that these final temperatures are approximately 1400 K and 800 K.

Next, the case with the TPS stack of five materials was replicated. The heating trajectory of the STS-1 mission was imposed on the stack. As the values were not reported, the Plot Digitizer web app [125] was used to extract data points from the stagnation point heating history plot given in the paper. The materials and their respective thicknesses are given in table 6.3. Given their thicknesses, the RCC layer was again divided into 4 layers, the aluminum layer into 2, and the other materials only consisted of 1 layer.

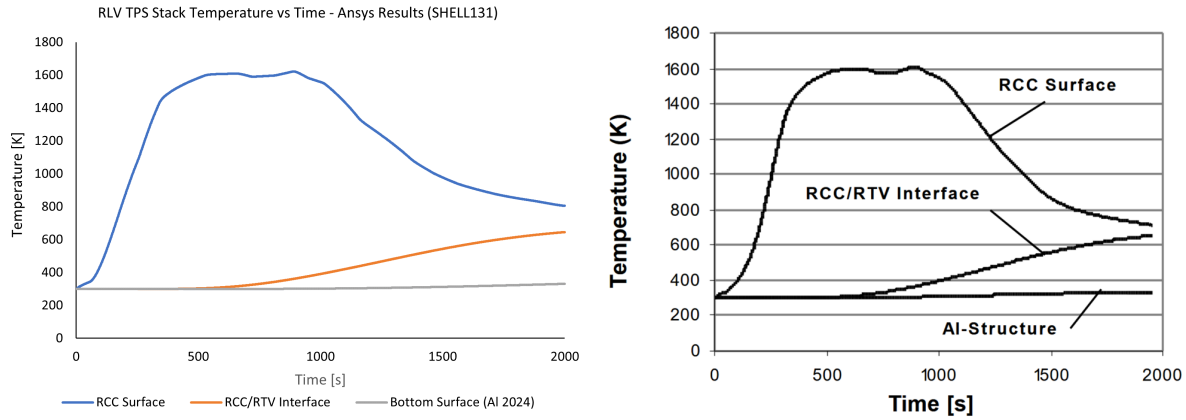

(a) RCC TPS stack temperature history from Ansys model.

(b) RCC TPS stack temperature history from [124].

Figure 6.3: Comparison of RCC TPS stack temperature histories.

Material	Thickness (mm)	Number of Nodes
RCC	152.4	10
RTV	2.0	3
SIP	4.0	3
RTV	2.0	3
Al-Structure	25.4	5

Table 6.3: RCC tile case properties [124]

The material properties were not given; the paper reported that the values were extracted from the NASA TPSX database [126]. Consequently, the values used in the Ansys models were also extracted from the current TPSX database, taking the aluminum material as Aluminum Alloy 2024-T6, as used on the Space Shuttle's airframe. The values used for these materials are recorded in table B.12. The surface emissivity is again taken as 0.8 to a sink temperature of 300 K on both sides. The TPS temperature history from the Ansys model is plotted in figure 6.3a, and the original in figure 6.3b.

The paper reported a maximum RCC surface temperature of approximately 1600 K; 1622 K was obtained. The temperature history of the aluminum structure matches that of the paper, being reported as almost constant at 300 K. A final temperature of 331 K was obtained. The plots obtained from the Ansys model are comparable and similar to the actual plot, with the RCC/RTV interface exceeding a final temperature of over 600 K. However, the cooling history of the RCC surface is slower than the original plot, not crossing below 800 K. This difference may be due to subtle differences in the trajectory heating plot or the different integration methods employed by Ansys and TCAT. Nevertheless, modeling practices were deemed acceptable given the similarities of the plots and recorded temperatures.

Sensitivity Analysis: Partitioning and Temperature Dependence

The material properties for a non-temperature-dependent system are shown in table 6.4. The temperature-dependent system takes the thermal conductivities and specific heat capacities of C/C-SiC XB and Zircar RS-ZFELT in Appendix B.

Material	Density [kg/m^3]	k [W/mK]	Cp [J/gK]
C/C-SiC XB	1900.0	7.0	1550.0
RS-ZFELT	240.0	0.3	753.6

Table 6.4: Materials without temperature dependence.

The initial temperature of the system is 295.15 K. The heat flux history of the 70° heat shield, given in figure 6.4, was applied to the panel surface for this series of sensitivity analyses. The maximum heat flux takes place at 72.5 seconds and heat shield jettison takes place at 221 seconds.

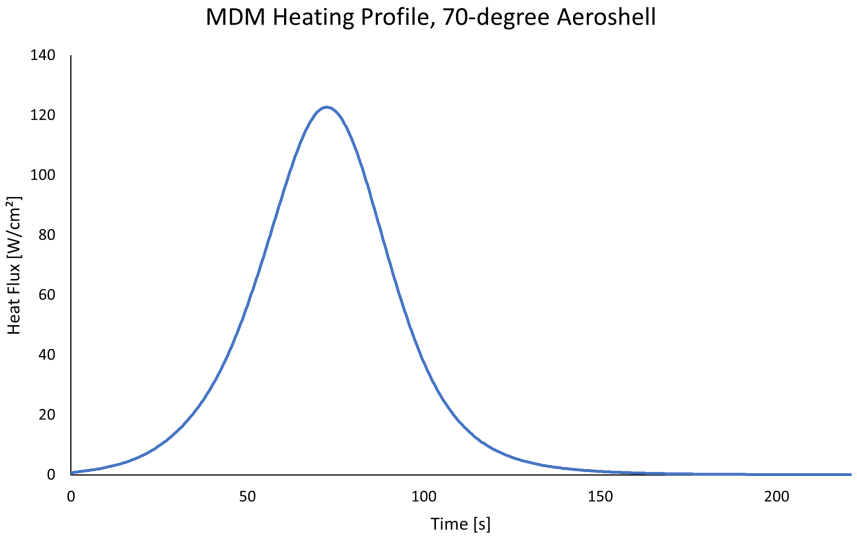

Figure 6.4: Stagnation point heating history for the 70° aeroshell.

For this series of sensitivity studies for model verification, the emissivity at the top and bottom surfaces will also be kept constant at 0.8 for a better comparison with steady-state thermal results; this value will be changed during the actual TPS sizing in section 7.1. In a steady-state analysis, with radiation on top and bottom surfaces, emissivity values must be kept similar. Different emissivity values can lead to a discrepancy between the heat transfer rates calculated through radiation and those through conduction, leading to further inaccuracies. The back surface radiates to a constant spacecraft sink temperature of 295.15 K. The top surface radiates to the varying freestream temperature in the atmosphere. For the partitioned system, the insulation layer was divided into 10 segments. This results in 21 nodes along the insulation. Given that the insulation is 40 mm, each segment is 4 mm thick. All simulations were run with a time step of 1 second. The simulation parameters and settings used throughout these studies are given in table 6.5.

Property	Value	Unit
Initial Temperature	295.15	K
Analysis Time	221	s
Time Step	1	s
Number of insulation thickness divisions	10	-
Planar Element Size	25	mm
Surface Emissivity	0.80	-
Backface Emissivity	0.80	-
Spacecraft internal temperature	295.15	K

Table 6.5: Simulation settings and parameters for the thermal verification sensitivity studies.

The surface and bottom temperatures T_w and T_b are presented in table 6.6 for different cases of partitioning and temperature dependence.

Case	T_w (t=72.5 s) [K]	T_w Max [K]	T_b (t=72.5 s) [K]	T_b Max [K]	T_b (t = 221 s) [K]
No partition, no temperature dependence	-	703.4	-	-17.5	Simulation crashes
No partition, temperature dependent	-	2200.1	-	715.2	Simulation crashes
Partitioned, no temperature dependence	2153.0	2197.7	295.5	506.6	506.6
Partitioned, temperature dependent	2175.1	2209.4	295.2	335.2	335.2
Steady-State Analysis	2275.4	-	717.1	-	-

Table 6.6: TPS top and bottom surface temperatures for different cases of partitioning and temperature dependence.

From the results in table 6.6, it can be observed that using a quadratic-order shell element without partitioning leads to highly inaccurate and incomplete results. The simulations crash before a converged solution can be found. The backface temperature achieves a high maximum temperature before the end of the trajectory. Proper partitioning leads to a converged solution. An important conclusion from the transient analyses is that the maximum temperature does not take place at the time of maximum heating. The non-temperature-dependent system, as expected, leads to conservative results for the backface. The temperature-dependent system gives a lower temperature for the backface, but higher wall temperatures. This is expected as less heat is conducted towards the bottom of the TPS, resulting in less rejection of heat by radiation from the top surface.

The non-temperature-dependent system, however, serves as the best point of comparison to the steady-state analysis as it uses the same material thermal conductivities. The transient wall temperature encountered at the time of peak heating is lower than the steady-state result

by 122 K. The maximum transient wall temperature differs by 78 K from the steady-state wall temperature. Finally, the backface temperature for the steady-state result is 432 K higher than the transient result at the time of peak heating, and higher than the corresponding maximum transient temperature by over 221 K. It can be seen that a steady-state analysis provides excessively high and inaccurate temperatures. For initial TPS sizing, it is best to therefore perform a transient analysis with unchanging and conservative material properties as a first estimate of temperatures, as steady-state results may lead to oversizing of the TPS if taken as base values.

Thickness Increment and Mesh Convergence

Now, the effect of nodal points on backface temperatures is analyzed. The temperature-dependent TPS is analyzed with the same conditions in table 6.5. The number of nodes through the thickness is controlled by adjusting the size of thickness increments through the insulation layer. The thickness increment size and maximum backface temperatures are given in table 6.7. The backface temperature history for different thickness increments are shown in figure 6.5.

Number of Increments	Increment Size [mm]	Number of Nodes	T_b Max [K]
10.00	4.00	21.00	335.19
8.00	5.00	17.00	334.93
5.00	8.00	11.00	334.02
4.00	10.00	9.00	334.27
2.00	20.00	5.00	359.35 (Unstable)
1.00	40.00	3.00	715.18 (Unconverged)

Table 6.7: Insulation thickness partitioning study on backface temperature.

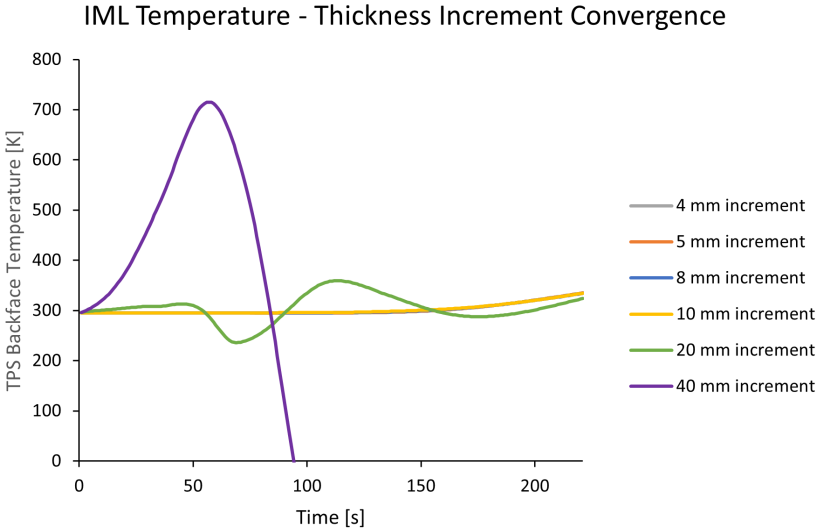

Figure 6.5: Backface temperature history for different insulation thickness increments.

Figure 6.5 shows that the larger the thickness increment, the more unstable the solution becomes; a 20 mm increment converges to a solution but shows wobbling and instability over

time. For increments below 10 mm, the maximum temperature is achieved at the end of the trajectory, which is expected behavior. The difference in these values is small, with a difference of only 1 K between an increment size of 4 and 10 mm. Therefore, for the TPS thermal analysis, the entire insulating layer will be partitioned into ten incremental layers, with each layer not exceeding 10 mm during the sizing study.

As aforementioned, the effect of surface meshing is considered to play a negligible effect on the TPS temperatures as the heat flux is equal throughout the panel surface. To demonstrate this hypothesis, the effect of panel surface element size on the backface temperature is studied. Table 6.8 shows the maximum backface temperatures for different surface element sizes.

Element Size [mm]	T_b Max [K]
10.00	335.15
15.00	335.17
20.00	335.19
25.00	335.19
50.00	335.28

Table 6.8: Backface temperature mesh convergence study.

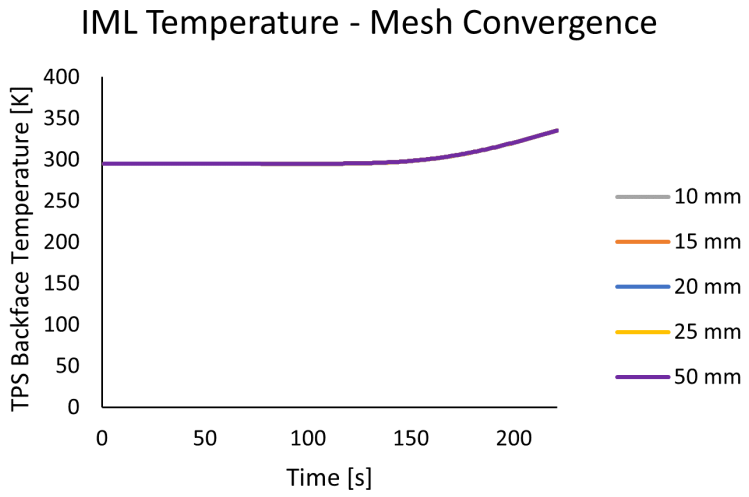

Figure 6.6: Backface temperature history for different surface element sizes.

From table 6.8, it can be observed that a negligible difference of 0.13 K is present by changing the element size from 10 mm to 50 mm. 50 mm means only one element on the surface as it corresponds to the length of the square panel. The backface temperature history curves plotted for different element sizes in figure 6.6 prove the triviality of surface meshing for this case. A surface element size of 25 mm is therefore acceptable.

Sensitivity Analysis: Time Steps

The determination of time increments is critical to a transient thermal analysis. According to Ferraiuolo and Manca [127], the variation in time must be such that the difference in heat flux must be less than 1% of the maximum heat flux. The baseline 1-second step size is sufficient,

but for completeness, the effect of time step size on the maximum wall temperature is shown in table 6.9.

Time increment [s]	T_w Max [K]
0.5	2211.6
1.0	2209.4
3.0	2199.3
5.0	2184.6
7.0	2180.3
9.0	2170.9
10.0	2162.0
25.0	2133.3

Table 6.9: Effect of time step on maximum wall temperature.

Between a time step of 1 second and 0.5 seconds, a difference of less than 2 K in maximum wall temperature can be observed, and a difference of approximately 76 K is seen between an increment of 1 and 25 seconds.

Panel and Shell Comparison
In the last step of setting up the thermal model, a comparison of temperature histories between a panel and the heat shield shell was made. It was assumed that, based on the assumption of constant heating throughout the entire heat shield, running thermal analyses on a square panel would suffice. Thermal analyses on a panel geometry compared to the shell would be much more quick and efficient; it was assumed that the results would not differ by a large extent. For further computational efficiency on the shell, as it is much larger than the panel, only a quarter of it was modeled and symmetry was applied. An element size of 50 mm was applied to both models, with the rest of the conditions kept the same as in table 6.5. Figure 6.7 plots the results of the temperature histories of the CMC wall, the interface between the CMC and insulation, and the TPS backface for the panel and the shell. Table 6.10 shows the differences in maximum temperatures between both models. It is confirmed that the difference between both models is negligible, amounting to an error of approximately 0%.

Temperature Zone	Panel	Shell	Error [%]
Surface	2209.4	2209.6	-0.0
Interface	2185.2	2185.4	-0.0
Backface	335.2	335.0	-0.1

Table 6.10: Comparison of maximum temperatures between the panel and the wall.

6.2. Structural Model Setup

Just as reported for the thermal model setup, this section begins with the element type selection for the structural model, followed by its inputs, settings, and outputs. The verification of boundary conditions was performed through a linear buckling analysis. The model's results for the critical buckling load of a simple spherical dome for two boundary conditions are compared to that of a closed form solution. This is followed by the meshing verification of the heat shield, performed through a mesh convergence study.

6.2.1. Selection of Element Type

From a structural perspective, shell elements capture bending responses more accurately compared to solid elements. This is important as the assessment of bending stress is critical

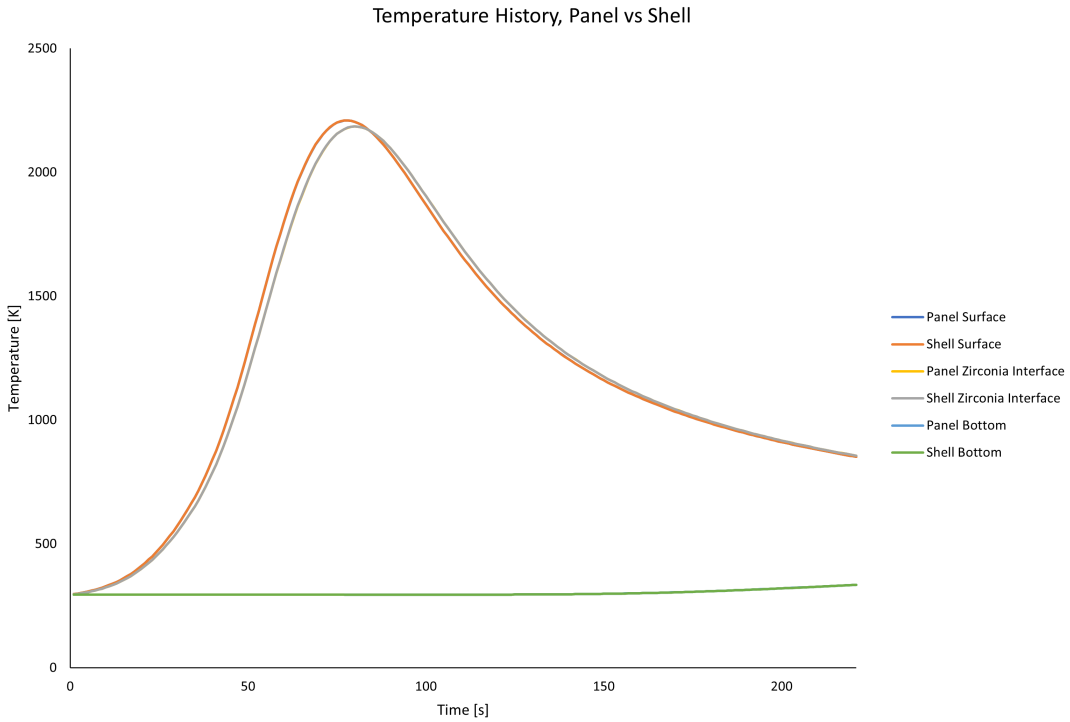

Figure 6.7: Comparison of temperature histories between a panel and a shell.

to ensuring that the heat shield does not exceed the maximum flexural strength of the skin material. SHELL181 and SHELL281 are structural shell elements on Ansys [120]; the former is a linear-order four-node element, while the latter is a quadratic-order eight-node element. As it is of interest to analyze the membrane and bending stresses only at in-plane directions, and given computational efficiency, the SHELL181 element would suffice. A diagram of the element is shown in figure 6.8.

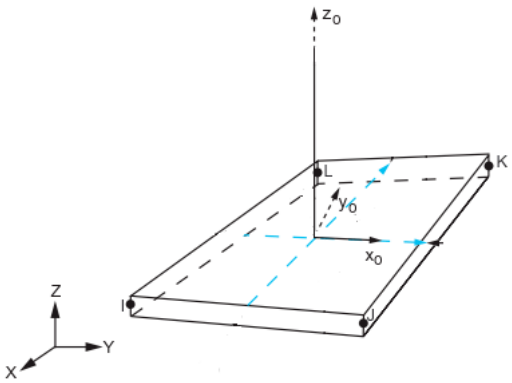

Figure 6.8: SHELL181 Geometry [120]

6.2.2. Inputs, Boundary Conditions, and Settings

Table 6.11 lists the inputs and settings that were used in the static structural model to assess the stresses and failure modes of the heat shield.

Property	Value/Description
Element Type	4-node linear order shell
Element Size	10 mm
Loads	Flight pressure, skin surface temperatures from thermal model
Boundary Condition	Simply Supported

Table 6.11: Inputs, boundary conditions, and analysis settings for the static (thermo)structural model.

6.2.3. Outputs

For the eigenvalue buckling analysis, the load multiplier corresponding to the first buckling mode is simply requested. For the static stress analysis, the field outputs were requested:

- **Hoop Stress.** These are the stress values in the circumferential direction of the heat shield shell. Membrane stress results in the local element direction 11 (corresponding to the red lines in figure 6.9) were extracted for this result.
- **Meridional Stress.** These are the stress values in the longitudinal direction of the shell. Membrane stress results in the local element direction 22 (corresponding to the green lines in figure 6.9) were extracted for this result.
- **Bending Stress, Hoop Direction.** These are the bending stress results along the local element direction 11.
- **Bending Stress, Meridional Direction.** These are the bending stress results along the local element direction 22.
- **Vertical Displacement.** This is the displacement of the shell in the Z-direction of the shell's cylindrical coordinate system shown in figure 6.10. A positive vertical displacement corresponds to elongation along the Z-axis.
- **Radial Displacement.** This is the displacement of the shell in the X-direction of the shell's cylindrical coordinate system shown in figure 6.10. A positive radial displacement corresponds to radial expansion.

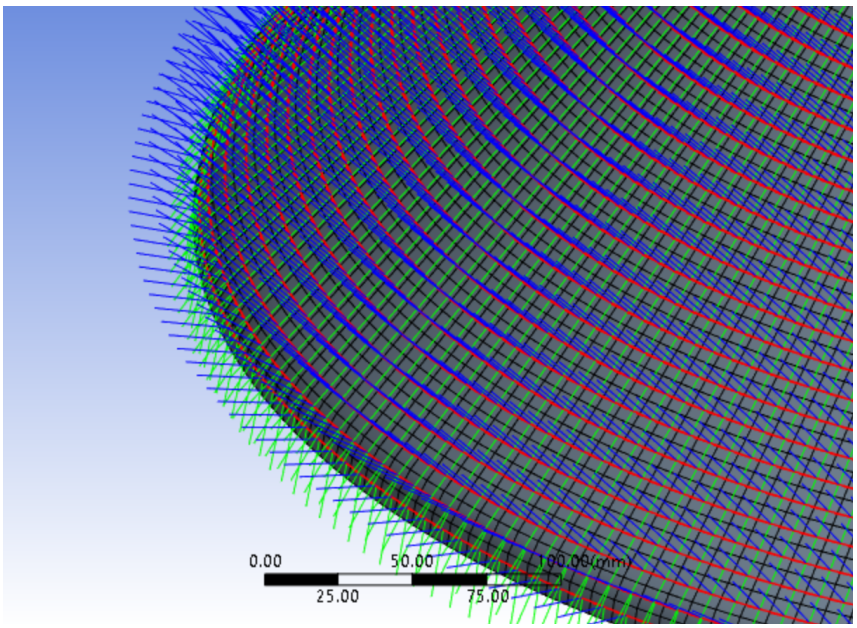

Figure 6.9: Element orientations for the structural model.

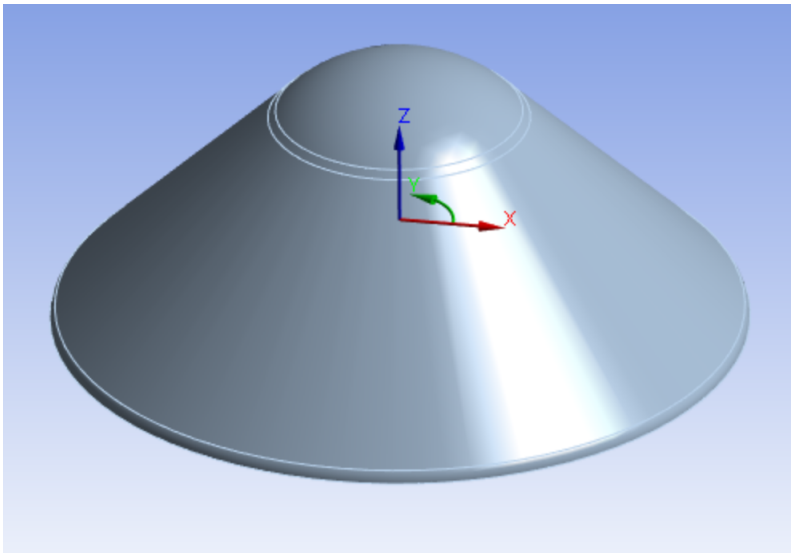

Figure 6.10: Cylindrical coordinate system of the heat shield shell.

6.2.4. Shell Meshing

The accuracy of an FE model can strongly be affected by the size, shape, and distribution of elements in its mesh. With a shell element, triangular elements must be avoided as they result in stiffer behavior. A quad-dominated, or an all-quad mesh, if possible, must be implemented. Given the geometry of the heat shield, this can be a complex practice. The Multizone mesher on Ansys was used with a uniform, all quad setting was selected. This, however, does not guarantee uniformity and a completely quad mesh. Therefore, the model was partitioned near areas prone to triangulation while ensuring that the aspect ratio of the quad mesh does not exceed 5. The partitions were circular, made near the edge of the spherical nose, and in the case of the 70° heat shield, halfway through the cone generator. The partitioning zones for the 70° heat shield are shown in figure 6.11.

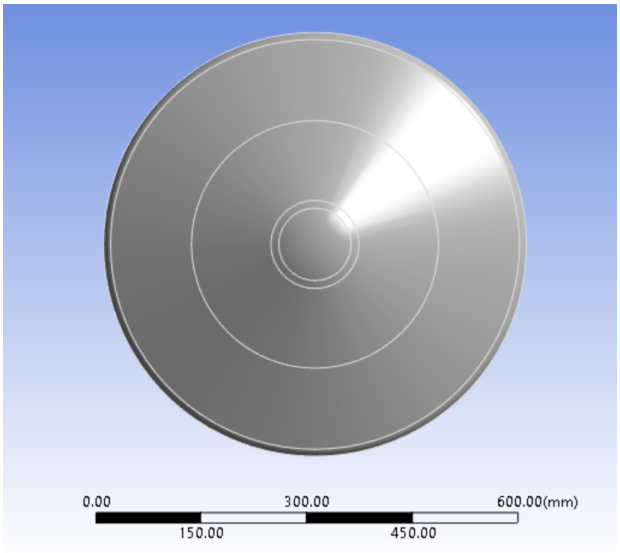

Figure 6.11: Partitioning of faces for meshing the 70° heat shield.

6.2.5. Structural Model Verification

Boundary Condition Verification with Buckling Equation

As stated in section 5.5, buckling is one of the two failure modes analyzed in the structural models. At this conceptual stage of the design, a linear buckling analysis is sufficient as the imperfections due to manufacturing and geometry are unknown. As shown in table 6.11, simple supports are considered at the base of the heat shield. This means that all displacements are constrained such that only rotations are allowed at the base. The heat shield is an axisymmetric shell, and as the pressure loads are assumed to be uniform, the loading is also axisymmetric. It is, however, a complex geometry consisting of a spherical cap, a cone, and a small toroidal segment, therefore it is not straightforward to cross-check boundary conditions with hand calculations. As the heat shield is a closed shell, a closed shell with a simple geometry can be used as a representative test case.

The buckling of a spherical dome under external pressure will be modeled to ensure that the correct boundary condition is used. The buckling pressure load will be compared for clamped and simply-supported boundary conditions. The shell is assumed to be perfect with no geometric imperfections. The classical buckling pressure of a spherical dome can be easily calculated using equation 6.1 from the NASA-8032 manual [128]:

$$P_{crit} = \frac{2E}{\sqrt{3(1-\mu^2)}}(\frac{t}{R^2}) \tag{6.1}$$

E is the material's modulus of elasticity and its Poisson's ratio is μ. R is the base radius of the spherical cap and t is its thickness. The dimensional and material properties of the spherical cap are taken from [129]. The shell was partitioned into quarters to apply a quad-dominated mesh with an element size of 1.1 mm. Ansys uses the Block Lanczos method for eigenvalue buckling analyses, which is formulated in equation 6.2 [130]:

$$([K] + \lambda_i[S])\phi_i = 0 \tag{6.2}$$

For the number of modes i, eigenvalue λ_i is the multiplier to a given input load; it is not exactly the critical buckling load. However, with an input load of unity, λ_i gives the critical buckling pressure in the applied unit system. Eigenvector ϕ_i is the corresponding buckling mode to the load. They are extracted using stiffness matrix [K] and stress matrix [S]. As buckling is to be avoided at all costs, only the first buckling mode is of interest. A unit load of 1 MPa is applied to the spherical cap for two cases of different boundary conditions. Table 6.12 compares the numerical results for buckling loads using a simply supported and a clamped boundary condition to the critical buckling load calculated from equation 6.1.

Analysis	P_{crit} [MPa]	Error [%]
Theoretical	23.46	-
Simply Supported	23.46	0.00%
Clamped	23.75	1.26%

Table 6.12: Comparison of numerical and analytical buckling pressures of a spherical cap.

Table 6.12 shows that the simply supported boundary conditions match the analytical calculations exactly, while clamped conditions overpredict it by over 1%. Their first buckling mode shapes are different; the simply-supported case in figure 6.12a shows half-symmetry while the clamped mode shape in figure 6.12b is axisymmetric.

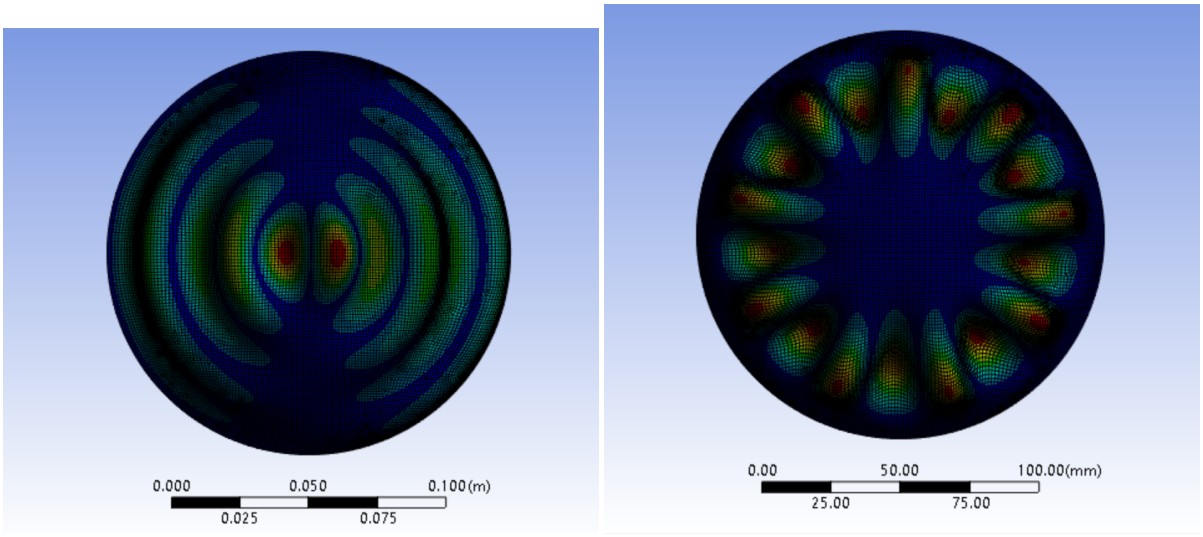

(a) First buckling mode of the simply supported spherical cap. **(b)** First buckling mode of the clamped spherical cap.

Figure 6.12: First buckling mode shapes for spherical caps with different boundary conditions.

Mesh convergence

With the simply supported boundary condition verified, a mesh convergence study is performed on the heat shield. A surface pressure of 1 MPa applied. The effect of element size on the linear buckling pressure was investigated. The shell thickness was arbitrarily set to 2 mm. The results are given in table 6.13. The resultant plot is shown in figure 6.13.

Element Size [mm]	Buckling Pressure [kPa]
10.0	97.5
15.0	98.0
20.0	100.0
25.0	101.0
30.0	102.5
35.0	104.1
40.0	105.9
45.0	108.5
50.0	110.5

Table 6.13: Mesh convergence study on buckling pressure on the 45° heat shield.

The plot appears to approach convergence towards 20 mm, however, a dip occurs from 20 mm to 15 mm, and no significant change is observed from 15 mm to 10 mm. Therefore, an element size of 10 mm was selected.
The buckling verification case confirmed that a simply-supported boundary condition is appropriate.

With the thermal and structural models set up, and the modeling practices and simulation properties in tables 6.1 and 6.11 verified, the TPS sizing and analysis process can begin.

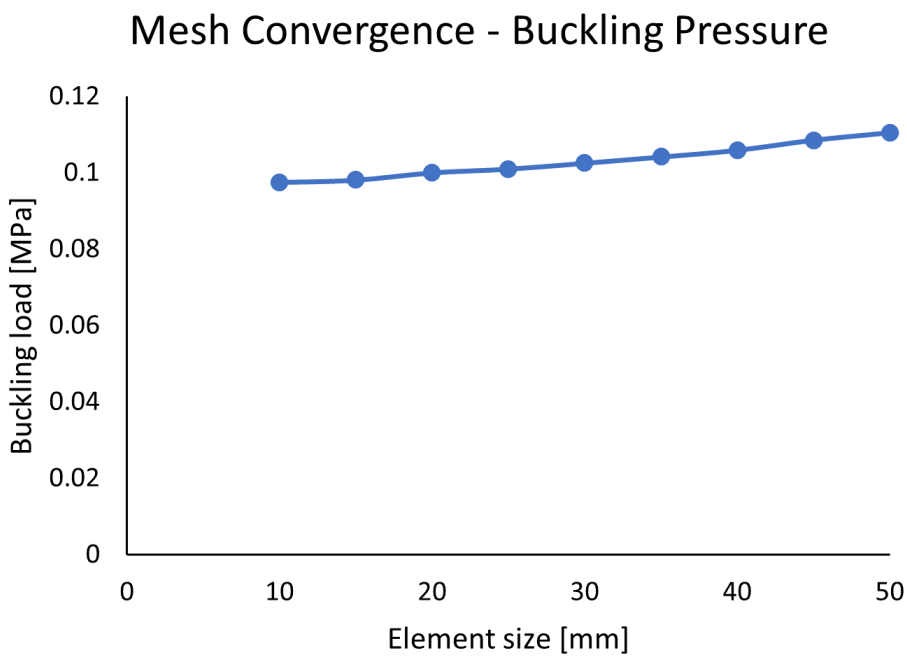

Figure 6.13: Mesh convergence plot for the critical buckling load of the 45° heat shield.

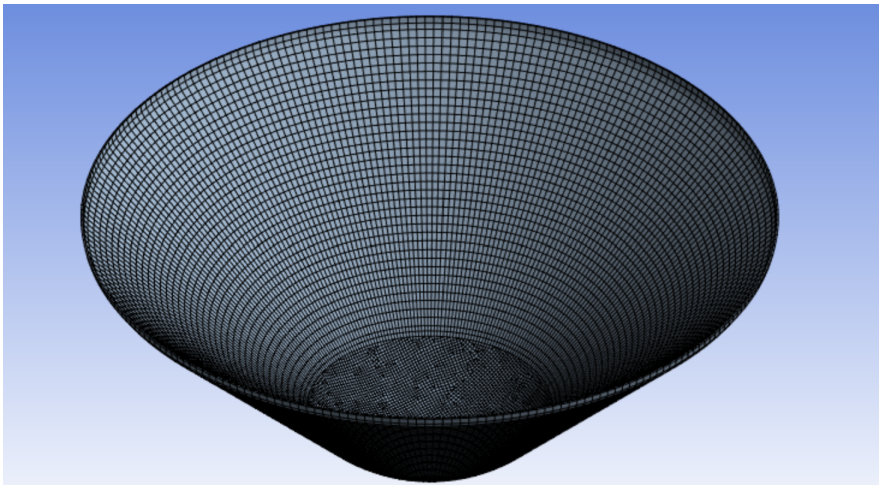

Figure 6.14: 45° heat shield quad meshed with an element size of 10 mm.

7

Sizing and Parametric Study

The FE models were set up and verified in the previous chapter. This chapter will begin with the thermal sizing of the 45° vehicle with the CMC material in section 7.1, and the structural analyses will follow in section 7.2. The structural analysis will present three cases: the maximum pressure alone, the maximum pressure with the corresponding skin temperatures, and the maximum skin temperatures with the corresponding pressure applied. Afterward, the results for the TPS on the same heat shield with a UHTCMC skin will be compared in section 7.3, and the results for the second heat shield size for both materials in section 7.4.

7.1. Thermal Sizing

In this section, the 45° heat shield with C/C-SiC XB, will be sized. The heating profile over time, given by the trajectory model in section 4.5, is given in figure 7.1. The heat shield is jettisoned at 219 seconds.

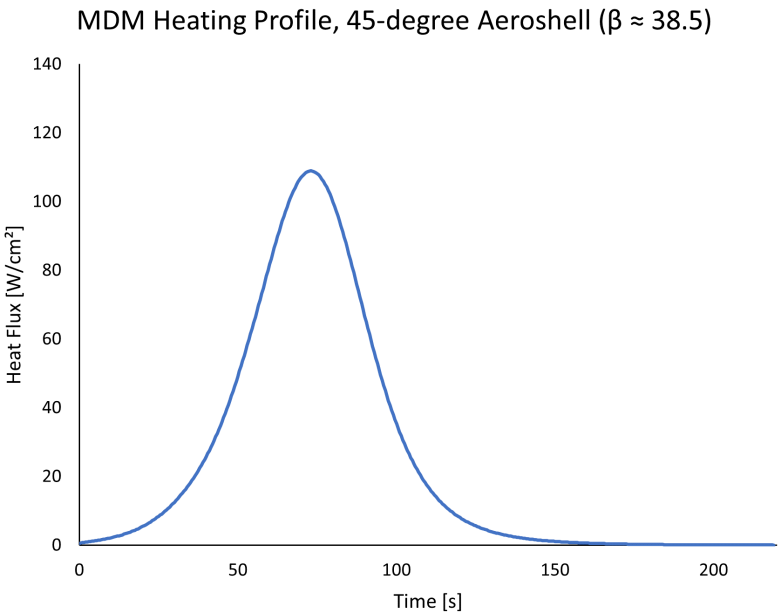

Figure 7.1: Heating profile of the 45° heat shield.

For this vehicle size, the areal density of the TPS must not exceed 11.2 kg/m^3. Both the high and lower-temperature insulation materials will be used. The system will be sized such the mass constraints are satisfied and that the maximum temperature of each layer does not exceed their material's intermittent use temperature. The material limit temperatures are given in figure 7.1.

Material	Limit Temperature [K]
C/C-SiC XB	2350
C/C-ZrB_2-SiC	2500
RS-ZFELT	2273 [116]
Q-Fiber	1533 [131]
IML (Backface)	450

Table 7.1: TPS material limit temperatures.

The sizing process begins with increasing the thickness of the skin as the insulation layers are kept constant. The appropriate skin thickness will be chosen. Then, each insulation material will be sized individually with the chosen skin thickness. Finally, a combination of different insulation sizes will be analyzed while ensuring that the areal density of the system does not exceed requirements. Table 7.2 gives the starting thicknesses.

Skin	RS-ZFELT	Q-Fiber
2 mm	20 mm	20 mm

Table 7.2: TPS starting thicknesses.

7.1.1. C/C-SiC Skin Sizing

The maximum surface (T_w), CMC-to-insulation interface (T_{i1}), insulation-to-insulation interface (T_{i2}), and backface (T_b) temperatures are investigated for a thickness increase of 1 mm. Both insulation layers are kept at a constant thickness. The results are given in table 7.3.

Skin Thickness [mm]	RS-ZFELT Thickness [mm]	Q-Fiber Thickness [mm]	T_w [K]	T_{i1} [K]	T_{i2} [K]	T_b [K]
2.00	20.00	20.00	2139.57	2126.74	803.18	361.43
3.00	20.00	20.00	2105.00	2082.94	801.03	354.70
4.00	20.00	20.00	2051.86	2017.92	796.84	348.15
5.00	20.00	20.00	1988.76	1939.80	787.61	341.62
6.00	20.00	20.00	1923.13	1856.65	772.23	335.17
7.00	20.00	20.00	1859.79	1773.10	751.80	329.21

Table 7.3: Maximum temperature response to skin thickness

As the skin increases in thickness, the magnitude in surface temperature change increases. The interface temperature experiences this change more dramatically. The second interface and bottom temperature are also affected, but not to a large extent as the CMC skin. This is expected due to the poor conduction of the insulation layer. The maximum temperature of the skin's surface is within the required temperature limit. A 3 mm thickness instead of 2 mm was chosen to account for recession due to oxidation.

7.1.2. Insulation sizing

The insulation layers are now sized with the selected 3 mm skin thickness. Table 7.4 shows the effect of TPS temperatures when the zirconia insulation is changed with everything else constant, and table 7.5 for the Q-Fiber insulation.

Skin Thickness [mm]	RS-ZFELT Thickness [mm]	Q-Fiber Thickness [mm]	T_w [K]	T_{i1} [K]	T_{i2} [K]	T_b [K]
3.00	5.00	20.00	2108.11	2089.70	1796.43	521.03
3.00	10.00	20.00	2104.67	2082.24	1350.90	479.30
3.00	15.00	20.00	2104.75	2082.35	1012.40	422.06
3.00	20.00	20.00	2105.00	2082.94	801.03	354.70

Table 7.4: Maximum temperature response to zirconia insulation sizing

Skin Thickness [mm]	RS-ZFELT Thickness [mm]	Q-Fiber Thickness [mm]	T_w [K]	T_{i1} [K]	T_{i2} [K]	T_b [K]
3.00	20.00	5.00	2105.00	2082.94	763.21	509.21
3.00	20.00	10.00	2105.00	2082.94	797.24	459.63
3.00	20.00	15.00	2105.00	2082.94	801.50	406.10
3.00	20.00	20.00	2105.00	2082.94	801.03	354.70

Table 7.5: Maximum temperature response to Q-Fiber insulation sizing

Unless the total zirconia insulation is thin, adjusting the zirconia insulation has small effects on the wall and interface temperatures, while affecting everything else below. The Q-Fiber has no effect on the wall and CMC interface temperature, while an increase in thickness causes the second interface temperature to increase, and then converge between 15 and 20 mm, primarily affecting the backface temperature. This increase in the second interface temperature with an increase of temperature is observed due to the thermal balance at that point. This interface receives heat input by conduction from the zirconia insulation, which is small, and rejects heat by conduction towards the bottom layer. As this layer is increased, the conductive heat leaving this interface is larger. To compensate, the conduction entering this interface is smaller, which can be seen in a reduced thermal gradient between interfaces 1 and 2. As the temperature of interface 1 is constant due to the poor thermal conductivity of the zirconia insulation, the temperature of interface 2 increases.

Finally, different combinations of insulation thicknesses were adjusted until the best compromise of areal densities and temperatures was found. The zirconia felt is much denser than the Q-fiber; an optimal system employs the thinnest layer of zirconia and a thicker layer of Q-fiber. Based on tables 7.4 and 7.5, the targeted maximum configuration is a zirconia thickness of 10 mm and a Q-fiber thickness of 30 mm. Table 7.6 shows the results for three combinations.

Skin Thickness [mm]	RS-ZFELT Thickness [mm]	Q-Fiber Thickness [mm]	T_w [K]	T_{i1} [K]	T_{i2} [K]	T_b [K]	Areal Density [kg/m^2]
3.00	10.00	25.00	2104.67	2082.24	1351.56	432.97	9.50
3.00	9.00	26.00	2104.77	2082.52	1440.14	433.44	9.32
3.00	8.00	26.00	2105.03	2083.13	1532.30	443.02	9.08

Table 7.6: Adjustment of insulation layers for final sizing.

The third case in table 7.6 kept temperatures below the maximum. The temperature history for these thicknesses with a 3 mm skin is shown in figure 7.2.

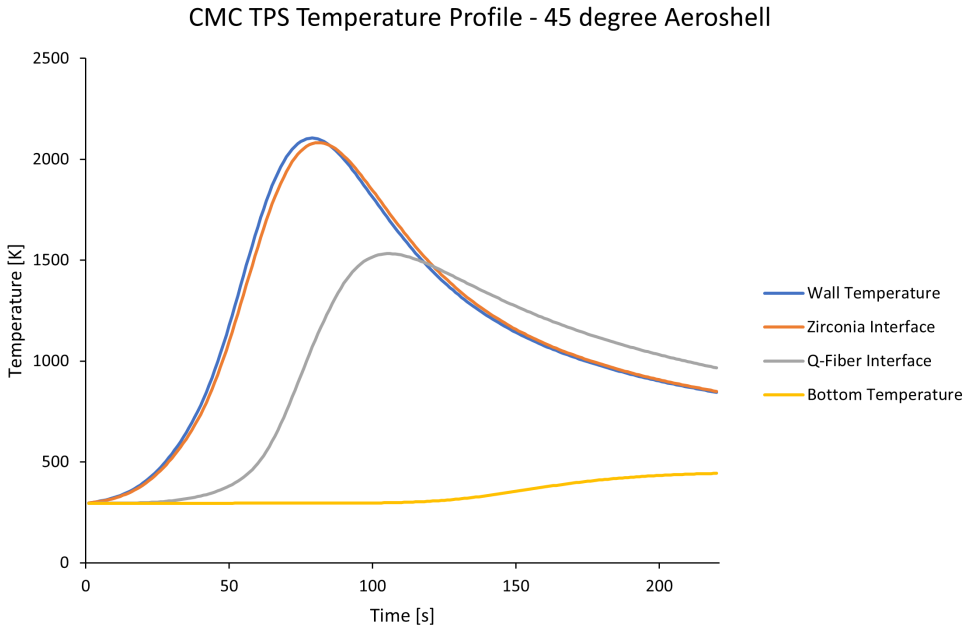

Figure 7.2: Temperature history of the sized CMC TPS on the 45° aeroshell.

7.2. Structural Analysis

The 3 mm-thick CMC heat shield will now be analyzed through a static structural analysis. A linear buckling analysis with the maximum flight pressure was performed. As the buckling pressure of 259 kPa is much higher than the maximum flight pressure of 4.5 kPa, it is revealed that buckling is not a concern. The corresponding mode shape is given in figure 7.3.

Now, the stress analysis will be performed. Three cases will be analyzed, which are shown in table 7.7. The first case shows the stresses corresponding to the maximum flight pressure alone. The second case brings the temperatures corresponding to the time of maximum flight pressure, and the third case is when the wall temperature is at its peak with the corresponding pressure applied.

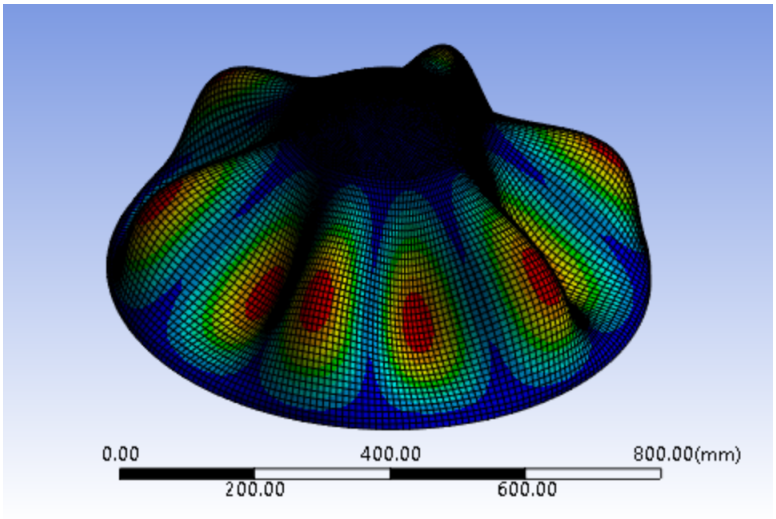

Figure 7.3: Heat shield first buckling mode.

Case	Pressure [kPa]	T_w [K]	$T_{i1}[K]$
Maximum Pressure only	4.5	-	-
Max Pressure with Temperature	4.5	2024.0	2036.4
Max Temperature with Pressure	4.0	2105.0	2078.1

Table 7.7: Loads for structural analysis cases for a 45° aeroshell with a C/C-SiC XB skin.

Material stresses form the criteria for analysis. The maximum stress values of C/C-SiC XB are given in table 7.8, which generally do not change with temperature.

Tensile [MPa]	Compressive [MPa]	Flexural [MPa]
80	210	160

Table 7.8: Maximum stress values for C/C-SiC XB

The inputs from table 7.7 are applied and the elemental stresses are evaluated. For brevity, only the stresses with the largest magnitudes and the minimum margin of safety are shown in table 7.9. Negative stress values are compressive and positive stress values are tensile. Positive values of radial and vertical displacement correspond to outward expansion and vertical stretching respectively. The margin of safety is calculated using equation 5.7 using a stress safety factor of 1.25.

Property	Pressure Only	Max Pressure, Combined	Max Temperature, Combined
Hoop Stress [MPa]	-0.76	-63.51	-65.72
Meridional Stress [MPa]	-0.38	-0.82	-0.79
Bending (Hoop) [MPa]	-0.07	-3.94	-3.19
Bending (Meridional) [MPa]	-1.89	-42.11	-42.80
Radial Displacement [mm]	0.00	0.50	0.52
Vertical Displacement [mm]	-0.01	0.77	0.79
Minimum MoS	66.82	1.65	1.56

Table 7.9: Maximum stresses of the 45° CMC heat shield with minimum margins of safety.

From table 7.9, it is shown that thermal stresses are a larger cause for concern compared to mechanical stresses. The minimum margin of safety for pressure loads alone is given by bending in the meridional direction, while compressive hoop stresses are the highest if thermal stresses are considered. The case where the maximum wall temperature is encountered is the worst case compared. As its MoS is 1.56, the analyses showed that the design can withstand the combined thermomechanical loads.

High compressive stresses in the hoop direction were expected. As the heat shield is a shell of revolution constrained at the open end, thermal expansion in the hoop direction is restricted, especially near the end. Due to the simply supported boundary constraint, the heat shield is not free to expand within this vicinity, resulting in high compression. As there is virtually no hoop displacement, the hoop stresses are higher compared to the meridional stresses. Figure 7.4a shows the hoop stress distribution, with a small area of high compressive stress near the end, while most of the shell shows much smaller tensile stresses within 5 MPa. The bending stresses, as shown in figure 7.4b for the meridional component, show similar behavior, but rapidly drop to zero near the boundary. The vertical displacement distribution, which is highest at the spherical nose, is shown in figure 7.5a. Starting from the spherical nose, the radial expansion gradually gets larger along the generator of the heat shield and drops to zero near the edge. This is shown in figure 7.5b. It can be seen that the bending stresses are predominantly responsible for the radial expansion behavior. The area where the highest compressive bending stress begins is where the highest radial expansion ends. The stress and displacement behaviors are similar for all thermomechanical cases analyzed in this chapter.

As the high stresses are largely a thermal contribution, the stress results are possibly conservative compared to a more realistic case with a surface temperature distribution. In this case, the stress values might be lower as temperatures encountered in this region may be lower compared to the stagnation point temperature at the nose. However, given that it is located at the heat shield's shoulder, the local temperatures encountered might be higher than those

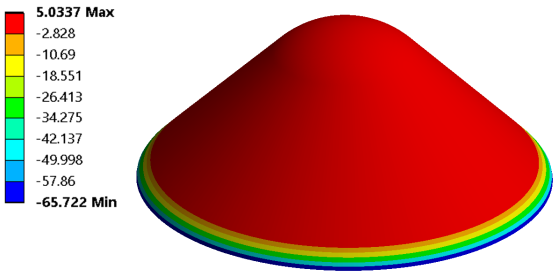

(a) Hoop stresses on the 45° CMC heat shield.

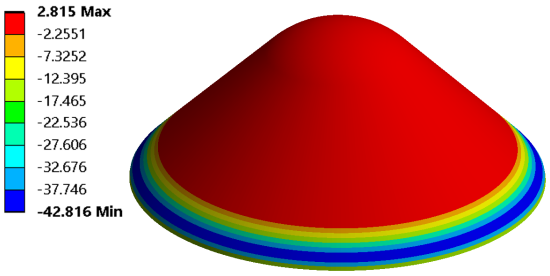

(b) Meridional bending stresses on the 45° CMC heat shield.

Figure 7.4: Distribution of critical stress components (in MPa) of the 45° CMC heat shield.

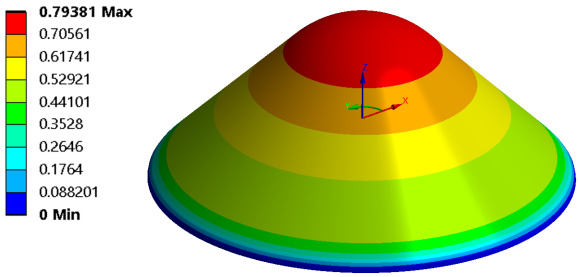

(a) Vertical displacement on the 45° CMC heat shield.

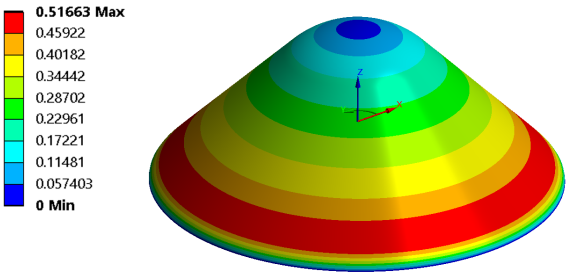

(b) Radial displacement on the 45° CMC heat shield.

Figure 7.5: Displacement distributions (in mm) on the 45° CMC heat shield.

experienced at the conical section. A more accurate stress distribution results from a proper temperature map; this is only known if a higher-fidelity distribution of heat fluxes along vehicle is obtained.

7.3. UHTCMC Skin

The sizing process is repeated for a TPS with a UHTCMC skin; due to its superior temperature limit, the process was much less rigorous compared to that with the CMC skin. The final thicknesses of layers and areal densities for both the CMC and UHTCMC skin are given in table 7.10.

Material	Skin Thickness [mm]	RS-ZFELT Thickness [mm]	Q-Fiber Thickness [mm]	Areal Density [kg/m^2]
CMC	3.0	8.0	26.0	9.0
UHTCMC	2.0	8.5	26.0	10.5

Table 7.10: Comparison of TPS thicknesses and areal density with different skin materials.

It is observed that the TPS with the UHTCMC skin reduced the system thickness by only 1.5 mm compared to the CMC TPS. Despite the thinner skin layer, the UHTCMC TPS is 16% heavier as the material is almost twice as dense as the CMC. The maximum temperatures in both systems are shown in table 7.11, and the temperature history of the UHTCMC TPS in figure 7.6.

Description	T_w [K]	T_{i1} [K]	T_{i2} [K]	T_b [K]
CMC TPS	2105.0	2083.1	1532.3	443.0
UHTCMC TPS	2129.0	2125.1	1531.8	445.6

Table 7.11: Maximum TPS temperature comparison with different skin materials.

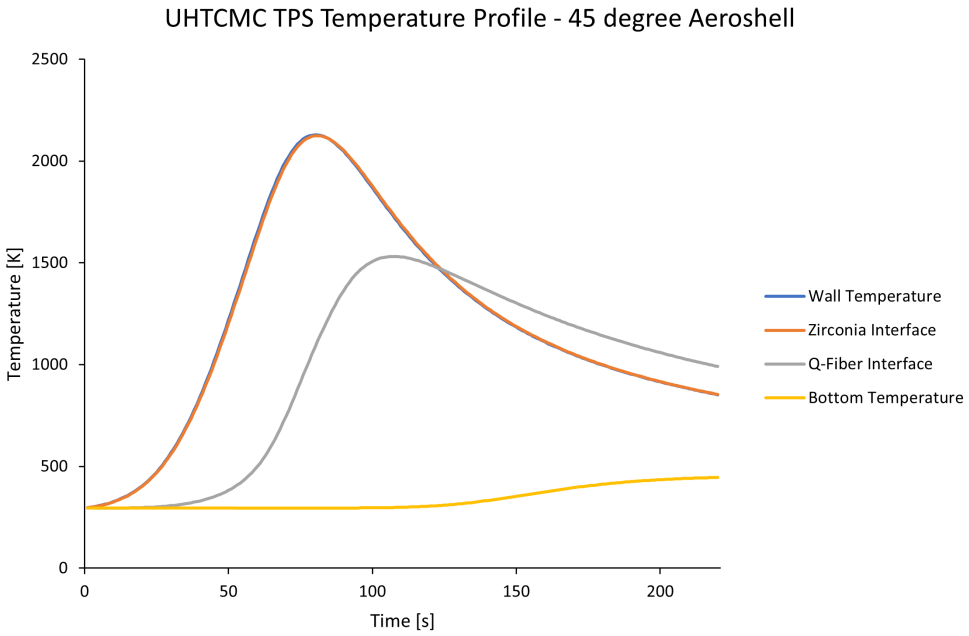

Figure 7.6: Temperature history of the UHTCMC TPS on the 45° heat shield.

The temperature difference between the wall and skin interface is very narrow as the UHTCMC material has a much higher thermal conductivity. This can also be seen in the time difference in maximum temperatures of the wall and skin interface between both systems. It takes 2 seconds for the CMC TPS and 1 second for the UHTCMC TPS after the peak wall temperature for the interface to reach its peak temperature.

The 2 mm-thick UHTCMC skin has a critical buckling load of 240.8 kPa. The limit stresses above 2073 K for C/C-ZrB_2-SiC are given in table 7.12, and the maximum stresses in table 7.14. As shown in earlier results, the structural loads alone dwarf in comparison to combined loads, so only the combined thermostructural cases are shown. Table 7.13 shows the surface temperatures and pressures for the cases.

Tensile [MPa]	Compressive [MPa]	Flexural [MPa]
100	500	315

Table 7.12: Maximum stress values for C/C-ZrB_2-SiC

Case	Pressure [kPa]	T_w [K]	$T_{i1}[K]$
Max Pressure with Temperature	4.5	2068.8	2072.4
Max Temperature with Pressure	4.0	2129.0	2124.4

Table 7.13: Loads for structural analysis cases for a 45° UHTCMC heat shield.

Property	At Max Pressure	At Max Temperature
Hoop Stress [MPa]	-311.95	-321.79
Meridional Stress [MPa]	-1.90	-1.89
Bending (Hoop) [MPa]	-15.19	-14.75
Bending (Meridional) [MPa]	-206.39	-211.89
Radial Displacement [mm]	1.12	1.15
Vertical Displacement [mm]	1.62	1.67
Minimum MoS	0.22	0.19

Table 7.14: Maximum stresses of the 45° UHTCMC heat shield with minimum margins of safety.

The minimum margin of safety, corresponding to bending in the meridional direction, is much lower compared to the CMC TPS. Throughout the investigation carried out in the sizing process, it was discovered that increasing the skin thickness has little effect on mitigating thermal-induced stresses. The higher thermal stresses than the CMC system can be explained not only due to a higher maximum temperature of over 100 K, but also a higher thermal expansion coefficient of the material. A lower MoS is again given by the maximum temperature case. As the margin of safety is positive, the design meets requirements.

7.4. 70° Heat Shield

Finally, the TPS with both materials will be assessed for the 70° aeroshell. Following the sizing methods of the TPS in the previous sections, the final thicknesses and areal densities for the 70° aeroshell using both materials are shown in table 7.15, and the maximum temperatures in table 7.16. The temperature histories for the CMC and UHTCMC TPS are given in figures 7.7 and 7.8 respectively. The heat shield mass constraint of this vehicle based on section 5.1 is 6.5 kg. Given that its surface area is much smaller than the 45° heat shield, the areal density requirement is less restrictive. Having increased by a factor of 2, the maximum areal density of the TPS is now 22.4 kg/m^2.

Material	Skin Thickness [mm]	RS-ZFELT Thickness [mm]	Q-Fiber Thickness [mm]	Areal Density [kg/m^2]
CMC	3.0	9.0	26.0	9.3
UHTCMC	2.0	9.5	25.5	10.7

Table 7.15: Comparison of TPS thicknesses and areal density with different skin materials for the 70° heat shield.

The UHTCMC TPS reduced the system thickness by only 1 mm and is 15% heavier compared to the CMC TPS. The maximum layer temperatures are given for both systems on the 70° aeroshell in table 7.16.

Description	T_w [K]	T_{i1} [K]	T_{i2} [K]	T_b [K]
CMC TPS	2178.0	2154.4	1502.6	441.8
UHTCMC TPS	2204.3	2199.9	1501.7	449.1

Table 7.16: Maximum TPS temperature comparison with different skin materials for the 70° heat shield.

As in the case of the first heat shield, pressure buckling was not found to be an issue as the linear buckling loads for the CMC and UHTCMC heat shields are 255 and 227 kPa respectively, which are well above the flight loads. The results of the thermostructural stress analysis of the 70° for the CMC and UHTCMC skin are given in tables 7.17 and 7.18 respectively.

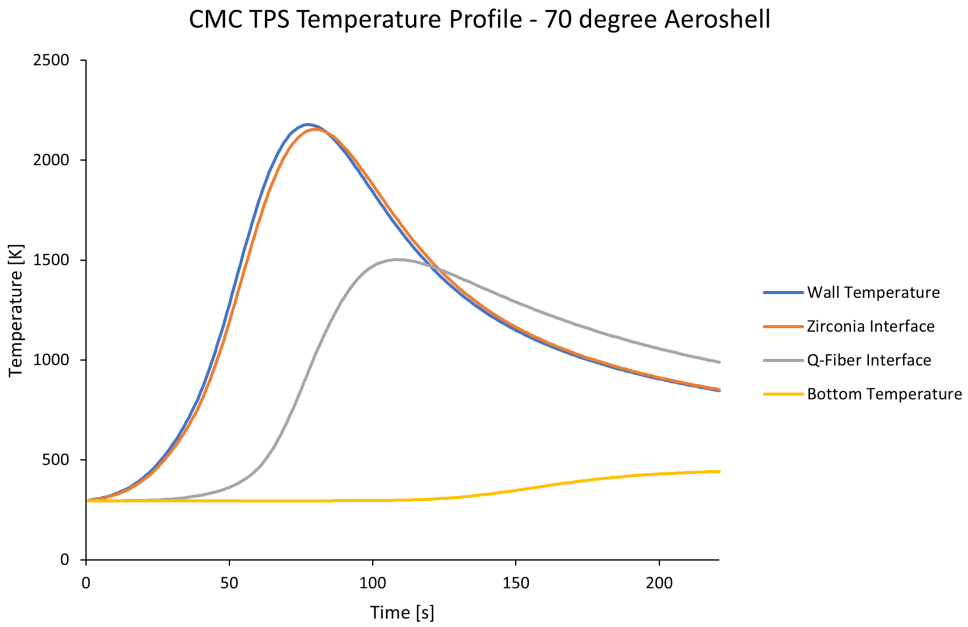

Figure 7.7: Temperature history of the CMC TPS on the 70° heat shield.

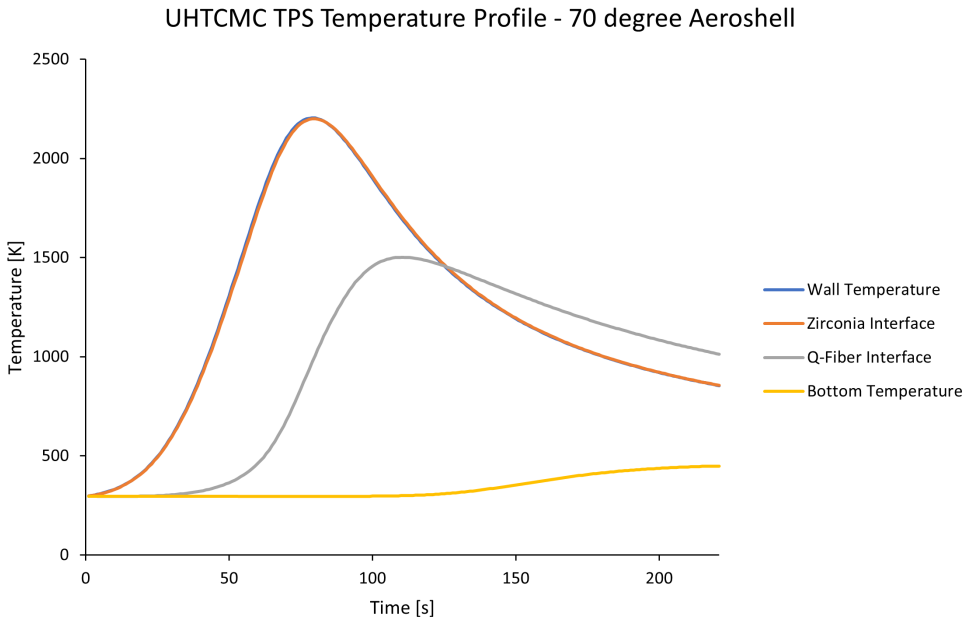

Figure 7.8: Temperature history of the UHTCMC TPS on the 70° heat shield.

Compared to the 45° heat shield, the tensile stresses of the CMC TPS in the second vehicle are less, while the compressive stresses are comparable. The compressive bending stresses have increased by approximately 2 MPa in the hoop direction but decreased slightly in the meridional direction. The average displacements are smaller by approximately 0.1 mm in the 70° heat shield. The minimum MoS value also corresponds to in-plane hoop compression in the maximum temperature case. The value for the 70° vehicle, however, is higher at 1.69, compared to 1.56 for the 45° vehicle.

Property	At Max Pressure	At Max Temperature
Hoop Stress [MPa]	-60.02	-62.37
Meridional Stress [MPa]	-0.92	-0.83
Bending (Hoop) [MPa]	-6.00	-5.25
Bending (Meridional) [MPa]	-40.86	-40.57
Radial Displacement [mm]	0.36	0.37
Vertical Displacement [mm]	0.64	0.67
Minimum MoS	1.80	1.69

Table 7.17: Maximum stresses of the 70° CMC heat shield with minimum margins of safety.

Property	At Max Pressure	At Max Temperature
Hoop Stress [MPa]	-294.28	-304.67
Meridional Stress [MPa]	3.09	3.49
Bending (Hoop) [MPa]	-22.51	-22.23
Bending (Meridional) [MPa]	-189.88	-193.29
Radial Displacement [mm]	0.81	0.84
Vertical Displacement [mm]	1.27	1.31
Minimum MoS	0.33	0.30

Table 7.18: Maximum stresses of the 70° UHTCMC heat shield with minimum margins of safety.

The UHTCMC TPS shows a larger change in compression compared to the CMC TPS, increasing by approximately 20 MPa on the 70° heat shield. The tensile stresses change to a much smaller extent, but in the meridional component, compressive stresses slightly dominate while on the 70° vehicle, tensile stresses are larger in magnitude. Consequently, the compressive bending stress in the hoop direction increased over 7 MPa, while the compressive meridional bending stresses decreased over 20 MPa. The vertical displacements have decreased by approximately 0.3 mm, and about 0.4 mm in the radial direction compared to its counterpart on the 45° heat shield. The lowest MoS value at 0.3 also corresponds to bending in the meridional direction, approximately higher by 0.1 than the lowest MoS value of the 45° vehicle.

The parametric studies performed in this section show the importance of synergy between thermal and structural modeling. While the pressure loads are also important to consider in the design of a hot structure, the thermal loads are much more critical, exerting large compressive stresses. The largest compressive stresses are seen in the in-plane hoop direction for the CMC TPS, while compressive stresses due to bending in the meridional direction are highest for the UHTCMC TPS. It was shown that the most critical design case for static analyses is at the point of maximum temperatures, and the most demanding cases take place within the high-temperature regime.

For both heat shield configurations, the CMC skin clearly shows superior performance compared to the UHTCMC skin with regard to mass savings and stress margin of safety. For both skin materials, the minimum stress margin of safety for the 70° configuration is higher by 0.1 than the 45° configuration.

The 70° heat shield is exposed to noticeably higher heat fluxes than its 45° counterpart, resulting in exposure to higher temperatures. The 70° CMC heat shield experiences maximum temperatures beyond the active oxidation point of 1923 K for approximately 33 seconds, reaching a peak temperature of 2178 K. Meanwhile, the 45° CMC heat shield experiences active oxidation temperatures for approximately 28 seconds, with a peak temperature of 2105 K. The difference in active oxidation limit duration between the two configurations is considered small. While the maximum temperature of the 70° heat shield is higher by 73 K, it is still within the acceptable limit considered for a short and single-use application discussed in chapter 5.

Considering that temperature requirements are met, it can be concluded from the simulations that the 70° configuration is preferable to a 45° heat shield. The 70° heat shield does not only show superior mechanical performance, but its total mass is lighter than the 45° heat shield by a factor of approximately 2.4. Despite a slightly higher areal density, this is due to the higher heat shield surface area of the 45° heat shield.

A summary of the results is shown in table 7.19, and the final heat shield masses and TPS thicknesses for both vehicles are visually compared as bar charts in figures 7.9 and 7.10 respectively.

System	T_w Max [K]	MoS Min	Total Thickness [mm]	Areal Density [kg/m^2]	Heat Shield Mass [kg]
CMC, 45°	2105.0	1.6	37.0	9.1	6.5
CMC, 70°	2178.0	1.7	38.0	9.3	2.7
UHTCMC, 45°	2129.0	0.2	36.5	10.5	7.5
UHTCMC, 70°	2204.3	0.3	37.0	10.7	3.1

Table 7.19: Comparison of maximum temperatures, minimum margin of safety, and masses for different heat shields with different skin materials.

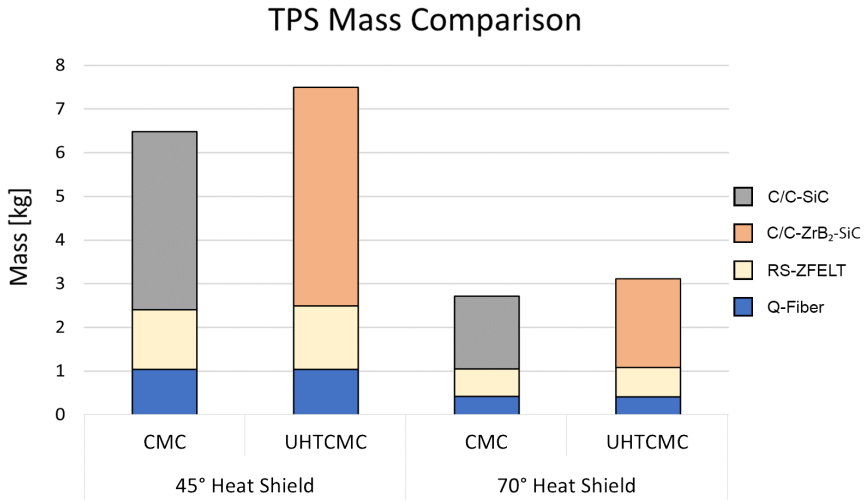

Figure 7.9: Total and layer mass comparison of the CMC and UHTCMC-based TPS on the two aeroshells.

It must be noted that a 70° heat shield is considered obsolete for the MDM EDV due to aerodynamic stability considerations and a 45° heat shield is the currently proposed solution within

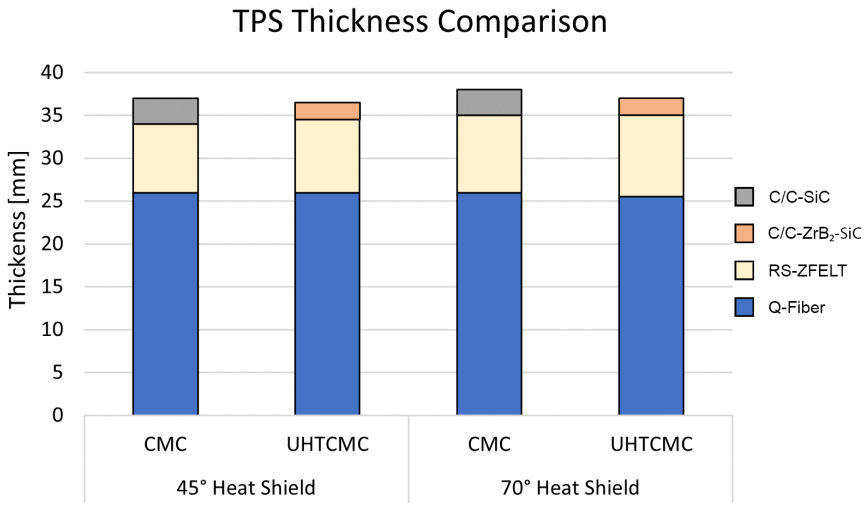

Figure 7.10: Thickness performance comparison of the CMC and UHTCMC-based TPS on the two aeroshells.

Team Tumbleweed. The 45° value, however, is not yet set in stone and still remains open considering that no CFD simulations have been performed. A compromise between heat shield thermostructural performance and other vehicle subsystem performances beyond the scope of this work such as aerodynamic stability is critical. A maximum vertex angle must also be set. A maximum value of 60° is suggested; this was used on Beagle 2, which spanned less than 1 meter in base diameter and used nothing else but spin stabilization provided by the Mars Express orbiter [132].

8

Conclusions and Recommendations

This chapter summarizes the results of this thesis by answering the research questions that were posed in chapter 1. The report closes with recommendations to implement in future work based on the assumptions made and insights gained throughout the duration of this work.

8.1. Addressing Research Questions

Answers are given in this section to each sub question to address the primary research question:

How can a lightweight heat shield combining high thermal and mechanical performance be designed for a small Mars entry capsule using ceramic matrix composites?

Q1: What CMC TPS design concept is suitable for a low-mass Mars mission?

A lightweight system is required for the entry and descent vehicle of Team Tumbleweed's Mars Demonstrator Mission, which aims to test a wind-driven rover on the Martian surface, including its descent. If utilizing novel TPS methods, it is recommended that the system shows versatility for a range of Mars missions without affecting the rover's descent performance. The monolithic hot structure aeroshell concept was selected. As this question can be highly mission-specific, a systems engineering approach was implemented to answer this question. First, CMC TPS concepts were identified based on heritage methods and past proposals for Mars entry. The concepts that were assessed are:

- **Monolithic hot structure:** A single-piece load-bearing CMC shell with an internal layer of lightweight insulation.
- **Deployable decelerator:** A circular arrangement of stowed CMC panels around a central front shield that are unfolded for entry.
- **Monolithic shell over an insulated structure:** This method employs a hot and cold structure combination, where a layer of insulation is sandwiched between a single-piece external CMC shell and a substructure. Adhesive bonding or mechanical fasteners can be used to keep the CMC shell intact.
- **Shingles over an insulated structure:** CMC tiles are used instead of a shell; joining to the substructure is only possible through mechanical fastening.
- **Surface-Protected Ablator:** A CMC shell bonded over an ablator, bonded over a substructure.

The decelerator concept was eliminated due to its complexity and unsuitability for the mission. A strength-and-weakness analysis was performed on the remaining concepts to narrow the selection to two concepts. The monolithic hot structure and the surface-protected ablator were the two concepts selected for a graphical tradeoff due to their minimal weight potential and mission suitability. The tradeoff showed that the monolithic aeroshell is a compromising solution between weight and mission goals.

The defined hot structure heat shield consists of a thin external CMC shell backed by an internal insulation package consisting of zirconia-based insulation for the high-temperature region through the thickness, and silica-based insulation for milder temperatures.

Q2: How do changes in vehicle dimensional parameters affect the design of the heat shield?

TPS design is significantly influenced by its requirements and vehicle thermomechanical loads. In chapter 4, the mechanical and thermal loads were investigated through a 2D trajectory simulation. The original dimensions of the sphere-cone heat shield before the start of the project were based on a half-cone vertex angle of 70°. For reasons attributed to aerodynamic stability, this value was later disregarded by Team Tumbleweed, proposing a change to 45°. A comparison was therefore made in this work between heat shields of 70° and 45° configurations. Such dimensional changes strongly affect a vehicle's ballistic coefficient, and consequently, entry load environment.

If a vehicle's ballistic coefficient is not constrained as the vehicle's vertex angle decreases:

- The heat flux profile can increase significantly due to a large increase in ballistic coefficient.
- The mechanical loads do not change much.
- The altitude of peak deceleration noticeably decreases

As it is desired to decrease heat flux and increase peak deceleration altitude, the ballistic coefficient must be restricted.

With an unchanged ballistic coefficient and a slight increase in vehicle diameter and nose radius:

- Lowering the drag coefficient via the heat shield's vertex angle does not change the mechanical loads.
- The altitudes of maximum deceleration and heating remain unchanged.
- The heat fluxes are much smaller.

Within a limited range of diameters, increasing the heat shield's vertex angle will cause the heat shield's surface area to significantly increase. Therefore, a 45° heat shield will be heavier than a 70° heat shield with a similar diameter. This places a more restrictive constraint on TPS areal density.

A configuration for the 45° heat shield was therefore selected in such a way that shows a good compromise between required mass, vehicle diameter, and ballistic coefficient.

- The total vehicle mass was increased from the current 18.2 kg mass up to the required limit of 20 kg to allow a larger heat shield mass.

- The vehicle diameter was also increased from 0.6 m to 0.8 m to not only minimize the ballistic coefficient but also allow a larger payload volume.

The resulting ballistic coefficient increased by 2 kg/m^2 compared to the 45° heat shield with the original vehicle mass and diameter, but the changes in load history and their corresponding altitudes are small.

Regardless, the TPS sizing challenge of strategically allocating appropriate thicknesses to different layers while ensuring the satisfaction of design stresses and mass requirements is less noticeable for the 70° despite a larger heat flux. The sized results show similar TPS areal densities, but due to the larger surface area of the 45° configuration, its resulting mass is over 2.4 times heavier than the 70° heat shield. While the minimum stress margin of safety of the 70° configuration is larger by only 0.1, it can be used to show that it displays superior (thermo)mechanical performance compared to its 45° counterpart.

Q3: How does a traditional CMC and a UHTCMC compare with respect to the thermostructural performance of the heat shield while satisfying mass requirements?

UHTCMC materials are of high interest for hot structure and TPS applications due to their superior oxidation resistance compared to traditional CMCs, thus raising the maximum operational temperature of a TPS. A sized system using a CMC and a UHTCMC skin material was therefore compared for the 45° and 70° heat shields. For both heat shield sizes analyzed, a system using C/C-SiC, a baseline CMC material, shows superior performance compared to that utilizing a C/C-ZrB_2-SiC UHTCMC. While thicker than the UHTCMC TPS by 1.5 mm and 1 mm for a 45° and 70° vehicle respectively, it saves mass by over 15%. This is due to the larger matrix density of the UHTCMC material. In addition, the minimum margin of safety against thermal and mechanical stresses is increased by approximately 1.5 for both vehicles when using a CMC skin compared to the UHTCMC. In conclusion, for a single-use mission where mass is an important constraint, traditional SiC-based CMCs are more suitable than a UHTCMC at their current state. Oxidation recession is permissible as long as the structural integrity of the system is not severely compromised. UHTCMCs are therefore more suitable for systems where continuous applications are of high importance.

Based on the work performed, the parameters of the optimal hot structure heat shield design are:

- **Half Vertex Angle:** 70°
- **Base Diameter:** 0.6 m
- **C/C-SiC Skin Thickness:** 3 mm
- **Zirconia Insulation Thickness:** 9 mm
- **Silica Insulation Thickness:** 26 mm
- **Heat Shield Mass:** 2.7 kg

8.2. Recommendations

Recommendations are made in this section based on the insights gained throughout the project.

Thermomechanical Load Distribution

Throughout this work, it was assumed that the heat flux and pressure distribution are equal throughout the vehicle profile. For a zero-angle of attack and a smaller forward spherical section, this assumption is sufficient for conceptual design as the distribution is expected to be similar throughout the cone generator. While this assumption may lead to conservative estimates for the thermal analysis and bending loads, it does not account for the temperature gradients that are encountered along the vehicle, which will introduce further in-plane stresses. A computational fluid dynamics (CFD) analysis can be performed, and it is suggested once the backshell geometry is known. Currently, the MDM backshell has not yet been defined. Alternatively, Newtonian flow theory can be assumed to get first estimates of the pressure and heat flux distribution, and interpolation methods to obtain the distribution in other phases of the flight. CFD analysis can also be used to better characterize the varying drag coefficient throughout different phases of the entry process to understand the change in pressure loads throughout the flight.

Stronger Thermomechanical Model Coupling

Because the temperatures are assumed constant throughout the profile of the vehicle, the thermostructural analysis was made by placing a constant temperature over the top and bottom surfaces of the heat shield shell for computational efficiency. This cannot be done in models with varying temperature distribution, so a coupled CFD and structural analysis, or a coupled thermal and structural analysis, must be performed.

Modeling of Mechanical Constraints

At this conceptual stage of the mission design, there are still many unknowns, including the mechanism to couple and separate the heat shield from the back shell. A simply supported boundary condition is assumed throughout this work, but newer boundary conditions must be implemented into the model if these mechanisms are defined.

Ablation and Emissivity

No ablation or recession was modeled in this work, which may affect the sizing and thermomechanical properties of the CMC TPS in particular. It was also assumed that the emissivity is constant - the formation of different phases as the CMC oxidizes at different temperatures can lead to a sudden change in emissivity values. Furthermore, ablative solutions are currently used for Mars entry missions exclusively; if ablation is modeled, a comparison to a standard ablative structure must be made.

Definition of Insulation Attachment

In this project, only consideration was made to the attachment of the insulation layer to the skin as an adhesively bonded quilted package. This idea was not explored further; it is recommended to attempt this addition to the thermal model, and possibly the effects of an adhesive on the structural model.

Dynamic Analysis

Static analyses were performed in this work with pressure applied onto the structure, and separate cases had to be analyzed. However, the thermomechanical environment throughout the

entire duration of entry can be modeled through a dynamic analysis. In addition, rapidly varying aerodynamic pressure is better captured as an inertial load. A coupled dynamic structural analysis with thermal loads is recommended.

Manufacture and Test
The thermal and thermostructural analyses were only performed through numerical simulations in this work. Experimental validation of the TPS stack in a plasma arc jet environment is recommended, and if possible, the manufacture of a smaller-scale representative prototype of the heat shield.

Stronger Integration with Mission Architecture
In this work, design parameters of the EDV such as base diameter and entry mass were changed. As the MDM is still in its preliminary phase, a number of aspects remain unknown or undefined; no clear boundaries have been set for many parameters. Changing high-level system parameters such as vehicle base diameter, for example, while beneficial for entry, can lead to complications and consequences for other subsystems, such as aerodynamics and mission cost. As work continues on the MDM, TPS and EDV design must be strongly embedded into the holistic mission architecture and coupled with all considered disciplines.

The outcome of this work makes a strong case for the mission integration problem. A 70° heat shield is favored over a 45° heat shield with respect to thermal and structural performance, especially if other dimensions remain unchanged. As a 70° half angle is no longer relevant for Team Tumbleweed and no official limit has been set for this parameter, it is highly suggested to identify a compromise between thermostructural performance and aspects related to other subsystems. Based on the Beagle 2 mission, a maximum vertex angle of 60° is suggested for future work.

Bibliography

[1] Thomas K Percy et al. “Human Mars Entry, Descent, and Landing Architecture Study: Descent Systems”. In: *2018 AIAA SPACE and Astronautics Forum and Exposition*. 2018, p. 5193.

[2] Stephen Hughes et al. “Hypersonic inflatable aerodynamic decelerator (HIAD) technology development overview”. In: *21st AIAA Aerodynamic Decelerator Systems Technology Conference and Seminar*. 2011, p. 2524.

[3] Alan Cassell et al. “ADEPT, A Mechanically Deployable Re-Entry Vehicle System, Enabling Interplanetary CubeSat and Small Satellite Missions”. In: (2018).

[4] Sarah Langston et al. “Optimization of a hot structure aeroshell and nose cap for mars atmospheric entry”. In: *AIAA SPACE 2016*. 2016, p. 5594.

[5] Sophie Förste et al. “Development of a Deployable Decelerator Concept for Small Mars Landers”. In: *2nd International Conference on Flight Vehicles, Aerothermodynamics and Re-entry Missions Engineering*. 2022.

[6] Donald M. Curry. *Space Shuttle Orbiter thermal protection system design and flight experience*. July 1993.

[7] François Buffenoir et al. “Development and flight qualification of the C–SiC thermal protection systems for the IXV”. In: *Acta Astronautica* 124 (2016). Intermediate Experimental Vehicle (IXV) – Special Publications from the 6th EUCASS, pp. 85–89. ISSN: 0094-5765. DOI: https://doi.org/10.1016/j.actaastro.2016.02.010. URL: https://www.sciencedirect.com/science/article/pii/S0094576516000576.

[8] Diletta Sciti et al. “Introduction to H2020 project C3HARME–next generation ceramic composites for combustion harsh environment and space”. In: *Advances in applied ceramics* 117.1_suppl (2018), pp. 70–75.

[9] David E. Glass. *Ceramic Matrix Composite (CMC) Thermal Protection Systems (TPS) and Hot Structures for Hypersonic Vehicles*. 2008.

[10] JC Verneuil and Jean-Francois Puech. “Scale Reduction Methodology for Space Probe Aeroshell Testing”. In: *SAE transactions* (1995), pp. 787–792.

[11] Michelle M Munk and Steven A Moon. “Aerocapture technology development overview”. In: *2008 IEEE Aerospace Conference*. IEEE. 2008, pp. 1–7.

[12] Sandra P Walker et al. “A Multifunctional Hot Structure Heat Shield Concept for Planetary Entry”. In: *20th AIAA International Space Planes and Hypersonic Systems and Technologies Conference*. 2015, p. 3530.

[13] Erik Seedhouse. “Starship”. In: *SpaceX: Starship to Mars – The First 20 Years*. Cham: Springer International Publishing, 2022, pp. 171–188. ISBN: 978-3-030-99181-4. DOI: 10.1007/978-3-030-99181-4_9. URL: https://doi.org/10.1007/978-3-030-99181-4_9.

[14] Lucas Cohen et al. “Pre-Phase A study of an innovative, low-cost Demonstration Mission of Tumbleweed mobile impactors on Mars”. In: *74th International Astronautical Congress, Baku, Azerbaijan*. 2023.

[15] J Rothenbuchner et al. “The tumbleweed mission: Enabling novel mars data sets through low-cost rover swarms, iac-22, a3, ip, x72458”. In: *73rd International Astronautical Congress (IAC), Paris, France*. 2022, pp. 18–22.

[16] Andrew Ball et al. *Planetary landers and entry probes*. Cambridge University Press, 2007.

[17] Grant Palmer et al. “Modeling Heat-Shield Erosion due to Dust Particle Impacts for Martian Entries”. In: *Journal of Spacecraft and Rockets* 57.5 (2020), pp. 857–875.

[18] Kayla Parcero et al. *Planetary Mission Entry Vehicles Quick Reference Guide Version 4.0*. 2022.

[19] Karl T Edquist et al. “Mars science laboratory entry capsule aerothermodynamics and thermal protection system”. In: *2007 IEEE Aerospace Conference*. IEEE. 2007, pp. 1–13.

[20] Prasun N. Desai et al. “Entry, Descent, and Landing Performance of the Mars Phoenix Lander”. In: *Journal of Spacecraft and Rockets* 48.5 (2011), pp. 798–808. DOI: 10.2514/1.48239. eprint: https://doi.org/10.2514/1.48239. URL: https://doi.org/10.2514/1.48239.

[21] Ashley M Korzun et al. “Aerodynamic performance of the 2018 InSight Mars lander”. In: *AIAA Scitech 2020 Forum*. 2020, p. 1272.

[22] Robin Beck et al. “Development of the Mars Science Laboratory Heatshield Thermal Protection System”. In: *Journal of Spacecraft and Rockets* 51.4 (2014), pp. 1139–1150.

[23] Christopher D Karlgaard et al. “Mars InSight entry, descent, and landing trajectory and atmosphere reconstruction”. In: *Journal of Spacecraft and Rockets* 58.3 (2021), pp. 865–878.

[24] Christopher D. Karlgaard et al. “Mars Entry, Descent, and Landing Instrumentation 2 Trajectory, Aerodynamics, and Atmosphere Reconstruction”. In: *Journal of Spacecraft and Rockets* 0.0 (2021), pp. 1–16. DOI: 10.2514/1.A35440. eprint: https://doi.org/10.2514/1.A35440. URL: https://doi.org/10.2514/1.A35440.

[25] Haogong Wei et al. “Tianwen-1 Mars entry vehicle trajectory and atmosphere reconstruction preliminary analysis”. In: *Astrodynamics* 6.1 (2022), pp. 81–91. DOI: 10.1007/s42064-021-0116-y. URL: https://www.sciopen.com/article/10.1007/s42064-021-0116-y.

[26] Qi Li et al. “Aerodynamic design, analysis, and validation techniques for the Tianwen-1 entry module”. In: *Astrodynamics* 6 (2022), pp. 39–52.

[27] Obinna Uyanna and Hamidreza Najafi. “Thermal protection systems for space vehicles: A review on technology development, current challenges and future prospects”. In: *Acta Astronautica* 176 (2020), pp. 341–356.

[28] Joseph H. Koo and Jon Langston. “Chapter 12 - Polymer Nanocomposite Ablative Technologies for Solid Rocket Motors”. In: *Nanomaterials in Rocket Propulsion Systems*. Ed. by Qi-Long Yan et al. Micro and Nano Technologies. Elsevier, 2019, pp. 423–493. ISBN: 978-0-12-813908-0. DOI: https://doi.org/10.1016/B978-0-12-813908-0.00012-5. URL: https://www.sciencedirect.com/science/article/pii/B9780128139080000125.

[29] Christine Szalai, Eric Slimko, and Pamela Hoffman. “Mars Science Laboratory Heatshield Development, Implementation, and Lessons Learned”. In: *Journal of Spacecraft and Rockets* 51.4 (2014), pp. 1167–1173. DOI: 10.2514/1.A32673. eprint: https://doi.org/10.2514/1.A32673. URL: https://doi.org/10.2514/1.A32673.

[30] Karl T Edquist et al. “Mars science laboratory heat shield aerothermodynamics: Design and reconstruction”. In: *Journal of Spacecraft and Rockets* 51.4 (2014), pp. 1106–1124.

[31] David M Driver et al. “Arcjet testing in shear environment for Mars Science Laboratory thermal protection system”. In: *Journal of Spacecraft and Rockets* 51.4 (2014), pp. 1151–1166.

[32] *Heat shield construction for NASA’s Insight Mission – NASA’s Insight Mars Lander*. URL: https://mars.nasa.gov/resources/7220/heat-shield-construction-for-nasas-insight-mission/?site=insight.

[33] Adam Nelessen et al. “Mars 2020 entry, descent, and landing system overview”. In: *2019 IEEE Aerospace Conference*. IEEE. 2019, pp. 1–20.

[34] Robin Beck et al. *TPS and Entry System Technologies for Future Mars and Titan Exploration*. 2020.

[35] *Large heat shield for mars science laboratory – NASA’s Insight Mars Lander*. URL: https://mars.nasa.gov/resources/536/large-heat-shield-for-mars-science-laboratory/?site=insight.

[36] Michael May, Deepak Rupakula, and Pascal Matura. “Non-polymer-matrix composite materials for space applications”. In: *Composites Part C: Open Access* 3 (Nov. 2020). DOI: 10.1016/j.jcomc.2020.100057.

[37] Walter Krenkel. *Ceramic matrix composites: fiber reinforced ceramics and their applications*. John Wiley & Sons, 2008.

[38] Dewei Ni et al. “Advances in ultra-high temperature ceramics, composites, and coatings”. In: *Journal of Advanced Ceramics* 11 (2022), pp. 1–56.

[39] ECSS. *ECSS-E-HB-32-20 Part 6A – Structural materials handbook: Fracture and material modelling, case studies and design and integrity control and inspection*. Mar. 2011.

[40] U Trabandt et al. “Test results of low cost C/SiC for martian entry and reusable launcher”. In: *Space Technology* 5.17 (1997), pp. 281–291.

[41] George Karadimas and Konstantinos Salonitis. “Ceramic matrix composites for aero engine applications—a review”. In: *Applied Sciences* 13.5 (2023), p. 3017.

[42] Walter Krenkel et al. “Design, Manufacture and Quality Assurance of C/C-SiC Composites for Space Transportation Systems”. In: *28th International Conference on Advanced Ceramics and Composites B: Ceramic Engineering and Science Proceedings*. Vol. 25. Wiley Online Library. 2004, pp. 49–58.

[43] Thomas Reimer. “Thermal and mechanical design of the expert C/C-SiC nose”. In: *Thermal Protection Systems and Hot Structures (5th European Workshop)*. 2006.

[44] Hannah Boehrk, Hendrik Weihs, and Henning Elsäßer. “Hot structure flight data of a faceted atmospheric reentry thermal protection system”. In: *International Journal of Aerospace Engineering* 2019 (2019), pp. 1–16.

[45] Miguel Rodríguez-Segade, Santiago Hernández, and Jacobo Díaz. “Multi-bubble scheme and structural analysis of a hypersonic stratospheric flight vehicle”. In: *Aerospace Science and Technology* 124 (2022), p. 107514.

[46] Bernhard Heidenreich. “C/SiC and C/C-SiC Composites”. In: *Ceramic matrix composites: materials, modeling and technology* (2014), pp. 147–216.

[47] Jon Binner et al. “Selection, processing, properties and applications of ultra-high temperature ceramic matrix composites, UHTCMCs – a review”. In: *International Materials Reviews* 65.7 (2020), pp. 389–444. DOI: 10.1080/09506608.2019.1652006. URL: https://doi.org/10.1080/09506608.2019.1652006.

[48] Matthew J. Gasch, Donald T. Ellerby, and Sylvia M. Johnson. “Ultra High Temperature Ceramic Composites”. In: *Handbook of Ceramic Composites*. Ed. by Narottam P. Bansal. Boston, MA: Springer US, 2005, pp. 197–224. ISBN: 978-0-387-23986-6. DOI: 10.1007/0-387-23986-3_9. URL: https://doi.org/10.1007/0-387-23986-3_9.

[49] Diletta Sciti et al. “A systematic approach for horizontal and vertical scale up of sintered Ultra-High Temperature Ceramic Matrix Composites for aerospace–Advances and perspectives”. In: *Composites Part B: Engineering* 234 (2022), p. 109709.

[50] Laura Silvestroni et al. “Ablation behaviour of ultra-high temperature ceramic matrix composites: Role of MeSi2 addition”. In: *Journal of the European Ceramic Society* 39.9 (2019), pp. 2771–2781.

[51] Antonio Vinci et al. “Understanding the mechanical properties of novel UHTCMCs through random forest and regression tree analysis”. In: *Materials & Design* 145 (2018), pp. 97–107.

[52] Luca Zoli and Diletta Sciti. “Efficacy of a ZrB2–SiC matrix in protecting C fibres from oxidation in novel UHTCMC materials”. In: *Materials & Design* 113 (2017), pp. 207–213.

[53] Luca Zoli et al. “From outer space to inside the body: Ultra-high temperature ceramic matrix composites for biomedical applications”. In: *Journal of the European Ceramic Society* 44.2 (2024), pp. 729–737.

[54] Pietro Galizia et al. “Elevated temperature tensile and bending strength of ultra-high temperature ceramic matrix composites obtained by different processes”. In: *Journal of the European Ceramic Society* 43.11 (2023), pp. 4588–4601.

[55] Suresh Kumar et al. “C/C and C/SiC composites for aerospace applications”. In: *Aerospace Materials and Material Technologies: Volume 1: Aerospace Materials* (2017), pp. 343–369.

[56] Viktor Ivanovich Trefilov. *Ceramic-and carbon-matrix composites*. Vol. 2. Springer Science & Business Media, 2012.

[57] Anastasia Filippova. *Гравимол для «Бурана»: как делали композитное крыло для корабля [Gravimol for Buran: how a composite wing for a ship was made]*. https://strana-rosatom.ru/2022/11/14/kak-delali-kompozity-dlya-burana/. Online; accessed April 4, 2024.

[58] buran.ru. *Элементы (типы) теплозащиты ”Бурана” [Elements of the ”Buran” Thermal Protection System]*. http://www.buran.ru/htm/tersaf4.htm. Online; accessed April 4, 2024.

[59] Marc Lacoste et al. “Using C/SiC composite materials for thermal protection system for planetary entry system, behaviour in relevant environment”. In: *SAE transactions* (1995), pp. 931–938.

[60] G Reich and GEN Scoon. *Thermal environment and thermal control aspects for Mars landers*. Tech. rep. SAE Technical Paper, 1993.

[61] U Trabandt et al. “Foldable Hot Structure Aerobrake, Concept Study on Light Weight Foldable Planetary Aeroshell”. In: *Hot Structures and Thermal Protection Systems for Space Vehicles*. Vol. 521. 2003, p. 247.

[62] U Trabandt et al. “Foldable Hot Structure Stabilizer for PARES”. In: *Thermal Protection Systems and Hot Structures*. Vol. 631. 2006.

[63] NASA. *Aerocapture for Discovery Missions*. 2010.

[64] Sandra P Walker et al. “Preliminary development of a multifunctional hot structure heat shield”. In: *55th AIAA/ASMe/ASCE/AHS/SC Structures, Structural Dynamics, and Materials Conference*. 2014, p. 0350.

[65] T. Pichon et al. “CMC thermal protection system for future reusable launch vehicles: Generic shingle technological maturation and tests”. In: *Acta Astronautica* 65.1 (July 2009), pp. 165–176. DOI: 10.1016/j.actaastro.2009.01.035.

[66] Romain Bernard, Thierry Pichon, and Jacques Valverde. “From IXV to Space Rider, CMC Thermal Protection System Evolutions”. In: *Proceedings of the International Conference on Flight Vehicles, Aerothermodynamics and Re-entry Missions & Engineering (FAR2019), Monopoli, Italy*. Vol. 30. 2019.

[67] European Space Agency. *IXV is being prepared for launch*. https://www.esa.int/ESA_Multimedia/Images/2015/01/IXV_is_being_prepared_for_launch. Online; accessed April 4, 2024.

[68] Hannah Boehrk. “Material-Tailored Thermo-Mechanical Design”. In: NAVO STO. 2011.

[69] Christian Zuber et al. “Manufacturing of the CMC nose cap for the EXPERT spacecraft”. In: *Advanced Processing and Manufacturing Technologies for Structural and Multifunctional Materials IV: Ceramic Engineering and Science Proceedings* 31 (2010), pp. 59–71.

[70] Kornelia Stubicar and Thomas Reimer. “Thermo-Mechanical Design of the EXPERT Nose and Testing of the Load Introductions”. In: ESA. 2009.

[71] Chun Tang and Michael Wright. “Analysis of the forebody aeroheating environment during genesis sample return capsule reentry”. In: *45th AIAA Aerospace Sciences Meeting and Exhibit*. 2007, p. 1207.

[72] Toshiyuki Suzuki et al. “Nonablative lightweight thermal protection system for Mars Aeroflyby Sample collection mission”. In: *Acta Astronautica* 136 (2017), pp. 407–420.

[73] G Reich and G Jahn. “MIRKA Heat Shield Experiment HEATIN-Theoretical and Experimental Approach to the Surface Protected Ablator”. In: *SAE transactions* (1996), pp. 481–488.

[74] J-M Bouilly, Ludovic Dariol, and Frédéric Leleu. “Ablative thermal protections for atmospheric entry. An overview of past missions and needs for future programmes”. In: *Thermal Protection Systems and Hot Structures* 631 (2006).

[75] Thierry Pichon et al. “Integrated thermal protection systems and heat resistant structures”. In: *57th International Astronautical Congress-IAC 2006*. IAC-06-D2. 5.09. 2006.

[76] J Barcena et al. “FP7/SPACE PROJECT ‘‘HYDRA’’Hybrid Ablative Development for Re-Entry in Planetary Atmospheric Thermal Protection”. In: *7th European Workshop on TPS & Hot Structures, ESA/ESTEC*. 2013, pp. 8–10.

[77] Ulrich Trabandt et al. *CMC Large Panel TPS Applied on X-38 Nose Skirt*. Tech. rep. SAE Technical Paper, 2000.

[78] Ethiraj Venkatapathy. “Ablators-From Apollo to Future Missions to Moon, Mars and Beyond”. In: *70th International Astronautical Congress*. 2019.

[79] Sarah L Langston, Christapher G Lang, and Jamshid A Samareh. “Parametric Study of an Ablative TPS and Hot Structure Heatshield for a Mars Entry Capsule Vehicle”. In: *AIAA SPACE and Astronautics Forum and Exposition*. 2017, p. 5290.

[80] Sarah L Langston, Christopher G Lang, and Kamran Daryabeigi. “Optimization of a Multifunctional Hot Structure Aeroshell for Mars Entry”. In: (2018).

[81] Ehouarn Millour et al. “The Mars Climate Database (Version 6.1)”. In: *Europlanet Science Congress 2022*. Vol. 16. 2022, EPSC2022–786.

[82] Erwin Mooij. *Re-entry Systems*. TU Delft, 2019.

[83] Ignazio Dimino et al. “A Morphing Deployable Mechanism for Re-Entry Capsule Aeroshell”. In: *Applied Sciences* 13.5 (2023), p. 2783.

[84] Michael Wright et al. “A review of aerothermal modeling for Mars entry missions”. In: *48th AIAA Aerospace Sciences Meeting Including the New Horizons Forum and Aerospace Exposition*. 2010, p. 443.

[85] Scott K Martinelli and Robert D Braun. “Centerline heating methodology for use in preliminary design studies”. In: *2011 Aerospace Conference*. IEEE. 2011, pp. 1–18.

[86] Dean R Chapman. *An approximate analytical method for studying entry into planetary atmospheres*. US Government Printing Office, 1959.

[87] Erwin Mooij, Jean-Paul Huot, and Guillermo Ortega. “Entry trajectory simulation using ESA Mars climate database version 4.1”. In: *AIAA/AAS Astrodynamics Specialist Conference and Exhibit*. 2006, p. 6023.

[88] Kenneth Sutton and Randolph A Graves Jr. *A general stagnation-point convective heating equation for arbitrary gas mixtures*. Tech. rep. 1971.

[89] Thomas K West IV and Aaron M Brandis. “Stagnation-Point Aeroheating Correlations for Mars Entry”. In: *Journal of Spacecraft and Rockets* 57.2 (2020), pp. 319–327.

[90] RA Mitcheltree et al. “Aerodynamics of the mars microprobe entry vehicles”. In: *Journal of spacecraft and rockets* 36.3 (1999), pp. 392–398.

[91] Suzanne Smrekar et al. “Deep Space 2: the Mars microprobe mission”. In: *Journal of Geophysical Research: Planets* 104.E11 (1999), pp. 27013–27030.

[92] Dinesh Prabhu and David Saunders. “On heatshield shapes for Mars entry capsules”. In: *50th AIAA Aerospace Sciences Meeting including the New Horizons Forum and Aerospace Exposition*. 2012, p. 399.

[93] Michael Wright et al. “Defining ablative thermal protection system margins for planetary entry vehicles”. In: *42nd AIAA thermophysics conference*. 2011, p. 3757.

[94] Robert Staehle et al. “Multiplying Mars lander opportunities with MarsDROP microlanders”. In: (2015).

[95] DuPont. *KEVLAR® ARAMID FIBER TECHNICAL GUIDE*. `https://www.dupont.com/content/dam/dupont/amer/us/en/safety/public/documents/en/Kevlar_Technical_Guide_0319.pdf`. Online; accessed 13 March 2024.

[96] Jeffrey S Robinson, Kathryn E Wurster, and Janelle C Mills. “Entry trajectory and aeroheating environment definition for capsule-shaped vehicles”. In: *Journal of Spacecraft and Rockets* 46.1 (2009), pp. 74–86.

[97] Walter L Heard Jr et al. “Design, Analysis, and Tests of a Structural Prototype Viking Aeroshell”. In: *Journal of Spacecraft and Rockets* 10.1 (1973), pp. 56–65.

[98] Shengbo Shi, Cunxi Dai, and Yifan Wang. “Design and optimization of an integrated thermal protection system for space vehicles”. In: *20th AIAA international space planes and hypersonic systems and technologies conference*. 2015, p. 3553.

[99] Javad Fatemi and Louis Walpot. “Coupled Thermal-structural analysis of the EXPERT re-entry vehicle”. In: *17th AIAA International Space Planes and Hypersonic Systems and Technologies Conference*. 2011, p. 2387.

[100] S Levy and T HESS. “Tension shell design considerations for planetary entry”. In: *7th Structures and Materials Conference*. 1966, p. 1741.

[101] Gongnan Xie et al. “Thermomechanical optimization of lightweight thermal protection system under aerodynamic heating”. In: *Applied Thermal Engineering* 59.1-2 (2013), pp. 425–434.

[102] Ralf Knoche et al. *Thermo-mechanical Design and Plasma Test Verification on PARES CMC Nose Cap*. Tech. rep. SAE Technical Paper, 2008.

[103] Javad Fatemi. “Metallic thermal protection system for the expert re-entry vehicle: Modelling and analysis”. In: *Thermal Protection Systems and Hot Structures*. Vol. 631. 2006.

[104] ECSS. *ECSS-E-HB-32-26A Spacecraft Mechanical Loads Analysis Handbook*. Feb. 2013.

[105] Christian Messe. *Thermostructural problem of hypersonic airbreathing flight systems: modeling and simulation*. Stuttgart: Institut für Statik und Dynamik der Luft-und …, 2017.

[106] Chenglong Hu et al. “Long-term oxidation behaviors of C/SiC composites with a SiC/UHTC/SiC three-layer coating in a wide temperature range”. In: *Corrosion Science* 147 (2019), pp. 1–8.

[107] Bernhard Heidenreich. “Carbon fibre reinforced SiC materials based on melt infiltration”. In: *6th International Conference on High Temperature Ceramic Matrix Composites HTCMC 6*. 2007.

[108] Yang Wang, Zhaofeng Chen, and ShengJie Yu. “Ablation behavior and mechanism analysis of C/SiC composites”. In: *Journal of materials research and technology* 5.2 (2016), pp. 170–182.

[109] Thomas Reimer. “The EXPERT C/C-SiC nose cap-system design and thermomechanical layout”. In: *AIAA/CIRA 13th International Space Planes and Hypersonics Systems and Technologies Conference*. 2005, p. 3262.

[110] Anatoly Kolesnikov and Lionel Marraffa. “An analysis of stagnation point thermochemical simulation by plasmatron for Mars probe”. In: *33rd Thermophysics Conference*. 1998, p. 3564.

[111] M Balat and R Berjoan. “Oxidation of sintered silicon carbide under microwave-induced CO2 plasma at high temperature: active–passive transition”. In: *Applied surface science* 161.3-4 (2000), pp. 434–442.

[112] Thierry Pichon and Renaud Barreteau. “Thermal Protection Systems: Heritage-Development Status-Perspectives”. In: *18th AIAA/3AF International Space Planes and Hypersonic Systems and Technologies Conference*. 2012, p. 5846.

[113] H Bohrk, H Elsaber, and Hedrik Weihs. “The SHEFEX II thermal protection system”. In: *7th European Symposium on Aerothermodynamics*. Vol. 692. 2011, p. 96.

[114] AE Sheindlin, IS Belevich, and IG Kozhevnikov. *Enthalpy and specific heat of graphite in temperature range 273 to 3650 K*. Tech. rep. Inst. of High Temperatures, Moscow, 1972.

[115] Rajan Tandon et al. *Ultra high temperature ceramics for hypersonic vehicle applications.* Tech. rep. Sandia National Laboratories (SNL), Albuquerque, NM, and Livermore, CA …, 2006.

[116] Zircar. *RS-ZFELT Zirconia Felt*. https://www.zrci.com/material/rs-3000-felt-2-2/. Online; accessed 13 March 2024.

[117] K Keller et al. "Advanced high temperature insulations". In: *Thermal Protection Systems and Hot Structures*. Vol. 631. 2006.

[118] Sachin Kumar and Shripad P Mahulikar. "Selection of materials and design of multilayer lightweight passive thermal protection system". In: *Journal of Thermal Science and Engineering Applications* 8.2 (2016), p. 021003.

[119] Final Advanced Materials. *Contronics® Ceramic Adhesives Technical Sheet*. https://www.final-materials.com/gb/index.php?controller=attachment&id_attachment=12. Online; accessed 13 March 2024.

[120] Ansys Inc. *Ansys Mechanical APDL Theory Reference, Release 2021 R1*.

[121] Ali Gülhan et al. "Aerothermal Qualification of High Temperature Materials and Structures in Ground Facilities". In: *Thermal Protection Systems and Hot Structures*. Vol. 631. 2006.

[122] Stefano Mungiguerra et al. "Qualification and reusability of long and short fibre-reinforced ultra-refractory composites for aerospace thermal protection systems". In: *Corrosion Science* 195 (2022), p. 109955.

[123] Jeroen Buursink. "On the development of a cooled metallic thermal protection system for spacecraft." In: (2005).

[124] Karl Cowart and John Olds. "Integrating aeroheating and TPS into conceptual RLV design". In: *9th International Space Planes and Hypersonic Systems and Technologies Conference*. 1999, p. 4806.

[125] PlotDigitizer. *Plot Digitizer*. https://plotdigitizer.com. Online; accessed 16 February 2024.

[126] NASA. *TPSX Materials Database*. https://tpsx.arc.nasa.gov/MaterialsDatabase. Online; accessed 16 February 2024.

[127] Michele Ferraiuolo and Oronzio Manca. "Heat transfer in a multi-layered thermal protection system under aerodynamic heating". In: *International Journal of Thermal Sciences* 53 (2012), pp. 56–70.

[128] NASA. *NASA SP-8032: BUCKLING OF THIN-WALLED DOUBLY CURVED SHELLS*. Aug. 1969.

[129] Ronald Wagner et al. "On the imperfection sensitivity and design of spherical domes under external pressure". In: *International Journal of Pressure Vessels and Piping* 179 (2020), p. 104015.

[130] Ansys Inc. *Ansys Mechanical Users Guide, Release 2021 R1*.

[131] John Mainsville. *Product Selection Guide*. https://www.jm.com/content/dam/jm/global/en/oem/selector-guides/OEM_Transport_Selector_Guide-WEB.pdf. Online; accessed 13 March 2024.

[132] Nigel Phillips. “Mechanisms for the Beagle2 lander”. In: *9th European Space Mechanisms and Tribology Symposium*. Vol. 480. 2001, pp. 25–32.

[133] K3RX. *K3RX Datasheet*. https://www.k3rx.com/wp-content/uploads/2021/11/dataSheet_K3RX-rev02.pdf. Online; accessed 13 March 2024.

A

Heat Shield Dimensioning

The sphere-cone heat shield geometry for the MDM heat shield is parameterized by half-vertex angle θ_c, base radius R_b, nose radius R_n, and shoulder radius R_s. For planetary entry capsules, relations A.1 are typically used [18].

$$R_n = 0.5R_b \qquad R_s = 0.1R_n \tag{A.1}$$

Figure A.1 and the following equations used to dimension the heat shield are obtained from [92].

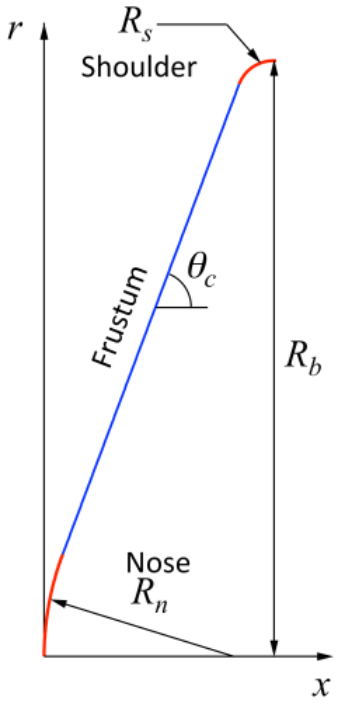

Figure A.1: Generatrice for parameterization of the heat shield geometry [92].

Using the coordinate system (x,r) and the sphere-cone's apex as the origin, the coordinates $(x_{t,n}, r_{t,n})$ of the point at the end of the spherical nose and the start of the conical frustum is given by:

$$x_{t,n} = R_n(1 - \sin\theta_c) \qquad r_{t,n} = R_n \cos\theta_c \tag{A.2}$$

The point $(x_{t,s}, r_{t,s})$ between the end of the frustum and the start of the torical shoulder is:

$$x_{t,s} = R_n(1-\sin\theta_c)+[R_b-R_n\cos\theta_c-R_s(1-\cos\theta_c)]\cot\theta_c \qquad r_{t,s} = R_b-R_s(1-\cos\theta_c) \tag{A.3}$$

The maximum required TPS areal density is obtained by dividing the maximum heat shield mass by the total surface area of the heat shield. These masses are 8 kg and 6.5 kg for the selected 45° and initial 70° heat shields respectively. The total surface area is calculated by adding the surface areas of the nose A_{nose}, frustum A_{cone}, and shoulder $A_{shoulder}$.

$$A_{nose} = 2\pi R_n^2(1 - \sin\theta_c) \tag{A.4}$$

$$A_{cone} = \pi(r_{t,s} + r_{t,n})\sqrt{(x_{t,s} - x_{t,n})^2 + (r_{t,s} - r_{t,n})^2} \tag{A.5}$$

$$A_{shoulder} = 2\pi R_s(R_s \sin\theta_c + (R_b - R_s)\theta_c) \tag{A.6}$$

B

Material Data

This section shows the thermal and mechanical material properties used for the TPS and verification exercises throughout this work.

B.1. DLR C/C-SiC XB

Property	Value	Unit
Density	1900	kg/m^3
Porosity	3.5	%
Fiber volume	65	%
Young's Modulus $\parallel$ (E1, E2)	60	GPa
Young's Modulus $\perp$ (E3)	20	GPa
Shear Modulus $\parallel$ / $\perp$	8 / 9	GPa
μ_{12}	0.03	-
μ_{13}, μ_{23}	0.2	-
Tensile Strength	80	MPa
Compressive Strength	210	MPa
Flexural Strength	160	MPa
Interlaminar Shear Strength	28	MPa
Tensile strain to failure	2.5	%
Flexural strain to failure (295.15 - 1773.15 K)	4.1 - 4.6	%
CTE (295.15 - 1773.15 K) $\parallel$	-1 - 2.5	10^{-6}/K
CTE (295.15 - 1773.15 K) $\perp$	2.5 - 7	10^{-6}/K

Table B.1: Physical and mechanical properties of C/C-SiC XB [105] [107]. $\parallel$ is in the fibrous direction and $\perp$ is in the pile-up direction.

Temperature [K]	Cp [J/kgK]
0	690
373.15	900
673.15	1410
1900	1550

Table B.2: Specific heat capacity of C/C-SiC XB.

Temperature [K]	Thermal Conductivity ∥ [W/mK]	Thermal Conductivity ⊥ [W/mK]
0	15.64	9.16
250	16.74	8.89
500	17.58	8.62
750	18.14	8.36
1000	18.41	8.09
1250	18.42	7.82
1500	18.15	7.55
1750	17.60	7.28
2000	16.78	7.01
2250	15.68	6.75
2500	14.30	6.48

Table B.3: Thermal conductivity of C/C-SiC XB.

B.2. CNR-ISTEC C/C-ZrB_2-SiC CFC

Property	Value	Unit
Density	3500	kg/m^3
Porosity	6	%
Fiber volume	54	%
ZrB_2 volume	36	%
SiC volume	10	%
Young's Modulus ∥ (E1, E2)	135	GPa
Young's Modulus ⊥ (E3)	25	GPa
Shear Modulus ∥,⊥	25	GPa
μ_{12}	0.03	-
μ_{13}, μ_{23}	0.14	-
Tensile Strength (295.15 K)	120	MPa
Tensile Strength (1873.15 - 2073.15 K)	200	MPa
Compressive Strength (295.15 K)	400	MPa
Compressive Strength (1873.15 - 2073.15 K)	500	MPa
Flexural Strength (295.15 K)	180	MPa
Flexural Strength (1873.15 - 2073.15 K)	315	MPa
CTE (295.15 - 2073.15 K) ∥	-1 - 4.2	10^{-6}/K
CTE (295.15 - 2073.15 K) ⊥	4.2 - 8	10^{-6}/K
Thermal Conductivity (295.15 K) ∥	140	W/mK
Thermal Conductivity (1473.15-1773.15 K) ∥	108.6	W/mK
Thermal Conductivity (295.15 K) ⊥	28	W/mK
Thermal Conductivity (1473.15-1773.15 K) ⊥	23.6	W/mK

Table B.4: Thermophysical and structural properties of the UHTCMC material [49][53] [54] [133].

Temperature [K]	Cp [J/kgK]
293.15	564.43
1473.15	1348.68
1773.15	1403.23
1873.15	1418.45
2173.15	1457.95

Table B.5: Specific heat capacity of the UHTCMC material calculated by the rule of mixtures.

B.3. Zircar RS-ZFELT

Property	Value	Unit
Density	240	kg/m^3
Intermittent Use Temperature	2473.15	K

Table B.6: Properties Zircar RS-ZFELT [116].

Temperature [K]	Thermal Conductivity [W/mK]
553.15	0.08
813.15	0.11
1088.15	0.15
1365.15	0.19
1643.15	0.25
1923.15	0.32

Table B.7: Thermal conductivities of Zircar^{TM} Zirconia [116]

Temperature [K]	Specific Heat Capacity [J/kgK]
366.15	544.30
2644.15	753.60

Table B.8: Specific heat capacity of Zircar^{TM} RS-ZFELT [116].

B.4. Q-Fiber

Property	Value	Unit
Density	56	kg/m^3
Intermittent Use Temperature	1533.15	K

Table B.9: Properties Q-Fiber [131].

Temperature [K]	Thermal Conductivity [W/mK]
300	0.032
450	0.04
800	0.065
1000	0.081
1050	0.086
1100	0.09
1200	0.1

Table B.10: Thermal conductivities of Q-fiber [118].

Temperature [K]	Specific Heat Capacity [J/kgK]
300	841
1200	1190

Table B.11: Specific heat capacity of Q-fiber [131].

B.5. RCC TPS Test Case Materials

Material	Density [kg/m^3]	k [W/mK]	Cp [J/gK]
RTV	1410	0.395	1170
SIP	86.5	0.0406	1310
Aluminum (Alloy 2024-T6)	2770	177	875

Table B.12: Materials used in the test case TPS stack by Cowart and Olds [124] taken from the NASA TPSX database [126].